THESIS

IMPACT OF GEOMETRIC DESIGN OF HYDRAULIC CONTACT TANKS ON RESIDENCE TIME DISTRIBUTIONS

Submitted by

Jeremy S. Carlston

Department of Civil and Environmental Engineering

In partial fulfillment of the requirements

For the Degree of Master of Science

Colorado State University

Fort Collins, Colorado

Spring 2015

Master's Committee:

Advisor: S. Karan Venayagamoorthy

Jorge A. Ramirez
Hiroshi Sakurai

ABSTRACT

IMPACT OF GEOMETRIC DESIGN OF HYDRAULIC CONTACT TANKS ON RESIDENCE TIME DISTRIBUTIONS

The research outlined in this thesis investigates how geometric design affects the mixing efficiency of contact tanks used for drinking water disinfection. In particular the configuration of baffles and inlets are assessed in depth using both physical tracer studies and computational fluid dynamics (CFD) simulations. Two rectangular contact tanks were used, both of which are assumed to be representative of disinfection tanks for small municipalities throughout the United States. System performance is analyzed by means of residence time distributions from which the baffling factor (*BF*) and Morrill index (*MI*) performance indicators can be calculated.

First, a parametric study of a 300 gallon tank used for previous research was undertaken. After model validation, 30 CFD simulations were conducted in order to determine optimal baffle configuration by altering channel width, baffle length, and flow orientation. It was found that the baffle lengths should be prescribed such that their openings are roughly equal to the width of the tank's channels. In this manner excessive constrictions or expansions, which lead to undesirable flow separation, can be prevented. It was also confirmed that high length-to-width ratios in the flow lead to a better emulation of ideal plug flow by promoting advective transport of both the water and disinfectant.

Second, a 1,500 gallon, two-baffled tank housed at Colorado State University's hydraulic laboratory in the Engineering Research Center was used to investigate "sharp" inlets, which lead

to poor mixing conditions. Unfortunately operating budgets prohibit many small disinfection facilities from upgrading these preexisting sharp inlets. In an attempt to provide an inexpensive solution, seven attachments to the inlet were tested for potential improvements to contact tank performance. Physical tracer studies were conducted on the prototype in order to obtain RTD curves resulting from each modification. The horizontal T-shaped attachment performed best, attaining a *BF* of 0.59 at a flow rate of 40 gallons per minute (gpm). This is a 74% gain over the unmodified inlet's *BF* of 0.34. From a hydrodynamic analysis of the flow fields obtained from CFD simulations, it was concluded that any inlet configuration leading to a quicker homogenization of longitudinal velocities (especially in the first channel of the tank) and hence better approximation of plug flow will improve system performance.

Finally, seven different inlet modifications to the un-baffled counterpart of the 1,500 gallon tank were investigated. Without any alterations the un-baffled sharp inlet tank provides extremely poor disinfection as evidenced by its baffling factor of 0.05. Due to good agreement between physical and numerical tests for the baffled tank, the un-baffled system was only researched with CFD. Four equally-spaced orifices deflecting flow to the back wall of the tank resulted in the largest gain in performance with an estimated *BF* of 0.27. A hydrodynamic analysis again confirmed that despite lower length-to-width ratios leading to a lower ceiling of mixing performance, better imitation of plug flow results in larger baffling factors and lower Morrill indices.

ACKNOWLEDGEMENTS

First I would like to thank my adviser, Dr. Karan, for all his help and expertise. Dr. Karan continually strives to bring out the best in everyone he knows, including his students. His patience with me and confidence in my abilities kept me motivated to achieve my goal of graduating with my master's degree for which I am very grateful. He is also a major reason why we are planning to publish at least two articles in peer-reviewed journals (one of which is in press), an accomplishment I can always be proud of.

Next I wish to express gratitude to my parents. Your never-ending love and care as I grew up has given me the tools and mindset that I need to be successful at whatever I do. Thank you for always being there for me and always being willing to lend a hand.

Amanda Poincelot deserves special recognition. As my long-term girlfriend she has supported me in all my endeavors, academic and otherwise, throughout my undergraduate and graduate studies. Thank you for being a constant source of encouragement and assistance over these past years.

Justin Kattnig played a major role in getting my research started for which I am grateful. He built the baffles in the prototype at CSU's hydraulic lab, showed me how to work with the equipment, and gave me guidance to achieve successful CFD simulations. Lei Fang also deserves recognition for conducting a large number of physical tracer studies presented in Chapter 4. His desire to be as helpful as possible greatly aided the physical validation process. The other students in the Environmental Fluid Mechanics Research Group at CSU – Farid Karimpour, Jordan Wilson, Ben Mater, Oladapo Aseperi, Jian Zhou, Amrapalli Garanaik,

Ajithshanthar Nithianantham, and Kyung-Seop Sin - were all obliging when I had questions or needed help.

Finally I would like to acknowledge and thank Drs. Ramirez and Sakurai for taking time out of their busy schedules to be on my thesis committee. Your insight, suggestions, and comments are truly appreciated.

TABLE OF CONTENTS

CHAPTER 1: INTRODUCTION

1.1 Background

Water plays a fundamental role to life no matter where it is found. It is no surprise then that water covers over 71% of the Earth's surface and is also found in large quantities throughout the ground and air (USGS, 2014). Despite its essentiality to humans and to life in general, adequate treatment of water to avoid illness and death from its consumption was largely unaddressed for the majority of recorded history. Even the simple action of draining water through sand, which greatly aids in the filtration process, was first documented in the 19th century (Huismans and Wood, 1974). Recognition of the legitimacy of such disinfection techniques stems from work by John Snow, an English physician and founder of epidemiology, who conclusively demonstrated a causal link between those who suffered from a cholera outbreak and the well from which their water was pumped (Johnson, 2006). Before then, actions so obviously detrimental to human and environmental health such as dumping raw sewage into rivers were commonplace.

Since then, rapid advances in public safety and wellness through increased understanding of disinfection and microbial deactivation in drinking water have taken place. Research occurring today attempts to continue this trend by optimizing systems and methodologies to disinfect drinking water at minimal cost to taxpayers while still being adequately safe. This thesis focuses on such research in the hopes that the results are widely useful and implementable by assessing the flow dynamics occurring in disinfection tanks.

1.2 Project Context

In the United States, drinking water is regulated by the United States Environmental Protection Agency (USEPA). Formed late in 1970 after President Nixon signed an executive

order, the EPA protects human health and the environment by overseeing many aspects of human interaction with the environment, including the land, water, air, flora and fauna, and more. The Safe Drinking Water Act (SDWA) followed 4 years later and is the primary regulatory action concerning drinking water for which the EPA is responsible for overseeing. Every one of the more than 150,000 public water systems established at any level (state, local, etc.) in the USA is required to abide by its standards and criteria. After its inception, further guidelines have been established under the SDWA to disinfect drinking water sufficiently depending on the source of water (ground or surface) and to maintain acceptably low levels of disinfection byproducts.

One important stage of drinking water treatment is the inactivation of potentially harmful microorganisms found within the source water. The *CT value* is often used to quantify the level of disinfection attained at this step of treatment. It is based on the assumption that level of microbial inactivation is related to the product of the concentration of the disinfection agent multiplied by a characteristic contact time between the disinfection agent and the water. A given *CT* value must be met or exceeded based on a desired level of microbial inactivation. From a mathematical point of view, one may simply increase the concentration of the disinfection agent until a prescribed level of inactivation is achieved. However, this quickly becomes problematic for a number of reasons. Most importantly, undesirable disinfection byproducts will quickly reach unacceptable levels, which have been shown to cause significant health issues (such as an increased risk of cancer when chlorine is used). The water can also become unpalatable and furthermore, such a method is also highly cost inefficient. Therefore, the engineering problem at hand is to maximize the contact time between the water and the disinfection agent, preferably through simple and easy-to-implement methods. Many effective methods are well-established,

such as installing baffles within the tank to encourage more effective mixing mechanisms. Many small public water systems nonetheless still have issues with their treatment methods due to lack of expertise and resources.

Unfortunately, the contact time between the water to be treated and the disinfection agent as seen in the *CT* value is not constant; due to the complex nature of fluid dynamics, an arbitrary parcel of water will have a different contact time within a tank than another one. It follows from this that an appropriate measure of system performance is needed. Many metrics have been put forth attempting to satisfy this need, but most of them are difficult to measure, ambiguous, or unreliable. Ultimately, the EPA has elected to use a parameter known as the *baffling factor* (*BF*) to evaluate the efficacy of a contact tank. This is not to imply that the *BF* is not without criticism. For example, Table 1.1 implies significant inaccuracy that is all-too-often involved when determining the baffling factor of a system without appropriate physical testing or numerical simulation; basic geometry of the contact tank is described and an approximate *BF* value is attributed to it. Meanwhile, complex flow dynamics that occur in disinfection tanks, operating flow rates, and subtle yet important aspects of the geometry are ignored. The baffling factor has also been shown to sometimes be unjustifiably non-conservative due to issues discussed in Chapter 2. Even so, it is a ubiquitous method to determine if satisfactory disinfection is obtained and is used in the calculation of *CT*, making it a highly important parameter to consider as a researcher and/or manager of a drinking water disinfection system.

Table 1.1: Baffling Classification Table from the Benchmark Technical Guidance Manual (USEPA, 2003)

Qualitative Efficiency	*BF*	Geometric/Baffling Description
Very Poor	0.1	No baffles, agitated basin, very low length to width ratio, high inlet and outlet flow velocities
Poor	0.3	Single or multiple un-baffled inlets and outlets, no intra-basin baffles
Average	0.5	Baffled inlet or outlet with some intra-basin baffles
Superior	0.7	Perforated inlet baffle, serpentine or perforated intra-basin baffles, outlet weir perforated lauders
Perfect ("Plug Flow")	1.0	Very high length-to-width ratio (pipeline flow), perforated inlet, outlet, and intra-basin baffles

1.3 Scope of Work and Thesis Organization

Chapter 2 is intended to lay out in more detail the background and motivation, methodology, and any other esoteric knowledge concerning the research presented in this thesis. More specifically, drinking water standards and regulations, contact tank design, physical tracer studies, numerical simulations, and system performance evaluation are explained to provide more context to the reader. The majority of the contents of Chapters 3 and 4 has been authored as journal manuscripts and hence are self-contained. As such it should be noted that some redundancy exists, especially with regard to general methodology.

Chapter 3 presents a parametric study undertaken to determine optimal geometry in baffled contact tanks. The hypothesis that the length of baffle openings should be designed to be on the order of the width of flow channels was then tested. This was found to be valid independent of several other geometric parameters. Commonly-accepted criteria for optimal system performance such as high length-to-width flow ratios leading to plug-like flow were also confirmed throughout this process.

Chapter 4 details research efforts that focused on modifying subpar sharp inlet configurations of contact tanks. In many small municipalities where such configurations exist it would be prohibitively expensive to upgrade pre-existing tanks, so economical and easily implementable attachments to the inlet were tested and were largely found to produce significant gains in contact times. The hydrodynamics leading to this improved efficiency are explained by means of validated computational fluid dynamics (CFD) models.

Chapter 5 follows a similar approach to Chapter 4 by modifying sharp inlets to improve residence time distributions. However, the tank that is investigated is un-baffled and so a somewhat different methodology must be utilized.

Chapter 6 concludes this thesis by summarizing the research presented in Chapters 3 through 5. Key findings are highlighted and future work intended to achieve better understanding of hydraulic contact tanks is suggested.

1.4 New Contributions

Research presented in this thesis makes the following unique contributions:

- Established the prudence of designing baffled contact tanks such that baffle openings are roughly equal to the width of the flow channels in order to optimize mixing efficiency.
- Demonstrated the use of simple yet effective modifications to sharp inlets of contact tanks to enhance residence time distributions by promoting plug-like flow as quickly as possible, whether the tank is baffled or un-baffled.

1.5 Research Publications

Work found in Chapter 3 is currently under review for publication in the Journal of Hydraulic Research with the title “Internal Hydraulics of Baffled Disinfection Contact Tanks.” The content from Chapter 4 has been accepted for publication in the Journal American Water Works Association under the title “Impact of Modified Inlets on Residence Times in Baffled Tanks” and is expected to appear in the June 2015 issue. The same research been accepted for presentation in the Emerging and Innovative Technologies Track at the 2015 World Environmental and Water Resources (EWRI) Congress of the Environmental and Water Resources Institute of the American Society of Civil Engineers (ASCE).

CHAPTER 2: LITERATURE REVIEW

2.1 Small Drinking Water Distribution Systems and Associated Issues

Municipalities of low population density areas in the United States are all too often plagued by financial constraints, and their public drinking water systems are no exception. Although less than 20% of the USA's populace is served by such systems (deemed to be "small" by the USEPA if 3,300 people or less use them), they are responsible for over 95% of incidences where maximum contaminant levels within the drinking water are exceeded under federal regulations (USEPA, 2011 and 2012). This is a direct result of a lack of both know-how and resources that arises from insufficient funding. As such, in recent years considerable effort has been devoted to researching improvements on the design of chlorination contact tanks through methods that are both effective and easily implementable for these public water drinking systems. Although small systems are at the largest risk of violations (and as such are of primary concern), it is hoped that the research presented in this thesis can guide managers of disinfection systems of any size.

2.2 Disinfection of Drinking Water Using Chlorine

Although the flow dynamics and hydraulic mixing efficiency within disinfection contact tanks are ultimately the focus of the researched outlined here, it is important to be aware of the context in order to gain a more thorough understanding of the importance and applicability of the results. With this in mind, the framework for assessing drinking water by chlorination in the United States is briefly outlined.

Chlorine is the most widely-used disinfection agent for deactivation of microbes in drinking water, especially for small public water systems, due to its cost efficiency,

dependability, and availability; furthermore, well-established standards and guidelines have been set forth by the USEPA. Therefore, chlorine is the sole disinfection agent considered in this thesis.

Disinfection by chlorination is assessed by the USEPA using a quantity known as the *CT value*. It can be calculated by multiplying the chlorine's concentration by a characteristic contact time. Due to the disassociation of chlorine in water into hypochlorous acid and hypochlorite, the former of which is more effective at microbial inactivation, *CT* values are found to be sensitive to both pH levels and temperature (Letterman, 1999). Davis and Cornwell (2008) provide an empirical approximation to the *CT* as follows:

$$CT = 0.9847 C^{0.1758} pH^{2.7519} T_o^{-0.1467}, \tag{1}$$

where C is the chlorine's concentration and T_o is the water's temperature. Equation 1 can be a desirable way to estimate a *CT* value because characteristic contact times are not always known and can be ambiguous. However, the calculation of *CT* in Equation 1 does not involve any actual contact time and hence does not take all physically-relevant variables into account. A physical tracer study or a sufficiently accurate numerical simulation (described in Section 2.3.1) is therefore desirable for more accurate calculations of *CT*.

In practice, a particular *log inactivation* is usually desired. It is defined as

$$LI = log_{10}\left(\frac{\phi_{in}}{\phi_{out}}\right), \tag{2}$$

where LI is the log inactivation, ϕ_{in} is the influent contaminant concentration and ϕ_{out} is the effluent contamination concentration. A 1-log inactivation is one where 90% of contaminants are treated, a 2-log inactivation is one where 99% are treated, and so on. Achieving an n-log

inactivation requires a particular *CT* value as prescribed by the USEPA. Therefore, it is clearly desirable to maximize *CT* in order to safely disinfect drinking water. One way to do this would be to increase chlorine concentrations; however, this is a poor solution as it makes water unpalatable, can result in excessive disinfection byproducts, and is highly inefficient from an economic standpoint. Alternatively, hydraulic tanks used to mix source water and a disinfecting agent can be carefully assessed and designed by engineers in order to increase contact times without creating unpleasant and/or unsafe drinking water and without incurring extra expenses to taxpayers. Chapters 3 through 5 highlight research efforts attempting to investigate issues with hydraulic contact tank design that are often overlooked in traditional design methodology and evaluation.

2.3 Assessing Contact Tank Performance

2.3.1 Physical Tracer Studies

In order to investigate the adequacy of a contact tank design, a *physical tracer study* is often conducted on the tank. Two prevalent approaches to accomplish this are the *step input method* and the *pulse input method*. In the case of the former a *tracer* (a substance of measurable concentration) is continuously injected at a steady rate at the inlet of the system along with the source water. It is vital to ensure that the tracer is well mixed before entering the system through the inlet. The concentration of the tracer, assumed to be representative of an arbitrary disinfectant, is then monitored as a function of time at the outlet until it does not change significantly. This typically occurs when at least 99% of the concentration at the inlet is observed at the outlet. The result is the system's *residence time distribution (RTD) curve*, which increases with time monotonically and is explained in greater detail in Section 2.3.2. Exceptions to the

monotonic behavior can be present when measurement error occurs in a physical test but are generally ignored if they are small.

Alternatively, the pulse input method may be utilized. Instead of continual, steady injection of the tracer at the inlet, a large and sudden quantity is injected as quickly as possible at the beginning of the test. Of course, an instantaneous injection is unrealistic, so efforts should be made to achieve introduction of the tracer into the system within about 1% of the system's theoretical distribution time (*TDT*, described in Section 2.3.2). The concentration of the tracer is recorded at the outlet until it recedes sufficiently close to zero. This results in the flow-through curve (FTC) of the system, which is also explained in Section 2.3.2.

With the advent of computational fluid dynamics (CFD) (see Section 2.5) a numerical simulation can be run in lieu of physical tracing, provided the model is sufficiently accurate. A *passive scalar* (i.e. a scalar quantity that is affected by the dynamics of the flow field but does not affect the flow field in return) replaces the tracer and plays the same role the tracer does in the physical study. After adequately approximating the flow field the scalar is introduced to the tank at the inlet via boundary condition specifications. Similar to the physical study, the model then records the scalar's concentration at the outlet and interpolates as necessary to obtain either the flow-through curve or residence time distribution for contact tank at hand.

2.3.2 Flow-Through and Residence Time Distribution Curves

The result of a step-input physical tracer study is the residence time distribution curve. Figure 2.1 depicts results for a typical step-input tracer study as opposed to the case of perfect plug flow. Plug flow is the ideal scenario and refers to very high length-to-width ratios of flow, which leads to advection-dominated transport of both the water and tracer with negligible

diffusion. This is desirable because advection is a much faster and more efficient mixing mechanism compared to diffusion, even when higher effective viscosities are presumed to occur (as is the case in many turbulence models). Pure advection produces a square-like RTD curve where the normalized concentration at the outlet jumps instantaneously from 0% to 100% at the system's TDT. Any deviation from the ideal curve can be attributed to diffusive action occurring in the contact tank. In earlier portions of the RTD curve this implies the possibility of inadequate microbial inactivation, while in later parts of the curve this leads to the potential for recirculation of flow. Such recirculation can in turn lead to undesirable disinfection byproducts.

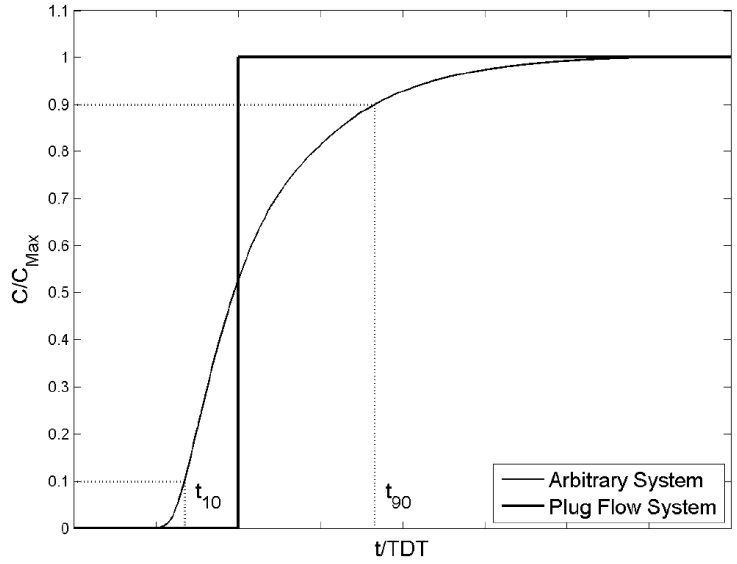

Figure 2.1: RTD Curves for an Arbitrary versus an Idealized System

If the pulse-input method is employed instead, the flow-through curve (FTC) rather than the RTD curve is obtained by monitoring the tracer's concentration at the outlet as seen in Figure 2.2. A typical system's FTC is shown in contrast to a plug flow, which is seen as an instantaneous spike of tracer concentration at $t = TDT$. Typically the RTD curve is desired over the FTC because important variables and relationships can be obtained directly from it.

Analogous to the connection between cumulative distribution and probably density functions, the RTD curve may be obtained from the FTC by the following relationship between the two:

$$RTD(t) = \frac{1}{T_r}\int_0^t FTC(\tau)d\tau, \tag{3}$$

(where T_r is the release time for the pulse input) which can be approximated by numerical integration.

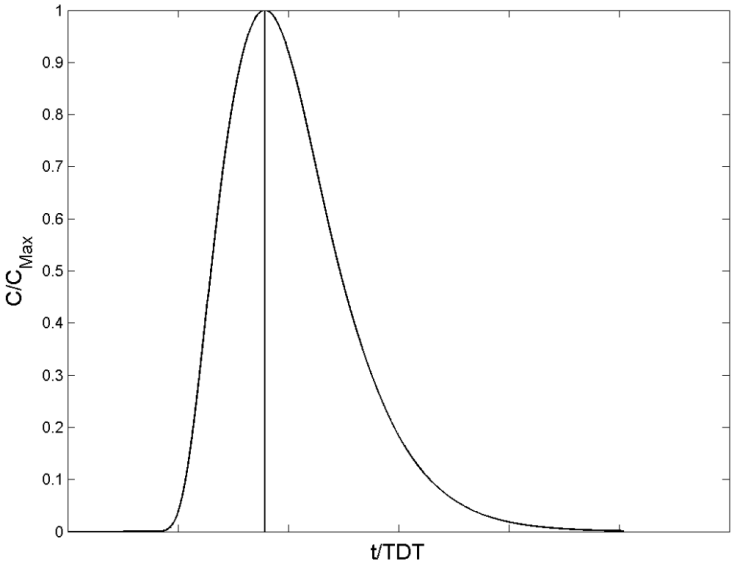

Figure 2.2: Generic FTC from a Physical Tracer Study Using the Pulse Input Method Compared to a FTC Resulting from Plug Flow

Table 2.1 briefly summarizes the main advantages and disadvantages of the two input methods for physical tracer studies. Essentially, the step input method is more costly yet provides better results, while the opposite is true for pulse input. Because the necessary chemical feed equipment had already been installed, tested, and used at Colorado State University's Hydraulic Lab, the step input method was chosen for the physical tracer studies presented in Chapter 4. Furthermore, sodium chloride was used as the conservative tracer, which is inexpensive and readily available. Chapter 3 utilizes FTC data obtained by Shiono et al (1991) to validate computational modeling.

Table 2.1: Comparison of Step and Pulse Input Methods

Step Input	Pulse Input
RTD curve is found directly	FTC must be integrated to find RTD curve
Larger quantities of a tracer are needed	Smaller quantities of a tracer are needed
Data is more reliable	Data is harder to obtain consistently and accurately
More equipment required	Less equipment required

2.3.3 Parameters of System Performance

With the concept of the FTC and RTD curves described, it is now prudent to introduce some helpful parameters used to describe a disinfection contact tank. First, the theoretical detention time (*TDT*) is defined as

$$TDT = \frac{V}{Q}, \tag{4}$$

where V is the volume of water-tracer mixture in the tank and Q is the steady volumetric flow rate through the system. A system's *TDT* can be thought of as an average residence time spent in the tank by fluid particles. In the ideal case of pure advection the concentration of the disinfectant at the outlet would instantaneously rise from 0 to 100% of its maximum value at the system's *TDT*. Since this is the best case scenario, it is intuitive to normalize concentrations by the *TDT* for easy comparison of system performance across various volumes, flow rates and geometries. Concentrations are similarly normalized by the concentration of the tracer at the inlet, which is the maximum possible value of tracer concentration in the tank.

Many parameters have been proposed for quantifying system performance, e.g. the baffling factor, Morrill index, dispersion number, and dispersion index (Wilson & Venayagamoorthy, 2010; Wols et al, 2010). In the United States and many other places, the

baffling factor (*BF*) is a parameter of prime importance, largely due to the role that it plays in the EPA's formulation of safe drinking water standards (USEPA 2003). It is calculated as

$$BF = \frac{t_{10}}{TDT}, \tag{5}$$

where t_{10} is the time at which 10% of the concentration of the physical tracer at the inlet is observed at the outlet as depicted in Figure 2.1. It is used in the calculation of *CT* values and hence is a primary method of quantifying contact tank performance when using chlorine as a drinking water disinfectant.

Despite its prevalence, shortcomings of the *BF* as a quantifier of system performance have been noted. Specifically the *BF* is a *short-circuiting* indicator, meaning it only assesses how much of the tank's volume is bypassed as the majority of flow travels from the inlet to the outlet. While useful in determining whether or not sufficient contact times have been achieved, it does not take into account recirculation as revealed by the later portions of the RTD curve. The baffling factor therefore fails to provide information about the level of disinfection byproduct formation potentially occurring in the contact tank. To this end the Morrill index (*MI*) is also sometimes used, especially outside the United States. It is defined by the following (Morrill et al, 1932):

$$MI = \frac{t_{90}}{t_{10}}, \tag{6}$$

where *MI* is the Morrill index, t_{90} is the time at which 90% of the tracer's original concentration is observed at the outlet, and t_{10} is as defined previously. It can be thought of a measure of dispersion occurring in the contact tank (Teixeira & Siqueira, 2008). As with the baffling factor the best case is *MI* = 1 corresponding to plug flow but can reach much larger values depending

on the amount of dispersion actually occurring. As the values of both t_{10} and t_{90} are consequences of actual flow dynamics (as opposed to the *TDT*, which only considers flow rate and volume), the Morrill index arguably provides a more insightful parameter by which a contact tank's performance can be quantified. However, due to its adaption by the EPA in their standards and its subsequence prevalence throughout the United States, the *BF* is the primary parameter used to determine hydraulic disinfection efficiency in this thesis. Fortunately (as will be shown in Chapters 3 through 5) a superior *BF* usually implies a superior *MI*, and likewise subpar *BF*s usually indicate that the system's *MI* is also poor.

2.4 Contact Tank Design

In general, behavior of fluid flow is highly sensitive to boundary conditions as imposed by geometry (Munson et al, 2013), and contact tanks are no exception. With this in mind the geometric design of such systems must be considered carefully. Important aspects of geometric design include baffles and inlets as discussed in Sections 2.4.1 and 2.4.2, respectively.

2.4.1 Baffled versus Un-baffled Tanks

Baffles have been used for decades to economically improve residence times in hydraulic contact tanks. They are physical wall-like barriers that divert flow away from the path it would otherwise take. This is a relatively easy yet effective method of increasing the contact time between the source water and the disinfectant, leading to increased mixing efficiency. The baffles create a more channeled environment for the water by increasing length-to-width ratios of flow in order to encourage transport through advection, which is superior to diffusion for mixing purposes (Kattnig, 2014; Amini et al, 2011; Li et al, 2006; Peplinski & Ducoste, 2001). It also limits the creation of dead zones of stagnated water by guiding the flow through portions of the tank that would otherwise be short-circuited (Kattnig, 2014; Zhang et al, 2013; Amini et al,

2011; Wols et al, 2010; Kim et al, 2010; Wols et al, 2008; Evans et al, 2003). In small communities where financial budgets for drinking water disinfection are limited, baffled systems provide a cost-effective solution for ensuring adequate contact time.

In un-baffled tanks, flow intuitively tends to take shorter paths to the outlet. Short-circuiting occurs and large dead zones are created in the tank. In these dead zones drinking water is often inadequately disinfected, while other portions of the tank may experience recirculation. This recirculation has the potential to create disinfection byproducts which can include carcinogens. Typical *BF*s for un-baffled tanks are about 0.1 on account of their low length-to-width ratios of flow and high velocities found at both the inlet and outlet (USEPA, 2003). Figure 2.3 schematically depicts a plan view of different major flow paths taken for an arbitrary contact tank with and without baffles.

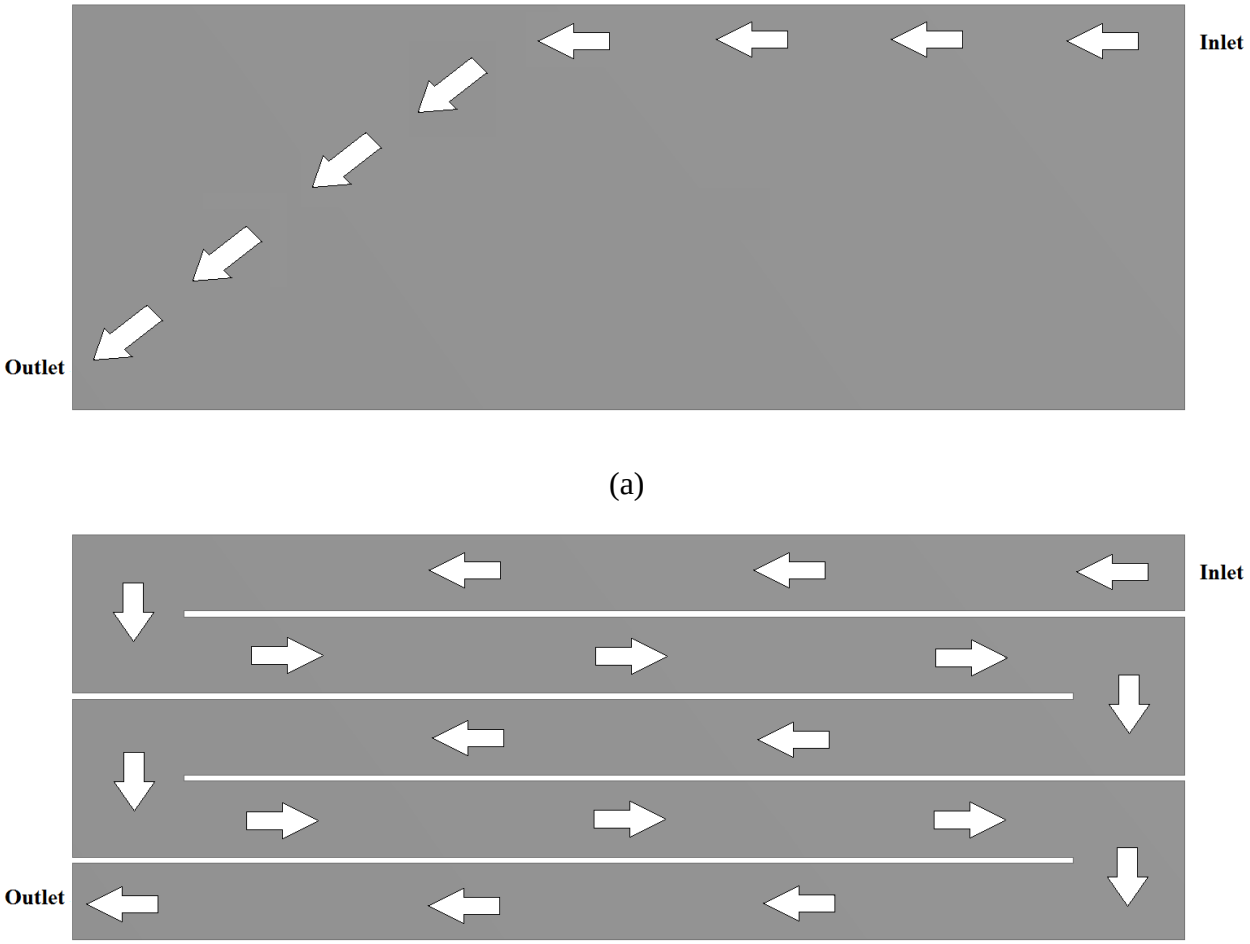

Figure 2.3: Likely Dominant Flow Paths in (a) Un-baffled and (b) Baffled Tanks

Although baffles are clearly useful, parametric studies have shown that increasing the number of baffles in a typical contact tank beyond about 6 results in diminishing returns in hydraulic disinfection efficiency (Xu & Venayagamoorthy, 2010). Furthermore it can also be difficult or cost-prohibitive to modify geometry in pre-existing tanks. In light of this, it is appropriate to consider other means for enhancing residence times even further in baffled contact tanks, particularly when chlorine is used for microbial inactivation. It is also worthwhile to

examine certain aspects of baffled contact tank design that is often overlooked in traditional design methodology.

2.4.2 Ideal versus Sharp Inlets

In baffled contact tanks, inlets with cross-sectional geometry identical to those of the compartments in the tank are ideal as they more closely resemble plug flow and hence minimize diffusive action (see, e.g., Green et al 2006 for dependence of system performance on inlet size). In practice this is often not possible due to the existing facilities and equipment that connects the disinfection tank to the source water. As a result, sharp inlets are frequently used. In this scenario the pipe delivering drinking water to the disinfection system, which has a relatively small diameter, shoots a jet of water into the contact tank. Compared to the rather quiescent water already in the tank, this jet moves at a high speed. Free-shear turbulence is generated due to the large differences in mean velocities between the jet and its slow-moving surroundings (Pope, 2000). Mixing in the immediate vicinity of the inlet is enhanced on account of this high level of turbulence. However, the use of sharp inlets tends to increase the likelihood of mediocre system performance as a whole by causing short-circuiting and associated dead zones in the tank.

In the case of un-baffled tanks an ideal inlet is still one that is as large as possible while being oriented to create the largest length-to-width flow ratios, although resulting residence time distributions will still be inferior to the baffled alternative. An un-baffled tank typically implies a lack of expertise and/or funding, meaning such an inlet condition is highly improbable in practice; a more likely scenario in an un-baffled system is a sharp inlet. Based on this discussion, the combination of a sharp inlet and un-baffled geometry implies an extremely poor design. It would therefore be desirable to investigate cost-effective and easily implementable modifications

to a sharp inlet in order to enhance contact times and mitigate both short-circuiting and recirculation.

2.5 Computational Fluid Dynamics

Fluid mechanics has historically been studied through a combination of theoretical and empirical reasoning. Fundamental equations of physics combined with scaling arguments, dimensional analysis, simplifying assumptions, and other techniques allowed scientists to gain insight into the behavior of fluids. While useful, these methods ultimately provide an incomplete picture of the flow dynamics. When applied to fluids the general equations of motion typically lack analytical solutions and physical tests can only provide a limited amount of data.

In more recent times, advancements in technology and computer science have allowed a new subfield of fluid mechanics to flourish. In *computational fluid dynamics* (CFD), the complex partial differential equations that govern flow are transformed into systems of algebraic equations by a method known as *discretization*. These systems of equations are then solved by powerful computer processors in order to provide approximate solutions at pre-defined, discrete points in a given flow field called a *mesh* or *grid*. A good CFD modeler will always carefully scrutinize these results as there are a plethora of possible sources of error (discussed in Section 2.5.6), so results can often appear physically realistic when they are not. Nevertheless CFD is an invaluable tool that can be used to obtain unprecedented insight into fluid behavior if one is aware of its shortcomings.

2.5.1 Numerical Methods

Many equations that describe physical processes are partial differential equations (PDEs). PDEs are a notoriously difficult class of equations to solve due to dependence on multiple

independent variables, the potential to contain nonlinearity, and the need to prescribe accurate boundary and initial conditions. As a result very few PDEs have known analytical solutions. In order to study the physical processes described by PDEs, scientists and engineers must often turn to numerical methods to obtain approximate solutions at a finite number of points in a function's domain. This is achieved through discretization wherein algebraic estimates are substituted for unknown derivatives in a given PDE and the resulting system of algebraic equations is evaluated (Moin, 2010). Several variations to this basic approach exist, but the *finite volume method* (FVM) is most often used for CFD simulations because it can be shown that conservative quantities are indeed conserved using the FVM.

In the FVM, an arbitrary flow domain is divided into many smaller volumes known as *cells* which make up the overall mesh. Each cell contains an approximate solution for each equation solved in the computational grid at that point in time. To obtain these estimates the FVM uses information from adjacent and other nearby cells in accordance with the discretization schemes utilized. Boundary conditions are used instead if a cell is at the edge of the flow domain and initial conditions are used to compute solutions for the first time step.

2.5.2 Governing Equations of Flow

As is usually the case in classical mechanics, it is prudent to begin with the basic conservation laws, namely conservation of mass, momentum, and energy. By applying conservation of mass to an infinitesimal parcel of fluid with constant density the incompressible continuity equation in differential form is obtained:

$$\nabla \cdot \vec{U} = 0, \tag{7}$$

where $\vec{U}$ = $\vec{U}(\vec{x},t)$ is the time and space-dependent velocity vector of the fluid. A similar approach is used to obtain the incompressible Navier-Stokes equations by applying conservation of momentum to a Newtonian fluid of constant density:

$$\rho\left(\frac{\partial\vec{U}}{\partial t}+\vec{U}\nabla\cdot\vec{U}\right)=-\nabla p+\mu\nabla^2\vec{U}+\rho\vec{f}, \tag{8}$$

where ρ and μ are the density and viscosity of the fluid, respectively, $p = p(\vec{x},t)$ is the pressure, $\vec{f} = \vec{f}(\vec{x},t)$ is the body force, and $\vec{U}$ is as defined previously. After discretization is performed, Equations 7 and 8 can be (approximately) solved simultaneously to obtain the unknown pressure and velocity vector components in each spatial dimension at each point in the mesh and each discrete time step. From a mathematical perspective, Equation 8 is difficult to solve (whether it be analytically or numerically) due to its nonlinearity and because it exhibits behavior of all three major types of partial differential equations, namely parabolic, hyperbolic, and elliptic. Each of these types creates their own unique challenges; for example, the elliptic pressure gradient term is computationally costly if strongly non-hydrostatic conditions exist. If carefully approached, however, an acceptable numerical solution is obtainable for many classes of flow.

2.5.3 Turbulence Modeling

Turbulence occurs in a fluid when momentum overwhelms dissipative viscous action and creates instability. It is often characterized as being "unsteady, irregular, and seemingly random and chaotic" (Pope, 2000). Although turbulence is favorable over orderly, laminar flow for many engineering purposes such as mixing or aerodynamic drag reduction, a major problem presents itself from a numerical modeling standpoint: an extremely wide range of length and time scales are found in turbulent flow. In fact, a difference of 5 orders of magnitude (or even more) between the largest and smallest length scales is not uncommon. In a more quantitative sense,

consider the *Re*-dependent range of length scales in turbulence based on scaling arguments and physical intuition as asserted by Kolmogorov (Pope, 2000):

$$\frac{l_0}{\eta} \sim Re^{3/4}, \tag{9}$$

where l_0 is a length scale on the order of the largest scale of flow and η is the Kolmogorov scale, the hypothesized smallest length scale. Since Relationship 9 is only for one spatial dimension, the separation of scales for a three-dimensional flow increases as $(Re^{3/4})^3 = Re^{9/4}$ if Kolmogorov is correct. As a result the computational expense required to simulate every length scale increases by $Re^{9/4}$ as well. With Reynolds numbers commonly 10^4 and higher in engineering flows (especially when dealing with low-viscosity fluids such as water or air), it quickly becomes infeasible or even impossible to capture every facet of turbulence with contemporary computing power. In order to satisfy the need to predict fluid flow for engineering purposes in the face of these impracticable computing requirements, a wide variety of turbulence models have been created. These models greatly diminish computational effort by filtering out one aspect or another of turbulence and directly resolving only the most desired portions of the flow. Sections 2.5.3.1 to 2.5.3.6 detail some common methodologies for handling the challenging topic of turbulence simulation.

2.5.3.1 DNS

Direct numerical simulation (DNS) is the approach wherein no turbulence models are used and every scale of turbulence is resolved on the computational grid via numerical solutions of Equations 7 and 8. On account of the aforementioned strong Reynolds-number dependence of computing power needed, DNS is relatively rare for engineering purposes. Even when DNS is undertaken, low velocities and small geometries are typical. It is most useful for insight on a

fundamental level and to guide development of new turbulence models. As such no DNS was undertaken in the research presented in this thesis.

2.5.3.2 LES

Large eddy simulation (LES) places a spatial filter on the flow in order to separate larger length scales from smaller ones. The larger scales of motion are then directly resolved on the computational mesh in a similar fashion to DNS while a sub-grid is utilized for smaller scales. Some sort of turbulence model is selected on the sub-grid to approximate flow at these finer scales. In this formulation of turbulence modeling a significant reduction in computing effort is observed between DNS and LES. However, it is still too costly for widespread use, mainly because even the largest scales in boundary layers near walls typically require extremely small time steps and grid spacing (ANSYS, 2011). As a result LES was also not used for the research highlighted in Chapters 3 through 5.

2.5.3.3 RANS

RANS modeling refers any turbulence modeling in which the mean continuity and Reynolds-averaged Navier-Stokes equations are solved. To obtain these equations, a statistical approach to turbulence is considered. In this framework one may intuitively dissect the unknown flow variables (i.e. velocity components and pressure) into an average and fluctuating component through a process known as Reynolds decomposition:

$$\vec{U} = \bar{U} + u', \tag{10}$$

$$p = \bar{p} + p', \tag{11}$$

where over-bars denote an average value of a variable and primes denote fluctuating values of a variable. By definition the average of all fluctuations is zero so that any instantaneous deviation from a variable's average is equal the fluctuation at the point in time and space. Substitution of Equations 10 and 11 into the incompressible continuity and Navier-Stokes equations (7 and 8) along with some mathematical manipulation yields the foundation for a large assortment of turbulence models:

$$\nabla \cdot \bar{U} = 0, \tag{12}$$

$$\rho\left(\frac{\partial \bar{U}_i}{\partial t} + \bar{U}_j \frac{\partial \bar{U}_i}{\partial x_j}\right) = \frac{\partial \bar{p}}{\partial x_i} + \rho \frac{\partial}{\partial x_j}\left(\nu \frac{\partial \bar{U}_i}{\partial x_j} - \overline{u_i' u_j'}\right). \tag{13}$$

(Note: Equation 13 is written in tensor notation to succinctly denote the second order tensor $\overline{u_i' u_j'}$.*)* The mean continuity equation (12) looks and behaves quite similarly to its instantaneous counterpart (7). Unfortunately an extra term, $\overline{u_i' u_j'}$, appears on the right-hand side of Equation 13. These six extra unknown values are collectively known as the *Reynolds stresses*. They are the covariance of the fluctuating velocity field and can be physically interpreted as stresses between the mean and fluctuating velocity field caused by momentum transfer at the molecular level. The original equations of motion for incompressible fluid particles, 7 and 8, are in theory solvable due to the number of unknown variables being equal to the number of independent equations. Because of the appearance of the Reynolds stresses in Equation 13, the new disparity between independent equations and unknowns is referred to as the *turbulence closure problem*.

Within a RANS framework the intent behind turbulence modeling is to predict Reynolds stresses sufficiently accurately for the problem at hand. Although each model has its own strengths and weakness, none have been able to adequately calculate Reynolds stresses

independently of flow regime. As such a large number of closure schemes to the RANS equations have been created and the turbulence modeler must practice sound engineering judgment to determine the most appropriate one. Regardless of model chosen, the result of a RANS simulation is a temporally-filtered average flow field.

2.5.3.4 The Turbulent Viscosity Hypothesis

A common starting point in tackling the closure problem within the RANS framework involves the use of the *turbulent-viscosity hypothesis*. In laminar flow of a Newtonian fluid, shear stress is assumed to be proportional to the rate of shearing strain by the fluid's viscosity; the turbulent-viscosity hypothesis creates an analogous relationship for turbulent flows by assuming that the deviatoric (anisotropic) portion of the Reynolds stresses are proportional to the average rate of strain by a so-called turbulent viscosity. This can be written as

$$\overline{u_i' u_j'} = \frac{2}{3} k \delta_{ij} - \nu_t \left(\frac{\partial \bar{U}_i}{\partial x_i} + \frac{\partial \bar{U}_j}{\partial x_j} \right), \tag{14}$$

where ν_t is the turbulent viscosity and $\frac{2}{3} k \delta_{ij}$ is the isotropic portion of the Reynolds stresses (subtracted out from the total Reynolds stresses to obtain the anisotropic portions) (Pope, 2000). In Equation 14 it can be seen that ν_t is not a property of the fluid but rather an assumed property of the flow, implying that in some sense "viscosity" is a misnomer. It is therefore not predictable a priori, but utilizing the turbulent-viscosity hypothesis makes RANS modeling much more tractable by reducing the number of unknowns from 6 to 1.

2.5.3.5 RNG k-ε Model

Perhaps the most popular RANS models are the so-called *k-ε models*. The standard *k-ε* model was developed by Jones and Launder in 1972 and has since been modified several times

to form its own subclass of models. Differential transport equations for both k (turbulent kinetic energy) and ε (turbulent kinetic energy dissipation rate) are solved from which ν_t can be prescribed for use in the turbulent viscosity hypothesis. k-ε schemes are often referred to as the "workhorse" of turbulence models for industrial CFD applications due to a good balance between computational effort and accuracy for a wide class of flows.

In 1986 Yakhot & Orszag developed a new k-ε model called the Renormalization Group (RNG) k-ε model. As its name suggests, Yakhot et al's approach involved the application of a statistical technique called renormalization group theory to the instantaneous Navier-Stokes equation (8). Relative to the standard k-ε model, the RNG model improves accuracy in the case of rapidly-strained and swirling flows. In addition to this analytical derivations for both turbulent Prandtl numbers and effective viscosities are employed instead of user-defined or empirical values, making the RNG model more accurate and reliable for a wider class of flows than the standard k-ε model (ANSYS, 2011). In this formulation k and ε are obtained by solving the following PDEs for the transport of each variable, respectively, assuming incompressible and neutrally-stratified flow:

$$\frac{\partial}{\partial t}(\rho k) + \frac{\partial}{\partial x_i}(\rho k U_i) = \frac{\partial}{\partial x_j}\left(a_k \mu_{eff} \frac{\partial k}{\partial x_j}\right) + G_k - \rho\varepsilon + S_K, \tag{15}$$

$$\frac{\partial}{\partial t}(\rho \varepsilon) + \frac{\partial}{\partial x_i}(\rho \varepsilon U_i) = \frac{\partial}{\partial x_j}\left(a_\varepsilon \mu_{eff} \frac{\partial \varepsilon}{\partial x_j}\right) + C_1 \frac{\varepsilon}{k} G_k - C_{2\varepsilon}\rho \frac{\varepsilon^2}{k} - R_\varepsilon + S_\varepsilon, \tag{16}$$

where μ_{eff} is the effective viscosity, G_k is turbulent kinetic energy (TKE) due to mean velocity gradients, a_k and a_ε are inverse effective Prandtl numbers, and S_k and S_ε are user-defined source/sink terms. R_ε is an additional term arising from their statistical approach and is given by

$$R_\varepsilon = \frac{C_\mu \rho \eta^3 \varepsilon^2 (1 - \eta/\eta_0)}{k(1 + \beta\eta^3)}, \tag{17}$$

where $\eta = Sk/\varepsilon$. Constants for Equations 15 – 17 are as follows: $a_k = a_\varepsilon \approx 1.393$, $\eta_0 = 4.38$, $\beta = 0.012$, $C_{1\varepsilon} = 1.42$, and $C_{2\varepsilon} = 1.68$. Finally, v_t is determined as

$$\nu_t = C_\mu \frac{k^2}{\varepsilon}, \tag{18}$$

for $C_\mu = 0.0845$, thus completing closure to the model.

2.5.3.6 Reynolds Stress Model

The Reynolds stress model (RSM) is one of the more elaborate widespread closure schemes for RANS simulations. Abandoning the turbulent viscosity hypothesis altogether, the Reynolds stress model instead solves transport equations for each of the six Reynolds stresses in conjunction with an equation for the dissipation rate for a total of 7 extra equations. It is a second-order closure scheme that is derived by taking moments of the instantaneous Navier-Stokes equation (8) (ANSYS, 2011). Throughout this process, unfortunately, several unknown variables appear in the exact transport equations and ultimately must be modeled as well. Furthermore, due to the large number of extra equations that must be solved the RSM tends to be much more computationally expensive than other turbulence models yet does not always produce significantly better results. Despite these issues the RSM can be useful when other models fail, such as rotating flows or other instances where the Reynolds stresses are highly anisotropic. The exact Reynolds-averaged transport equations can be written as

$$\frac{\partial(\rho\overline{u_i'u_j'})}{\partial t} + \frac{\partial(\rho U_k \overline{u_i'u_j'})}{\partial x_k} = D_{L,ij} - D_{T,ij} - P_{ij} + \phi_{ij} - \varepsilon_{ij} \tag{19}$$

where $D_{L,ij}$ and $D_{T,ij}$ are molecular and turbulent diffusion, respectively, P_{ij} is the stress production, ϕ_{ij} is the pressure strain, and ε_{ij} is the dissipation rate. In Equation 19 $D_{T,ij}$, ϕ_{ij} and ε_{ij} are unknown and need to be modeled in order to provide closure. ε_{ij} is modeled in essentially the same manner as in the *k-ε* model; for information on modeling techniques for $D_{T,ij}$ and ϕ_{ij} see ANSYS, 2011.

2.5.4 Modeling Scalar Transport

In hydraulic contact tanks, disinfectants can often be modeled as a passive, conservative scalar. A *passive scalar* is one that is affected and transported by the flow but does not affect it in return, while a *conservative scalar* is one that is not created or destroyed by chemical processes nor converted to another state of matter. Applying Reynolds decomposition to place a time-averaging filter on the advection-diffusion equation of a passive conservative scalar results in another closure problem as is the case in Equation 13. To resolve this, a similar hypothesis is taken as with Equation 14 wherein certain physical processes in turbulent flow are assumed to behave as they are observed at the molecular level. The *gradient-diffusion hypothesis* draws parallels to Fick's Law, which states that molecular diffusive flux is proportional to the gradient of the scalar's concentration by the fluid's diffusivity (Pope, 2000). Applying this to RANS turbulence modeling, the mean scalar flux is thought to be proportional to the mean scalar gradient by the turbulent diffusivity (κ_t):

$$\overline{u_j' C'} = -\kappa_t \frac{\partial C}{\partial x_j}, \tag{20}$$

where C is the average scalar concentration. Like with turbulent viscosity, the turbulent diffusivity is a property of the flow rather than of the fluid itself. With these assumptions in mind

the concentration of a scalar representing an actual disinfecting agent may numerically modeled as a function of time and space by solving

$$\frac{\partial C}{\partial t} + \bar{U}_J \frac{\partial C}{\partial x_j} = \frac{\partial}{\partial x_i}\left(\kappa_{eff} \frac{\partial C}{\partial x_i}\right). \tag{21}$$

Here κ_{eff} is the summation of molecular and turbulent diffusivities. κ_t is often rewritten as

$$\kappa_t = \frac{\nu_t}{Sc_t}. \tag{22}$$

Sc_t is known as the turbulent Schmidt number, which is the ratio of the turbulent viscosity and diffusivity. Although a wide range of discussion exists in literature concerning the correct value of Sc_t, Venayagamoorthy and Stretch (2010) showed that 0.7 is a reasonable approximation in neutrally-stratified flows. This value was incorporated into the CFD models presented in the following chapters by means of a user-defined function (see Appendix A).

2.5.5 ANSYS Software

Several commercial software packages exist for CFD modeling, including but not limited to CFX, OpenFOAM, FLOW-3D, COMSOL, STAR-CD, and PHOENICS (Versteeg and Malalasekera, 2007). FLUENT software by ANSYS was chosen for simulations in this thesis for its use of the finite volume method, ability to handle user-defined functions, wide variety of model options and solver settings, support of large meshes, and widespread use and acceptance of its capabilities. Workbench software by ANSYS was used to create and subsequently mesh all geometries before being directly exported to FLUENT for modeling. Each simulation used FLUENT's pressure-based solver; for more information on this see ANSYS, 2011.

2.5.6 Shortcomings of CFD Simulations

Although CFD is an invaluable tool to gain insight into flow behavior, caution must always be taken by the modeler when assessing results. As mentioned before, resolved flow fields can often appear physically realistic when they actually are not. Some potentially significant sources of error include:

1. Truncation: In order to discretize continuous functions to be solved on a computational grid, power series are used to express derivatives or integrals with an infinite series of terms. Due to the inherently unmanageable nature of an infinite series only the first few terms are used and the rest are discarded, thereby creating truncation error (Moin, 2010).
2. Computer round-off: In computer science, a floating point number is used to approximate an actual number by managing a tradeoff between range and precision. Real numbers must often been held to a certain number of significant digits, leading to computer round-off error (Ueberhuber, 1997).
3. Turbulence modeling: Bringing the level of indeterminacy of a filtered set of governing equations to zero requires a closure scheme as discussed in Section 2.5.3.3. A large number of such schemes exist, each with their own benefits and shortcomings, but some degree of error is inherent in all of them.
4. Physical modeling: Empirical equations used to model flow are often utilized in CFD. If such equations are not fitted with the correct coefficients or otherwise calibrated correctly the flow may not be predicted at an acceptable level of accuracy.
5. User input: A large amount of input is needed from the modeler before a computer may simulate flow. This includes but is not limited to boundary conditions, initial conditions,

and geometry and meshing. Poor prescription of this data by the user can lead to invalid results.

Due to these errors a typical CFD simulation is not considered sufficiently accurate until physical validation is performed. This is essential in verifying whether or not the collective sources of error have impacted the results enough to be of concern. Furthermore, during the discretization process the modeler must determine grid spacing and time steps. These must be chosen in such a way that a grid or time step refinement would result in a negligibly different solution while (preferably) incurring minimal computational cost. If this requirement is not met, the solution cannot be considered valid (Versteeg and Malalasekera, 2007). Despite these issues CFD is unrivaled in terms of prospective insight gained into fluid mechanics and as such is used in-depth throughout this thesis to explain results.

CHAPTER 3: INTERNAL HYDRAULICS OF BAFFLED CONTACT TANKS[1]

3.1 Introduction

Baffles are used in many contact tanks to promote plug (uniform) flow and minimize short circuits and dead zones. The effective contact time in a tank is usually taken to be t_{10} (the time required for the first ten percent of the disinfectant to travel through the tank to the residual sampling point) rather than the theoretical detention (or residence) time (*TDT).* The efficiency of contact tanks is commonly quantified by the baffling factor (*BF*), which is defined as the ratio of t_{10} to *TDT* and provides a measure of the short-circuiting in the tank. Un-baffled tanks usually have a *BF* on the order of 0.1, while tanks with ideal plug flows have a *BF* close to 1.0. Another measure of hydraulic efficiency is a mixing indicator commonly known as the Morrill index (*MI*, Teixiera and Siqueira 2008, Gualtieri 2010) which evaluates the amount of diffusion in a contact tank based on the ratio $t_{90}/t_{10,}$ where t_{90} represents the time it takes for the first ninety percent of the fluid to pass through the tank to the outlet. A prudent way to optimize hydraulic disinfection efficiency is to increase the value of t_{10} for the contact tank while minimizing the value of t_{90}, which can be accomplished by decreasing short-circuiting and promoting fully-developed flow through the use of baffles and by altering the size, location, and/or orientation of the inlet and outlet (Hannoun et al, 1998; Singer, 1994; Angeloudis et al, 2014).

Baffles placed in the interior of contact tanks provide for a longer contact path and reduced flow separation within the tank, both of which may in theory extend the disinfection contact time and lead to near-plug flow conditions. The number and geometry of the internal baffles, the inlet and outlet locations, and the tank geometry are factors that influence the

[1]The results presented in this chapter have been submitted in substantial part as "Internal Hydraulics of Baffled Disinfection Contact Tanks" by Z. Taylor, J. Carlston, and S.K. Venayagamoorthy to the Journal of Hydraulic Research.

hydraulic efficiency (Crozes et al, 1999). Recent studies have considered the effect of changing one tank design parameter on *BF* and other hydraulic efficiency indicators. Amini et al (2011) analyzed the effect of changing the number of baffles, Kim et al (2013) considered the effect of baffle spacing by varying the compartment width, and many other studies have considered the length-to-width ratio of baffle compartments. In all these studies, baffle spacing was the only design parameter that was varied. Another key geometric variable that has not received much attention in literature but should be considered in relation to other relevant geometric parameters is the baffle opening length (denoted by L_{bo}). A key question that is important to address is whether there exists an optimal baffle design configuration that will result in an internal flow field that is closest to plug flow conditions for a tank with a given footprint and uniform inlet width (i.e. where the flow in the tank is predominantly in the horizontal plane)? In the present study, the emphasis is to determine the most relevant geometric design variables that will yield optimal hydraulic efficiency in such a tank. This is important as it is evident that there are numerous inadequately designed tanks that are at risk of producing cancerous disinfection by-products (Rauen et al, 2012).

In this study, the footprint of a laboratory-scale disinfection tank is used that was investigated in a number of other studies, including but not limited to those by Shiono et al (1991), Shiono and Teixeira (2000), and Khan et al (2006) in their experimental and numerical studies but with one important difference, namely: a uniform inlet is used in order to promote plug flow early in the first compartment, thereby eliminating the step-like flow conditions observed in the experiments. In this study, the baffle opening length (L_{bo}) and the inlet width (W_{ch}) for the given footprint are varied to quantify the hydraulic efficiency of the tank primarily using two-dimensional CFD simulations. The layout of this chapter is as follows: first, numerical

methodology employed for the CFD simulations is introduced and model validation via previous experimental results is presented. The conceptual formulation and details of the parametric study is spelled out, followed by results of the parametric study. A summary detailing overall findings concludes the chapter.

3.2 Numerical Framework

The well-known CFD software FLUENT by ANSYS was employed to perform highly resolved two and three-dimensional simulations. FLUENT is a finite-volume code that solves the Navier-Stokes equations with any number of other equations required for the desired modelling project. In this context the code solved the Reynolds-averaged Navier-Stokes equations and the scalar transport (advection-diffusion) equation in a contact tank using an unstructured quadrilateral mesh as seen in Figures 3.1(b) and (d)). The renormalization group (RNG) k-ε model was chosen for turbulence closure as it handles flows with separation and recirculation better than the standard k-ε model (ANSYS, 2011; Bradbrook et al 1998; Yakhot and Orszag, 1986).

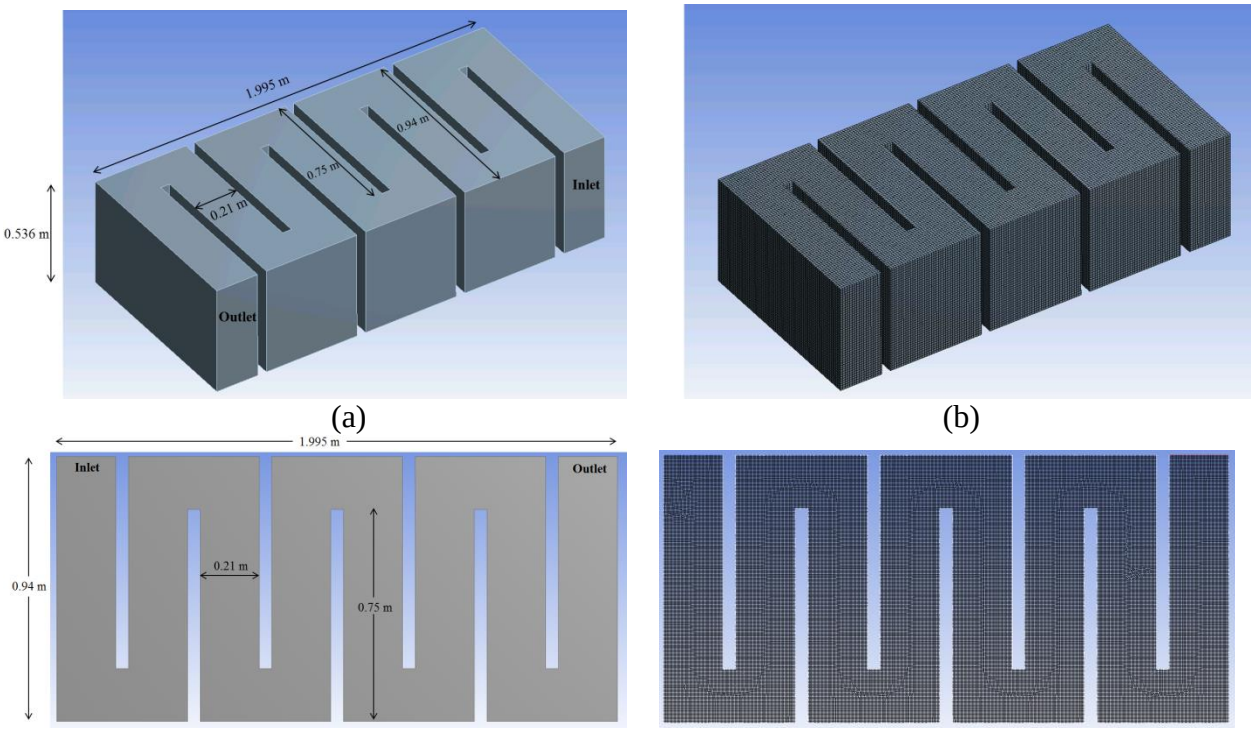

Figure 3.1: Benchmark contact tank with 7 baffles used in this CFD study: (a) 3D schematic; (b) 3D computational mesh; (c) 2D schematic; (d) 2D computational mesh

The simulations were performed in two steps. First, the steady-state turbulent velocity field was calculated using the RANS equations. Enhanced wall-function boundary conditions (that assume that the near wall flow is within the viscous sublayer and hence use more detailed formulations to resolve the near-wall effects) were imposed on all walls and baffles (ANSYS, 2011). The water surface was treated with a symmetry boundary condition. Constant volume flow rate, turbulent kinetic energy (k) and turbulent kinetic energy dissipation rate (ε) were specified at the inlet, while the outlet was treated as a pressure outflow discharging to the atmosphere. Second, with the converged steady-state velocity field from the first step, the tracer concentration was calculated using the advection-diffusion equation for a passive conservative scalar as given by the following (Pope, 2000):

$$\frac{\partial C}{\partial t} + \bar{U}_j \frac{\partial C}{\partial x_j} = \frac{\partial}{\partial x_i}\left([\kappa + \frac{\nu_t}{Sc_t}] \frac{\partial C}{\partial x_i} \right), \quad (23)$$

where C is the average conservative tracer concentration (e.g. chloride or lithium), $\bar{U}$ is the average steady-state turbulent velocity field, ν_t is the turbulent eddy viscosity and Sc_t is the turbulent Schmidt number. The solutions of Equation 23 were used to obtain the RTD curve at the outlet of the tank corresponding to a step tracer input at the inlet where the concentration was set as $C_0 = C_{max} = 1$. The value of the scalar was monitored using an area-weighted average over the cross-section of the outlet. Variation of concentration as a function of time provides an RTD curve of a step dose tracer input as discussed in Section 2.3.2.

In Equation 23 both $\bar{U}$ and ν_t are obtained from the steady-state solution of the momentum equations from the first step. The value of the turbulent Schmidt number Sc_t used in previous simulation studies has ranged from 1.0 (Gualtieri 2006; Stamou 2008; Rauen et al; 2012) to as low as 0.3 in a recent large-eddy simulation study by Kim et al (2013). In this study, Sc_t is taken to be 0.7, a value accepted to be appropriate for neutrally-stratified flow conditions based on theoretical arguments (Venayagamoorthy and Stretch, 2010; Angeloudis et al, 2014). Nonetheless a simulation study was undertaken to explore the sensitivity of the results to different values of Sc_t (0.3, 0.7 and 1.0) which demonstrated that the residence time distribution curves were very close to each other as seen in Figure 3.2 (less than 10% difference is observed at the widest departure points). Both the advection-diffusion equation and the momentum equations were discretized using a second-order upwind scheme. Each 2D simulation took no more than 1 hour to run on a standard workstation using a quad core processor with 16GB of memory.

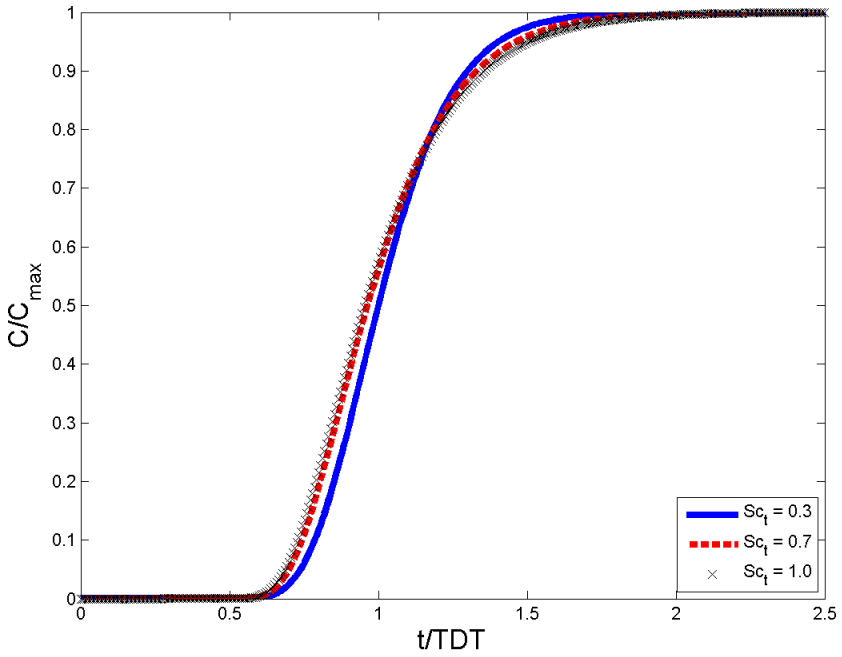

Figure 3.2: Sensitivity of RTD Curves to Turbulent Schmidt Number

3.3 CFD Model Configuration and Validation

Figures 3.1(a) and (c) shows the 3D and 2D schematics of the model tank utilized in this study (the benchmark tank) and represent the main aspects of the seven short-baffle tank configuration used by Shiono et al (1991) in their experimental study. As discussed earlier, the main difference is the use of a uniform inlet in the simulation as opposed to the step weir inlet that was employed in the previous experiments. Physical tracer studies were conducted by Shiono et al (1991) with a continuous discharge of $Q = 1.17 \cdot 10^{-3}$ m^3/s entering the tank, resulting in a mean water depth of 0.536 m and an initial mean cross-sectional velocity of 0.109 m/s at the inlet channel. The *TDT* in the baseline tank was 774 seconds. The flow rate used in all the CFD simulations for the parametric study was the same flow rate used in the physical tracer studies. The geometry and mesh files in this study were generated using ANSYS Workbench, the latter of which were then directly exported to FLUENT for use in simulations. The 3D mesh shown in

Figure 3.1(b) of the benchmark geometry consisted of 520,000 quadrilateral cells while the highly resolved 2D mesh of the benchmark geometry consisted of 80,000 cells as shown in Figure 3.1(d). The 2D mesh configuration of 80,000 cells was verified with a mesh independence study.

Figure 3.3(a) shows a comparison of the RTD curves between the 3D and 2D simulations for the tank configurations indicated in Figure 3.1(a) and (c). The agreement is clearly excellent but not surprising since the depth of flow at the inlet section is the same as the flow depth in the tank for the 3D simulation (i.e. the step in the experimental study of Shiono et al 1991 was eliminated). This excellent agreement provides justification for the use of 2D simulations in the presented parametric study since the flow will be primarily horizontal. Figure 3.3(b) shows excellent comparison between RTD curves for three different mesh sizes using 2D simulations indicating grid independence of the simulation results.

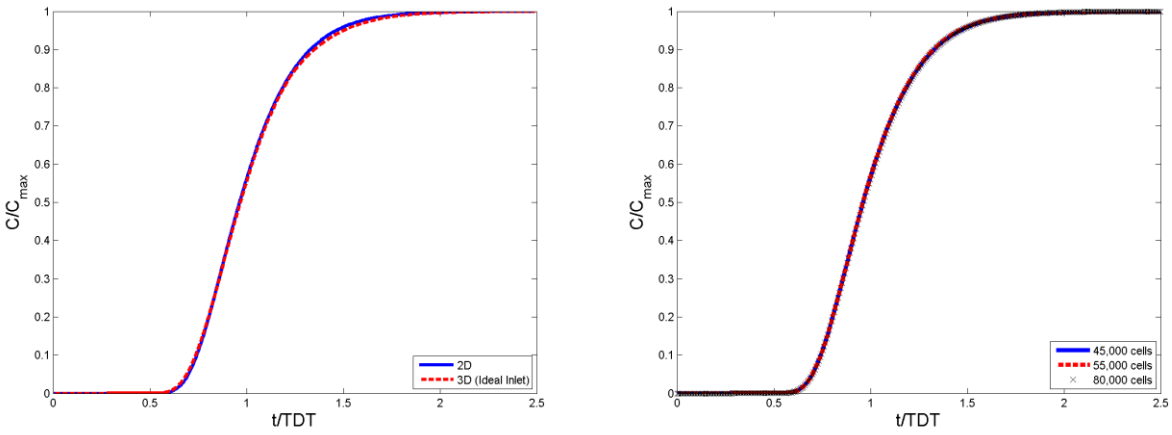

(a) (b)

Figure 3.3: Normalized RTD Curves for (a) 2D and 3D Simulations, Justifying 2D Analysis, and (b) 2D Simulations at Various Mesh Refinements, Demonstrating Grid Independence

In the first step of physical validation, the flow-through curve (FTC) obtained from a pulse-input tracer study from Shiono et al (1991) was compared to the numerically-predicted FTC of a passive scalar for the same tank. Shown in Figure 3.4, a relatively good agreement is

noted between the two data sets. At a cursory glance it may concerning that the rising limbs deviate somewhat before the peak concentration near $t = TDT$ is observed; however, this is to be expected since the ideal inlet as prescribed in the modeled tank promotes plug flow in the first compartment thereby causing a delayed breakthrough. On the other hand, in the physical test a step-like weir at the inlet described previously results in a highly 3D flow field, causing inferior mixing conditions until the flow stabilizes to essentially two-dimensional behavior. The consequence of this is seen by earlier breakthrough of empirical data in Figure 3.4.

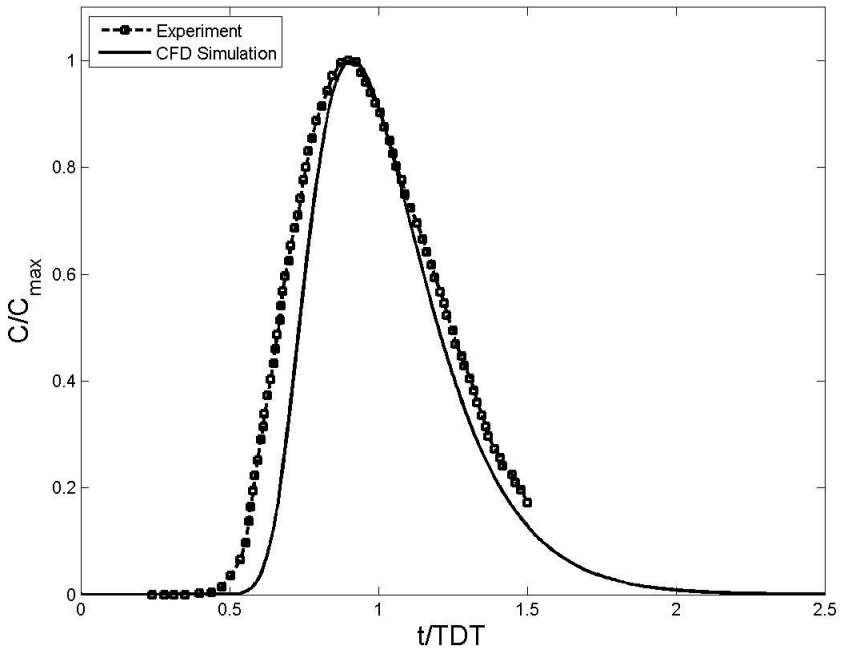

Figure 3.4: Empirical versus Predicted Flow-Through Curves for the Baseline Tank

In an effort to further validate the CFD model (noting similar residence times do not always imply predictive capabilities of CFD models; see Khan et al, 2006) data for the longitudinal velocity in a cross-section in the center of fifth compartment of the tank from the experiments of Shiono et al (1991) was compared to numerical results. Figure 3.5 shows good

agreement between the simulated and empirical velocities, where the notation used in Wang and Falconer (1998) was followed to normalize the cross-sectional axis of the compartment by the cross-sectional width. The deviations of the CFD results compared to the physical model results can be attributed to the depth-averaging of the values. Regardless, there is reasonable prediction of the asymmetrical distribution of the flow velocity across the cross-section with good agreement for the higher velocities, indicating that the turbulent (Reynolds) stresses are predicted reasonably well.

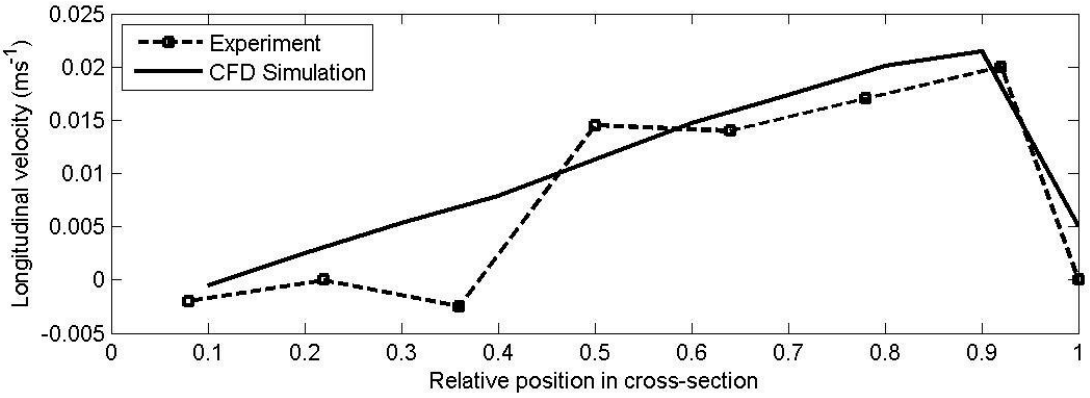

Figure 3.5: Empirical versus Predicted Longitudinal Velocities at the Center of the 5th Compartment in the Baseline Tank

Finally, in order to ensure that the hydrodynamic characteristics in the 2D simulations were relatively independent of the flow rate, simulations with different flows rates of up to 4 times the original flow rate of $Q = 1.17 \cdot 10^{-3}$ m^3/s were performed. Although a small dependence on flow rate is observed, the normalized RTD curves as seen in Figure 3.6 are in excellent agreement. In order to optimize computational efficiency and ensure accuracy, the settings used in Workbench to develop the benchmark 2D mesh with 80,000 cells were used to generate the meshes for all the modified geometries used in all the 2D simulations for the parametric study, which is discussed next.

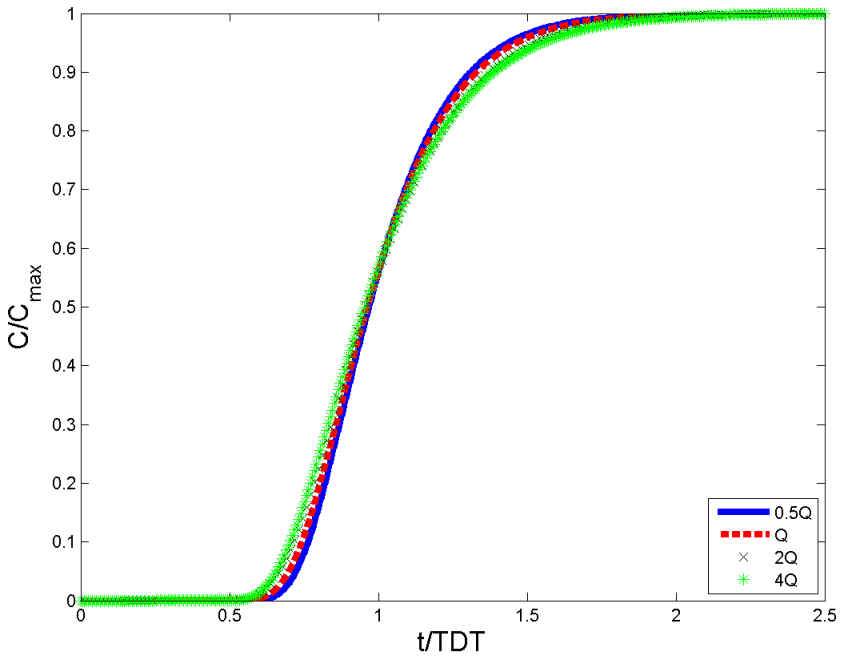

Figure 3.6: Dependence of Scalar Transport on Flow Rate

3.4 Parametric Study

3.4.1 Conceptual Formulation

Given a footprint of a rectangular contact tank with length L_T (measured parallel to the orientation of baffles) and width W_T (measured perpendicular to the orientation of baffles) with a fixed inlet width W_{inlet}, as shown in the schematics depicted in Figure 3.7(a) and (b), respectively, it is intuitive to choose the baffle channel width W_{ch} such that $W_{ch} = W_{inlet}$ in order to promote plug flow. This choice immediately implies that the number of baffles that should be placed in the tank is also fixed provided that, naturally, the baffle wall thickness W_b is a constant. Furthermore, the ratio L_T/W_{ch} is also fixed for a given inlet width W_{inlet}. It should be expected that the long baffle orientation shown in Figure 3.7(b) should be optimal given that the ratio L_T/W_{ch} will be higher compared to the short baffle orientation shown in Figure 3.7(a). However, the long baffle orientation will have fewer compartments compared to the short baffle orientation, with

the actual number of compartments dependent on the inlet width (e.g. for the tank schematics shown in Figure 3.7(a) and (b), there are 8 compartments for the short baffle orientation and 4 compartments for the long baffle orientation).

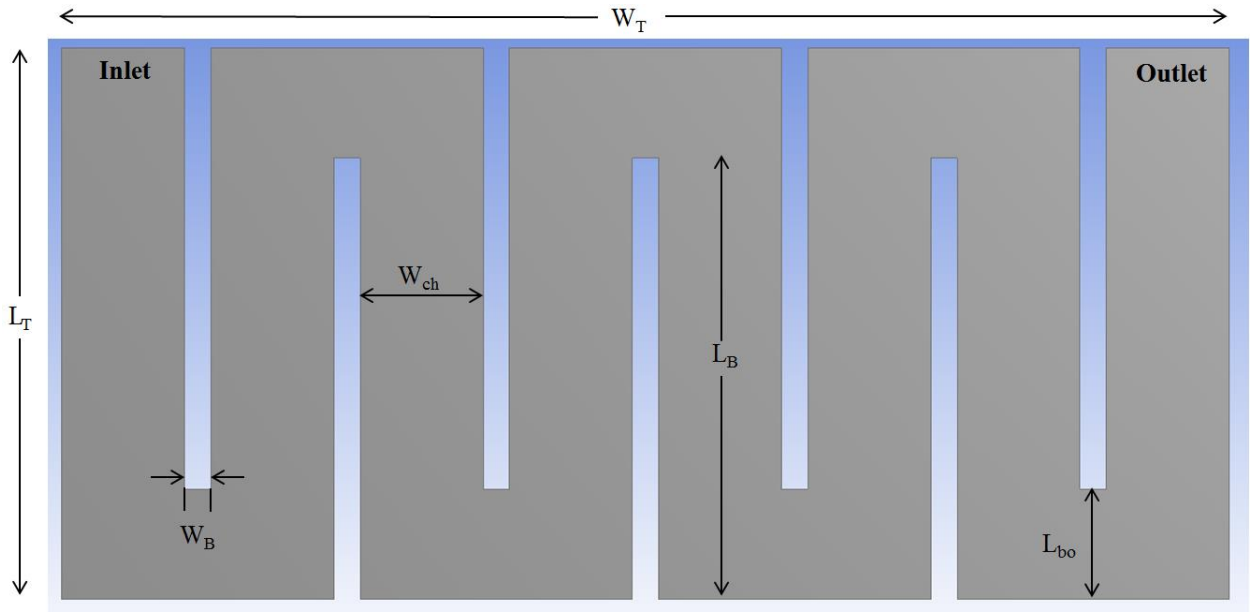

(a)

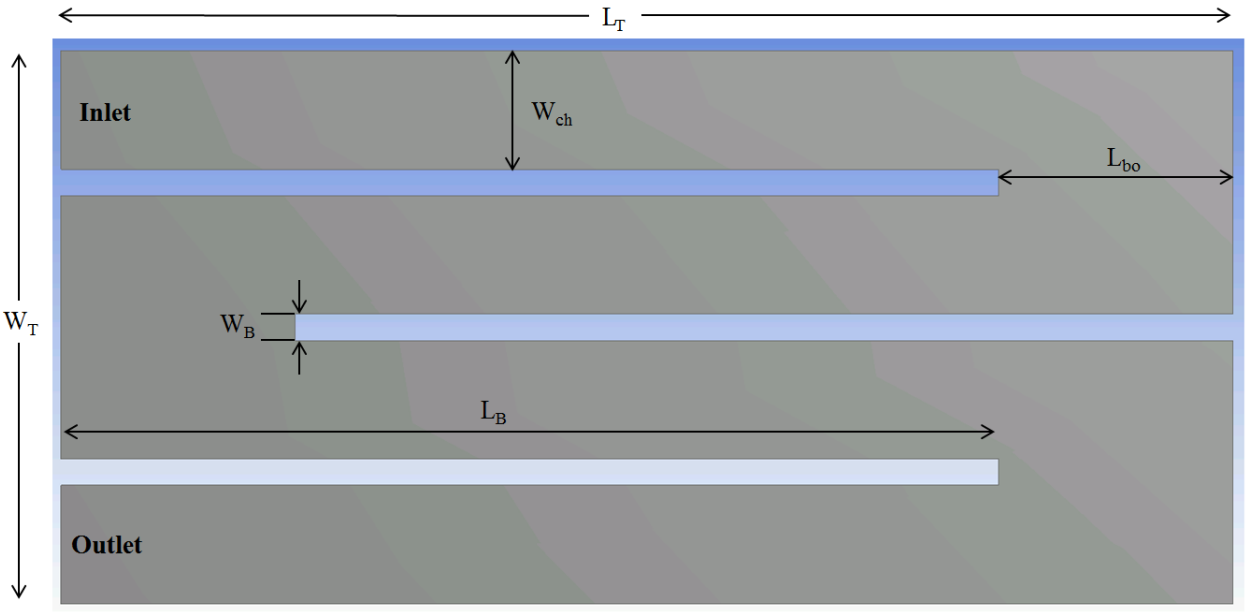

(b)

Figure 3.7: Schematics of the Tank for (a) Short Baffle and (b) Long Baffle Orientations

Based on the above points, the key question is what is the most important geometric variable that should be optimized to obtain the best hydraulic efficiency (i.e. highest *BF* and lowest *MI*)? Clearly, that variable is the baffle opening length L_{bo}. There are only two ratios that this quantity can be logically related to based on the prescribed setup. These are L_{bo}/L_T and L_{bo}/W_{ch}. It is prudent to first consider the first ratio L_{bo}/L_T which is the comparison of the turning radius around the baffles to the distance the water must travel along each compartment of the tank.

Obviously, it is important for baffles to be designed such that $L_{bo}/L_T \leq 0.5$ in order to ensure that the flow is prevented from channeling between the baffles that will result in large short circuits and dead zones. To demonstrate this, Figure 3.8 shows velocity magnitudes predicted by a 2D CFD simulation with $L_{bo}/L_T = 0.6$. It can be clearly seen that the majority of flow bypasses the compartments created by each baffle. As a result low velocities in portions of the tank away from the primary flow route imply large dead zones and/or recirculation. This supports the notion that one should ensure baffles on either side of the tank extend past each other by imposing the restriction that $L_{bo}/L_T \leq 0.5$. This study therefore only considers $L_{bo}/L_T \leq 0.4$.

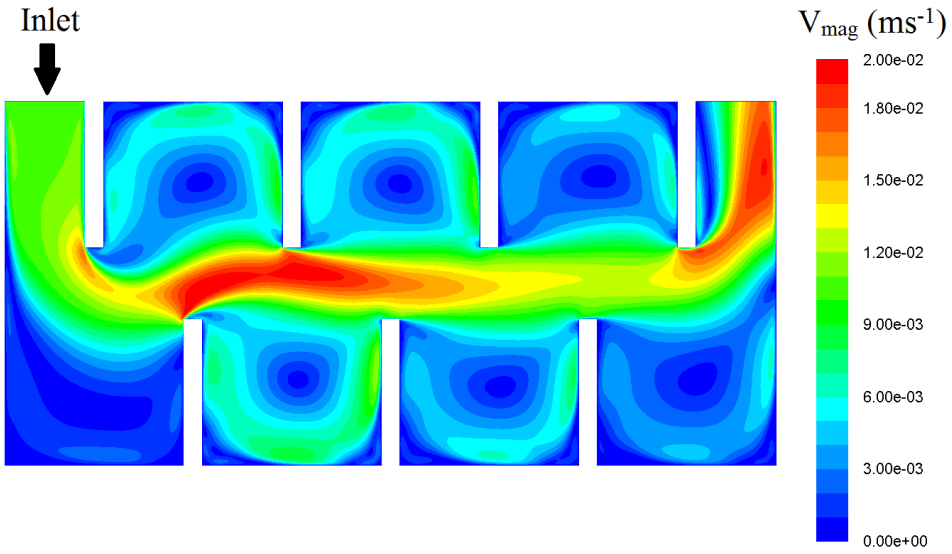

Figure 3.8: Simulated Flow Conditions for L_{bo}/L_T = 0.6

The second ratio L_{bo}/W_{ch} provides an indication of the extent of expansion/contraction of the flow in the contact tank as the flow turns from a channel of width W_{ch} through a baffle opening of length L_{bo} at the baffle tips. The goal should be to minimize such changes in order to minimize dead zones that arise due to flow separation around baffle tips. Based on physical reasoning, it is hypothesized that an optimal hydraulic efficiency (i.e. closer to plug flow conditions) should occur when $L_{bo}/W_{ch} \approx 1$ with W_{ch}/W_{inlet}=1.

3.4.2 Details of Parametric Study

In order to determine the effects of the proposed dimensional relationships on *BF* and *MI*, the baffle opening length L_{bo} and the inlet width W_{inlet} in a tank were set as variable parameters and a parametric study consisting of a total of 30 simulations was performed. For each inlet width W_{inlet} (which is also equal to the channel width W_{ch} as discussed in Section 3.4.1), five different values of the baffle opening length L_{bo} (i.e. 40%, 20%, or 10% of L_T and a final value of L_{bo}=W_{ch}) were used. Three different inlet widths were used for both the short and long baffle configurations, i.e. as close as possible to $0.5W_{inlet\_0}$, $1.0W_{inlet\_0}$ and $1.5W_{inlet\_0}$ under the given geometric constraints, where W_{inlet_0} is the original inlet width of 0.21 m used in the

experimental study by Shiono et al, 1991). These corresponded to a total of 13, 7 and 5 baffles for the short baffle orientation study and a total of 6, 3 and 2 baffles for the long baffle orientation study, respectively. In summary, for each of the three values of channel width used, five simulations were performed per baffle orientation to investigate the effect of L_{bo}/W_{ch} on *BF* and *MI*. Tables 3.1(a) and (b) summarize the geometries and resultant *TDT*s for the 30 simulations performed.

Table 3.1: Geometric Data for (a) Short Baffle and (b) Long Baffle Orientations

Short Baffles					
	W_{ch} (m)	**N_b**	**L_{bo}/L_T**	**L_{bo}/W_{ch}**	**TDT (s)**
L_T = 0.94 m W_T = 1.995 m W_b = 0.045 m	0.101 (Narrow) $0.48W_{inlet\_0}$	13	0.10	0.93	632.38
			0.20	1.87	657.58
			0.30	2.80	682.77
			0.40	3.73	707.96
			0.11	1.00	634.18
	0.210 (Normal) $1.00W_{inlet\_0}$	7	0.10	0.45	737.03
			0.20	0.90	750.59
			0.30	1.34	764.16
			0.40	1.79	777.72
			0.22	1.00	753.77
	0.295 (Wide) $1.40W_{inlet\_0}$	5	0.10	0.32	771.91
			0.20	0.64	781.60
			0.30	0.96	791.29
			0.40	1.27	800.98
			0.31	1.00	792.63

(a)

Long Baffles					
	W_{ch} (m)	N_b	L_{bo}/L_T	L_{bo}/W_{ch}	TDT (s)
L_T = 1.995 m W_T = 0.94 m W_b = 0.045 m	0.096 (Narrow) $0.46W_{inlet\_0}$	6	0.10	2.08	637.02
			0.20	4.17	661.70
			0.30	6.25	686.38
			0.40	8.34	711.05
			0.05	1.00	624.18
	0.201 (Normal) $0.96W_{inlet\_0}$	3	0.10	0.99	748.07
			0.20	1.98	760.41
			0.30	2.97	772.74
			0.40	3.97	785.08
			0.10	1.00	748.18
	0.283 (Wide) $1.35W_{inlet\_0}$	2	0.10	0.70	785.08
			0.20	1.41	793.31
			0.30	2.11	801.53
			0.40	2.82	809.76
			0.14	1.00	788.54

(b)

3.5 Results and Discussion

The results of the parametric study show that the ratio L_{bo}/W_{ch} is the key parameter for baffle tanks with predominantly horizontal flow conditions. In what follows, the main results from the parametric study that support this finding are presented.

Figure 3.9 shows velocity magnitude contours (in m/s) for both the short (7 baffle) and long (3 baffle) configurations corresponding to the original inlet width of 0.21 m used by Shiono et al (1991). Figure 3.9(a) shows the results for L_{bo}/W_{ch} = 1 for the short baffle orientation while

Figure 3.9(b) shows the results for $L_{bo}/W_{ch} \approx 1.8$ for the short baffle orientation. Similarly, Figure 3.9(c) shows the results for $L_{bo}/W_{ch} = 1$ for the long baffle orientation while Figure 3.9(d) shows the results for $L_{bo}/W_{ch} \approx 4.0$ for the long baffle orientation. It is clear that the when $L_{bo}/W_{ch} = 1$, the flow is more developed especially for the long baffle orientation (as shown in Figure 3.9(c)) compared to when $L_{bo}/W_{ch} > 1$ where it is evident that the flow is channelled between the baffle tips resulting in large dead zones as shown in Figure 3.9(b) and (d), respectively.

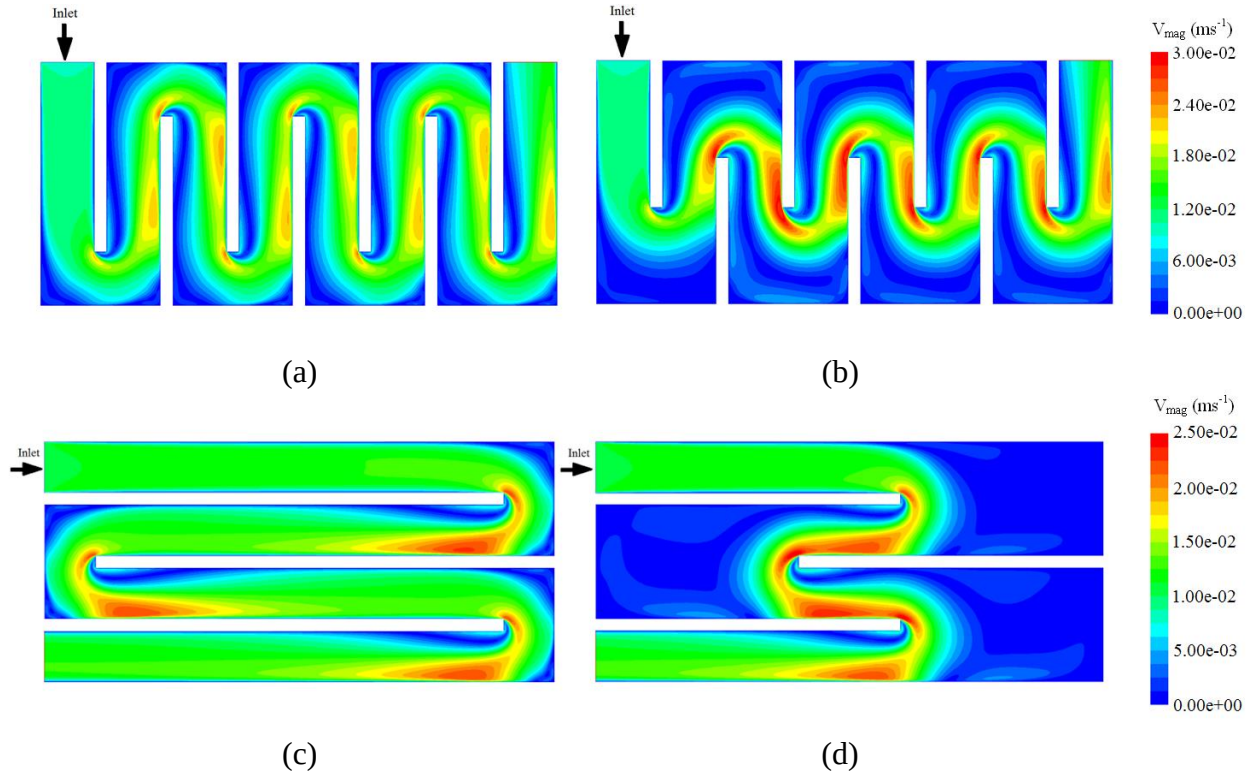

Figure 3.9: Velocity magnitude contours (m/s) for (a) short baffle orientation and $L_{bo}=W_{ch}$; (b) short baffle orientation and $L_{bo}=0.4L_T$; (c) long baffle orientation and $L_{bo}=W_{ch}$; (d) long baffle orientation and $L_{bo}=0.4L_T$. For (a) and (c) baffle lengths are optimized while for (b) and (d) flow is channeled between baffle tips, creating large dead zones.

Figures 3.10(a) and (b) show the *BF* and *MI* as functions of L_{bo}/W_{ch} for each of the three different channel (inlet) widths for the short baffle orientation. The color of each data point denotes the ratio of L_{bo}/L_T as indicated by the color bar on the right of the figure. The *BF* is optimal (highest) and the *MI* is optimal (lowest) when $L_{bo}/W_{ch} \approx 1$ for all three channel widths.

For the narrow channel case (i.e. $W_{ch} = W_{inlet} \approx 0.5W_{inlet\_0}$), this is clearly evident with the *BF* (*MI*) decreasing (increasing) monotonically with increasing L_{bo}/W_{ch}, with the highest value of *BF* = 0.88 occurring when $L_{bo}/W_{ch} = 1$. However, for both the normal channel (i.e. $W_{ch} = W_{inlet} = W_{inlet\_0}$), and the wide channel (i.e. $W_{ch} = W_{inlet} \approx 1.5W_{inlet\_0}$), the trend is not necessarily monotonic. Nevertheless, the optimal values of the *BF* and *MI* clearly occur when $L_{bo}/W_{ch} \approx 1$.

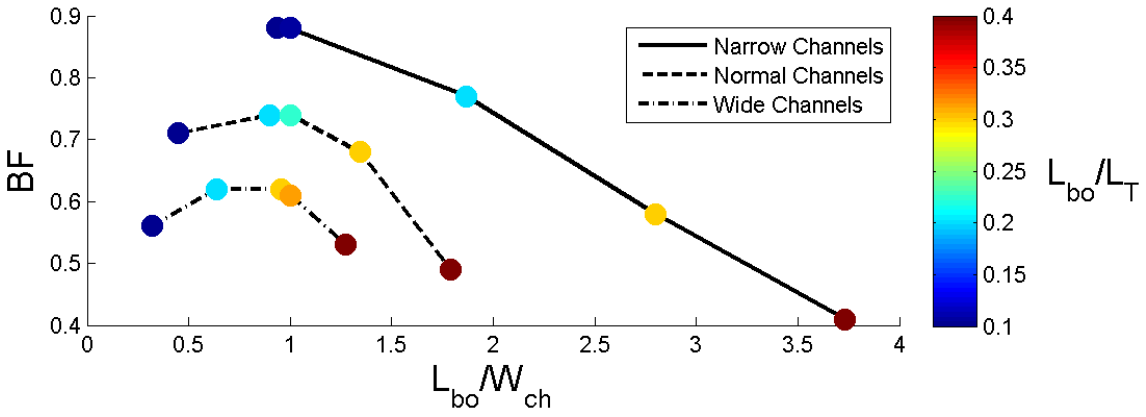

(a)

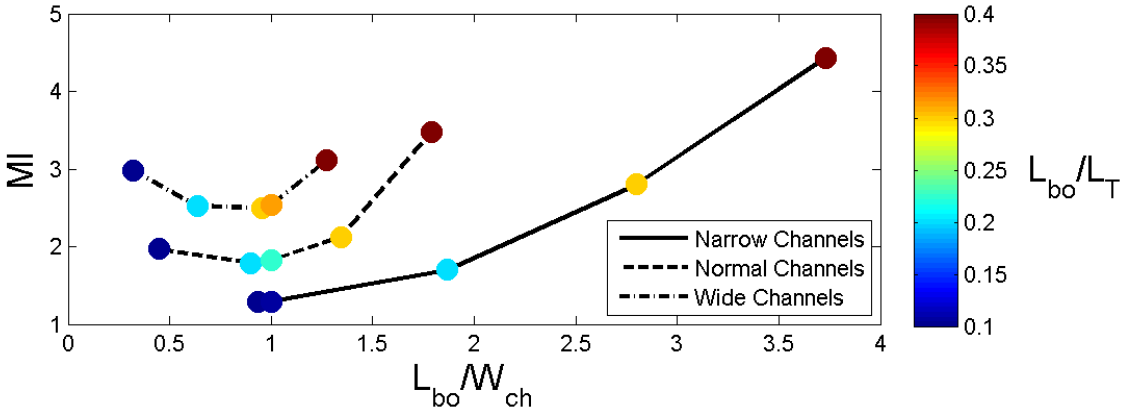

(b)

Figure 3.10: (a) Baffling factors and (b) Morrill indices for the short baffle orientation as a function of L_{bo}/W_{ch}. The color of each data point denotes the L_{bo}/L_T ratio for that simulation as indicated by the color bars on the right.

The results are more striking for the long baffle orientation cases as shown in Figure 3.11(a) and (b) which show similar plots of *BF* and *MI* to Figure 10(a) and (b). As can be seen, both the *BF* and *MI* decrease (increase) monotonically with increasing L_{bo}/W_{ch} for all three channel widths. It is clear that the range of L_{bo}/W_{ch} values are much higher for the long baffle orientation for all three channel width cases compared to the short baffle orientation, and the hydraulic efficiency indicators (as denoted by *BF* and *MI*) are strongly correlated with this ratio. Physically, when L_{bo}/W_{ch} becomes significantly larger or (smaller) than 1, the flow undergoes significant expansions (contractions) at baffle turns resulting in severe flow separation, channelling and dead zones. These results clearly highlight that the importance of designing baffled tanks with $L_{bo}/W_{ch} \approx 1$. Hence, designing a contact tank such that L_{bo} is the same width as the dominant flow field width, i.e. $W_{ch} = W_{inlet}$, will decrease separation thereby maximizing *BF* and minimizing *MI*.

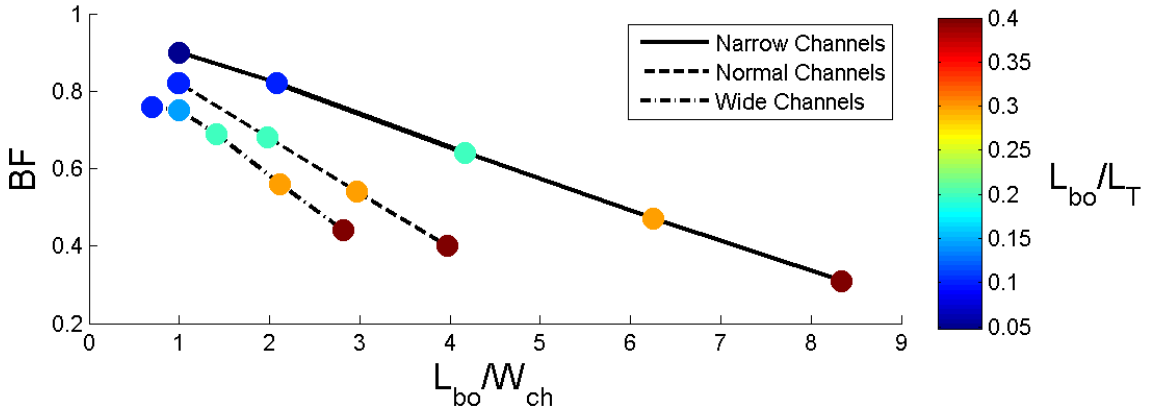

(a)

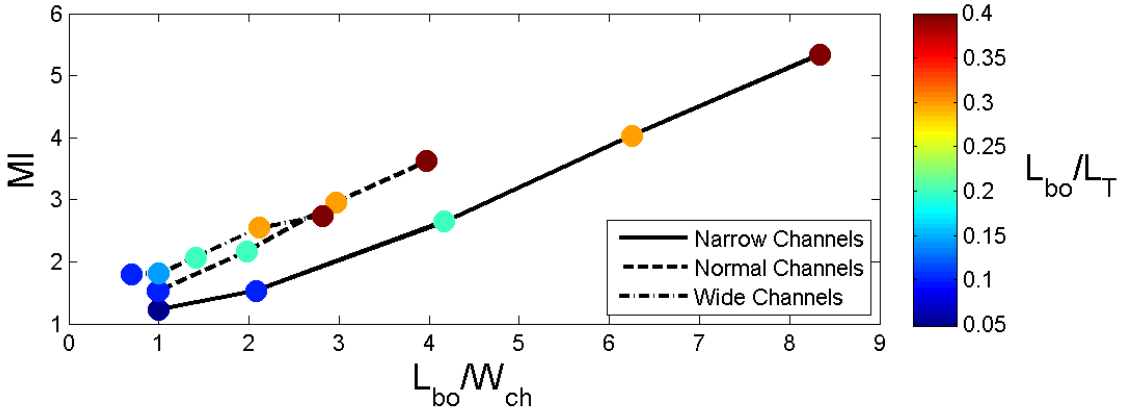

(b)

Figure 3.11: (a) Baffling factors and (b) Morrill indices for the long baffle orientation as a function of L_{bo}/W_{ch}. The color of each data point denotes the L_{bo}/L_T ratio for that simulation as indicated by the color bars on the right.

The overall trends illustrated in Figures 3.10 and 3.11 also indicate that the hydraulic efficiency is higher in general when the ratio L_{bo}/L_T is lower. This is because the flow has a longer straight path between turns, and hence the turbulence and flow separation created in the turns can be more easily dissipated. Furthermore, as predicted, the long baffle orientation cases with $L_{bo}/W_{ch} \approx 1$ show better hydraulic performance compared to the short baffle orientation cases. This is because the length to width ratio in each compartment of the contact tank given by

L_T/W_{ch} is significantly higher for the long baffle orientation cases, thus allowing the flow in each compartment to approach near plug flow conditions before it reaches the next baffle turn in the tank.

3.6 Conclusions

The objective of this study was to identify the dimensional relationships that most affect the hydraulic efficiency of baffled contact tanks and to propose guidelines for contact tank design. Results from highly resolved two-dimensional CFD simulations of turbulent mixing and passive scalar transport in baffled disinfection contact tanks show that the *BF* and *MI* are strongly correlated with the amount of flow separation in the tank. In a long pipe loop, the only significant flow separation is caused by bends. In a contact tank, flow separation can be caused by expansion from the inlet to the tank, expansions/contractions between channels and baffle openings, contraction from the tank to the outlet, and flow around bends. It is proposed that the best contact tanks will resemble pipe loops in their plan view, irrespective of L_T and W_T, implying the ideal tank should be designed such that $W_{inlet} = W_{ch} = L_{bo} = W_{out}$ so that flow separation will only be caused by bends around baffle openings.

The dimensional relationship from this study that most affected hydraulic efficiency is L_{bo}/W_{ch} as long as the channel width W_{ch} is chosen to be equal to the inlet width W_{inlet}. The results from the parametric study highlight that it is imperative for such tanks to be designed such that $L_{bo}/W_{ch} \approx 1$ to ensure optimal hydraulic performance. Furthermore, it was also confirmed that it is also beneficial to orient the baffles parallel to the longer side of a given tank footprint so that L_T/W_{ch} is maximized while ensuring $L_{bo}/W_{ch} \approx 1$ in order to both optimize the hydraulic performance of the tank and minimize costs associated with baffle installation.

While the results of this study are clear, succinct and useful, a crucial assumption that sometimes does not hold true in practice is that $W_{inlet} = W_{ch}$. This is undoubtedly the ideal inlet configuration, but in many hydraulic contact tanks (especially those without access to adequate funding and expertise) subpar inlet conditions exist. In particular a "sharp" inlet, one that is much smaller than the cross-section of channels in the tank, introduces the source water and disinfectant to the system. The result is a jet that produces highly 3D effects near the inlet and can negatively affect system performance throughout the entire tank by inhibiting plug-like flow. In light of this the following question should be answered: What simple yet cost-effective modifications can be made to sharp inlets to boost hydraulic disinfection efficiency? Chapter 4 details research and an accompanying CFD analysis undertaken to resolve this issue.

CHAPTER 4: IMPACT OF SHARP INLETS ON MIXING EFFICIENCY IN BAFFLED HYDRAULIC CONTACT TANKS[2]

4.1 Introduction

As seen in Chapter 3, placing baffles in hydraulic contact tanks is a relatively easy yet effective method of increasing the contact time between the source water and the disinfectant by increased mixing efficiency. These baffles create a channeled environment for fluid flow in order to encourage scalar transport through advection, which in this context is superior to diffusion for mixing purposes (Kattnig, 2014; Amini et al, 2011; Li et al, 2006; Pelinski & Ducoste, 2001). It also limits the creation of "dead zones" of stagnated water by guiding the flow through portions of the tank that would otherwise be short-circuited (Kattnig, 2014; Zhang et al, 2013; Amini et al, 2011; Wols et al, 2010; Kim et al, 2010; Wols et al, 2008; Evans et al, 2003). For small communities where financial budgets for drinking water disinfection are limited, baffled systems provide a cost-effective solution for ensuring adequate contact time. However, parametric studies have shown that increasing the number of baffles in a typical contact tank past about 6 results in diminishing returns of *BF* values (Xu, 2010). It is therefore desirable to investigate other means by which increased mixing efficiency may be achieved in disinfection tanks for drinking water, particularly when chlorine is used for microbial inactivation of the source water.

4.1.1 Sharp Inlets and Inlet Modification

Greene et al (2006) have shown that larger inlets tend to increase hydraulic efficiency by encouraging advective transport. It follows that inlets with a cross-section identical to that of the contact tank's channels are ideal as they more closely resemble plug flow. In practice this is

[2]The results presented in this chapter have been submitted in substantial part as "Impact of Modified Inlets on Residence Times in Baffled Tanks" by J. Carlston and S.K. Venayagamoorthy to the Journal American Water Works Association.

often not possible due to the existing facilities and equipment that connects the disinfection tank to the source water. As a result, “sharp” inlets are commonplace. In this scenario the pipe delivering drinking water to the disinfection system, which has a relatively small diameter, shoots a jet of water into the contact tank. Compared to the rather quiescent water already in the tank, this jet moves at a high speed. Free-shear turbulence is generated due to the large differences in mean velocities between the jet and its slow-moving surroundings (Pope, 2000). The research presented in this chapter intends to make better use of the large levels of turbulence found in the vicinity of sharp inlets relative to the rest of the contact tank in order to further increase the mixing efficiency beyond what can be feasibly attained by increasing the number of baffles. Although the baffling factor is of highest practical importance, the Morrill index is also discussed as a means of evaluating a system’s RTD curve. Physical tracer studies using electrical conductivity (EC) measurements on a full-scale prototype were run to obtain empirical RTD curves. Once validated by these tests, several flow simulations using computational fluid dynamics were utilized to gain insight to the chaotic three-dimensional velocity field and explain the hydrodynamics behind the results obtained.

4.2 Prototype and Geometric Description

The Engineering Research Center (ERC) at Colorado State University houses a disinfection contact tank representative of tanks used by many small municipalities throughout the United States as seen in Figure 4.1(a). It is a simple rectangular prism with an interior length of 132 inches (3.35 m) and interior width of 48 inches (1.22 m). The maximum water level without overflowing is 68 inches (1.73 m) but free surface levels observed in testing ranged from 61.5 to 63.6 inches (1.56 to 1.62 m) for flow rates of 10 and 50 gpm (0.63 to 3.15 L/s), respectively.

As shown in Figure 4.1(b), plumbing in the tank allows for various sharp inlet and outlet arrangements. The inlet diameters are all 2 inches and the centers of their cross-sectional areas are 2 inches from the bottom of the tank. The outlets are all 4 inches in diameter and are centered 6.5 inches from the top of the tank. While multiple inlet and/or outlets could potentially be configured, only one inlet and one outlet each were considered as is usually the case for disinfection contact tanks. More specifically, one inlet was connected at the bottom of the tank and one outlet used at the top of the tank, at the end of the last channel, to allow effluent to exit.

(a)

(b)

Figure 4.1: (a) Archetypal Disinfection Tank at CSU's ERC (b) Close-up of Inlets and Outlets

Figure 4.2 depicts plan-view geometry of the baffled contact tank. Thanks to previous research efforts by Kattnig (2014), two baffles were constructed out of plywood which use 2X4 pieces of wood to anchor them to the concrete bottom and sides of the tank. The baffles run along the longitudinal direction of the prototype and separate it into 3 distinct channels, each 15.5 inches (39.4 cm) wide and 132 inches (3.35 m) long. The turning points from one channel to the next are also 15.5 inches in order to avoid excess flow separation arising from contractions or expansions as the flow transitions from one channel to the next.

(a)

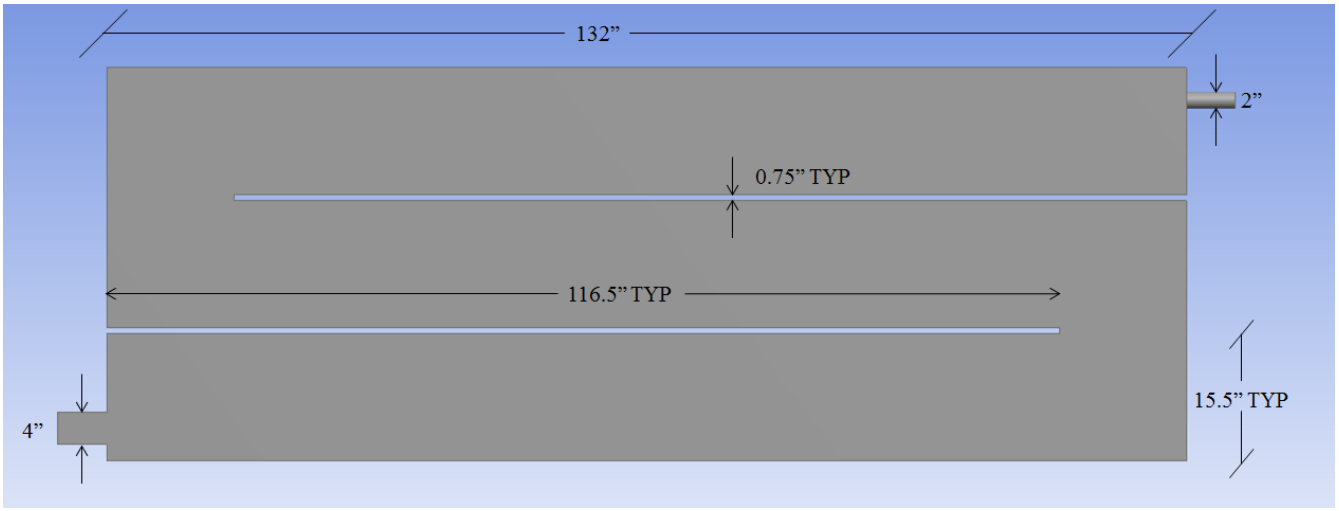

(b)

Figure 4.2: (a) Top of Contact Tank (b) Plan View of Contact Tank with Dimensions

4.3. Description and Motivation behind Inlet Modifications

As alluded to previously, the purpose of this research is to ascertain easily implementable methods to increase the contact time between drinking water and a disinfectant being used. Sharp inlets are often used to introduce the water and disinfectant into the system. In this scenario large

dead zones are a potential pitfall as the jet entering from the inlet passes over large volumes of the tank. It is hypothesized that modifying a sharp inlet by merely changing its orientation and/or number of orifices can significantly increase the efficiency of the system by better taking advantage of the ability of turbulence to enhance mixing. It is crucial that such alterations be simple so that small communities can successfully utilize them without incurring appreciable additional expenses that would offset gains in hydraulic efficiency.

Four different inlet attachments were utilized in an attempt to exploit turbulence found in the vicinity of a sharp inlet. As Figure 4.3 illustrates, an elbow (a), a tee (b), a U-shaped piece (c), and a three-way piece (d) were tested for potential improvements to the unmodified, straight scenario. The elbow in Figure 4.3(a) was oriented upward, downward, left and right in four separate tests, leading to a total of seven inlet configurations. A few of these were selected to be tested for flow rate dependence if promising results at 40 gpm warranted it. These attachments are made of PVC, are easily found at hardware stores, and cost no more than $3 each, satisfying the goal of economic modifications to the system.

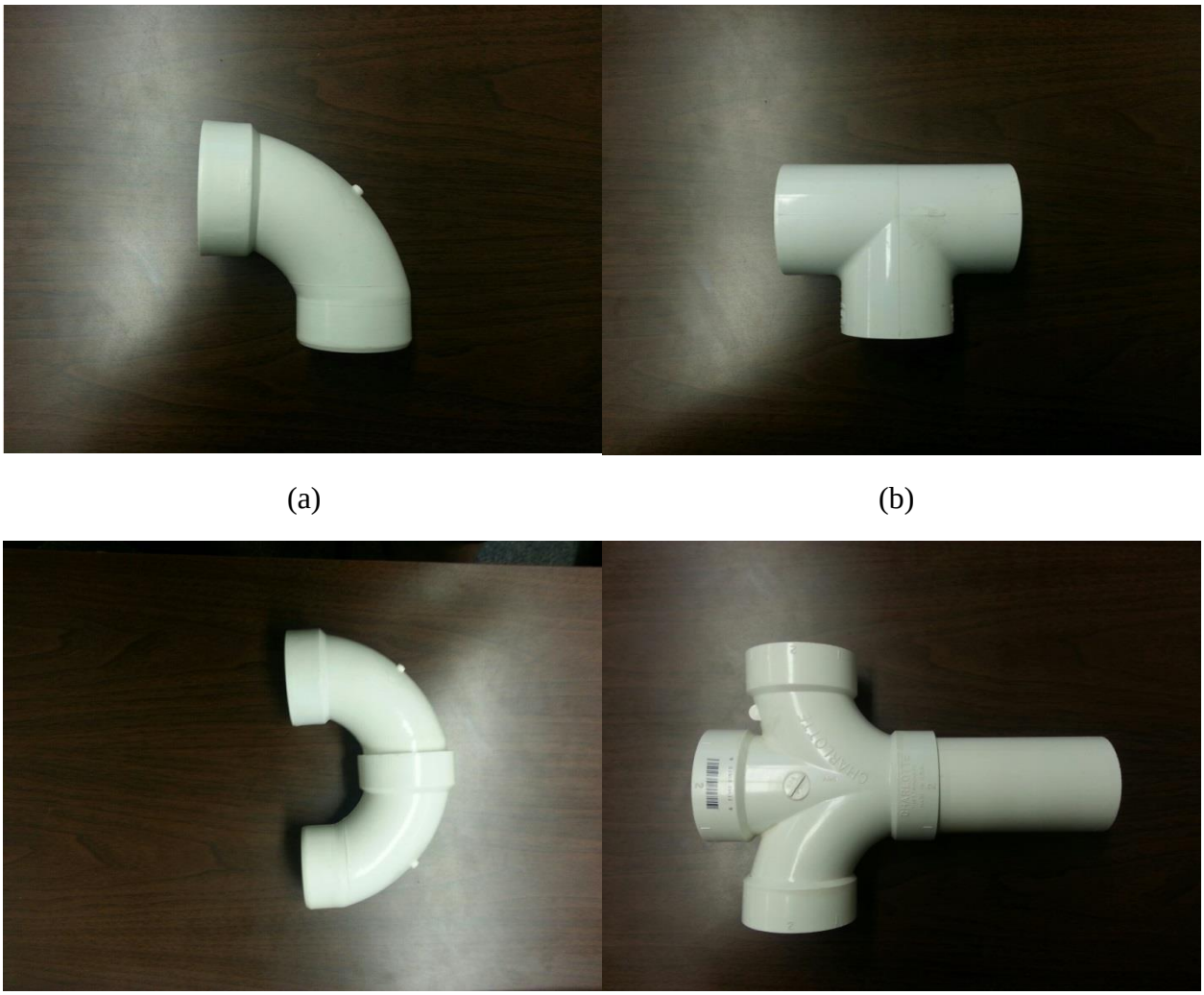

(a) (b)

(c) (d)

Figure 4.3: Various Inlet Attachments to Modify the Sharp Inlet: (a) Elbow (Left, Right, Down, Up) (b) Tee-shaped Piece (c) U-Shaped Piece (d) Three-Way Piece

4.4. Physical Tracer Studies

Physical tracer studies were run using the prototypical contact tank described in Section 4.2 for each of the inlet attachments shown in Figure 4.3. A flow rate of 40 gpm was used for each inlet modification as well as 10 and 20 gpm for the scenarios where the tee, the left-pointed elbow, and upward-pointed elbow were used. Every flow scenario was tested at least twice to ensure precision of the results.

4.4.1 Sodium Chloride, Electrical Conductivity, and RTD Curves

Step-input tracer studies were conducted on the physical prototype introduced in Section 4.2 by continuous injection of a solution of sodium chloride into the influent in order to obtain RTD curves for each inlet configuration. Sodium chloride was selected primarily for its ease of use and dependability. Its cost effectiveness also allows a large number of tests to be run economically. The sodium chloride dissociates into its respective ions in the source water, thereby increasing the water's electrical conductivity, which is then recorded as a function of time at the outlet with an electrical conductivity meter. This conductivity was then subtracted from the source water's background conductivity and was used in place of an actual concentration.

4.4.2 Upstream Conditions

Salt being introduced into the contact tank was assumed to be homogenously concentrated at the inlet. To achieve this, a chemical feed pump injected a saline solution upstream of the inlet which is depicted in Figure 4.4(a). The source water and saline solution then passed through a static mixer as seen in Figure 4.4(b). This static mixer forces highly rotational action of the mixture along its longitudinal axis before allowing the combined water and salt to pass through the inlet of the disinfection system.

(a)

(b)

Figure 4.4: (a) Chemical Feed Pump and Injection Setup (b) Static Mixer Upstream of Inlet

4.4.3 Buoyancy

Sodium chloride is known to increase water's density by an appreciable amount; seawater, for example, is typically about 3% denser than freshwater (Wilcox, 2012). Since the inlet is located at the bottom of the prototype, excessive concentrations of salt would create a stable stratification of fluid density. Such a scenario would result in a non-conservative estimation of the system's RTD curve; it would appear that superior mixing is occurring in the tank, but in reality the heavier, salt-containing water would remain towards the bottom for too

long and allow buoyant strata of water to exit the tank without any disinfection. With this in mind, Kattnig (2014) determined appropriate levels of saline concentrations to be injected upstream of the inlet in order to avoid unwanted buoyancy effects while still providing a large enough range of electrical conductivity variation to produce reliable and accurate RTD curves. These concentrations were used for the study at hand without additional complications.

4.5 Computer Modeling and CFD Software

CFD simulations are invaluable when attempting to explain the results of the tracer studies; the physical data only provides details about what is occurring at the outlet of the system but cannot why. CFD allows the researcher to investigate the three-dimensional velocity field, progression of scalar transport, and more in order to elucidate the hydrodynamics taking place in the contact tank.

Several commercial software packages exist for CFD modeling. FLUENT software by ANSYS was chosen for its use of the finite volume method, ability to handle user-defined functions, wide variety of model options and solver settings, support of large meshes, and widespread use and acceptance of its capabilities.

For each simulation, the flow field was initially solved in a steady-state formulation. Unsteady terms in the governing equations were then calculated based on the steady-state results and velocities were allowed to further stabilize. Kattnig (2014) showed that average velocities in the contact tank stop changing after roughly 1 TDT; the CFD simulations outlined in this chapter follow this metric for flow field convergence. Once this was accomplished, a non-dimensional scalar value of 1 was introduced at the inlet. To obtain the RTD curve, a monitor recorded scalar

concentrations at the outlet for each time step, using an area-weighted average to represent the concentration across the cross section of the outlet.

4.5.1 Turbulence Modeling and Associated Challenges

Reynolds averaging of the governing equations of flow was used to filter the flow field in time and provide practicable means of dealing with the wide range of time and length scales typically found in turbulent flow. This of course necessitates a turbulence closure scheme. Ultimately the RNG k-ε model was used for most simulations as it handles free shear turbulence well while still being computationally inexpensive. The application of the RNG k-ε model in disinfection contact tanks to correctly describe scalar transport has been validated by Wilson, Taylor, Barnett, and Kattnig (2011, 2012, 2013, and 2014, respectively). Similarly favorable results were obtained using were obtained using the standard k-ε model for the same purpose by Wilson & Venayagamoorthy (2010) and Gualtieri (2006). Enhanced Wall Treatment methodology was utilized due to its ability to often provide similar accuracy to the standard two-layer approach for wall treatment while not requiring excessively fine meshing near the wall (ANSYS, 2011). Three specific inlet configurations are presented and analyzed in detail in Section 4.7: The base case of a sharp, straight inlet, an elbow oriented upwards, and the horizontal tee.

Selecting the correct turbulence model to provide closure proved to be troublesome for many of the inlet modifications; the physics at hand in the vicinity of the inlet for these particular modifications is that of a jet impinging directly onto a wall, where very steep pressure and velocity gradients are found. Research efforts have concluded that second-moment closure schemes typically perform best when dealing with an impinging jet (Craft et. al, 1992), which prevents the need to assume the isotropic turbulent viscosity hypothesis. In FLUENT, the

Reynolds stress model is the only 2nd-order moment scheme available, which solves transport equations for the Reynolds stresses in conjunction with an equation for the dissipation rate (FLUENT, 2011). This selection proved to be adequate in resolving the flow where other turbulence models failed (as defined by a root-mean-square error between physical and numerical results larger than 5%), provided that it was used in combination with the PISO (pressure-implicit with splitting of operators) pressure-velocity coupling scheme and PRESTO! interpolation method rather than the solver settings described below. Due to the extra computational expense required, this choice of turbulence modeling and associated modified settings were only used for the T-shaped inlet in order to capture the physics of the impinging jet in the locale of the inlet sufficiently well.

4.5.2 Solver Settings

It was found that first-order upwind schemes were sufficiently accurate for spatial terms in the momentum, TKE, and dissipation rate equations as well as the Reynolds stresses when the RSM was utilized. The pressure-based segregated solver with the SIMPLE (semi-implicit method for pressure-linked equations) algorithm was utilized to couple pressure and velocity except for when the RSM was used, which required the PISO pressure-velocity scheme to perform well. Gradients were computed using the least squares cell-based method and pressure was interpolated at the cell faces by a standard scheme wherein momentum equation coefficients are used. Again, the RSM required different settings than those of the RNG k-ε model. Here a PRESTO! (Pressure Staggering Option) was needed rather standard interpolation choices. Transient terms were discretized with an implicit second-order scheme to ensure stability and to provide a good balance between accuracy and computational effort. A third-order upwind scheme called MUSCL was used for the scalar transport equation as Wang and Falconer (1998)

suggest that the advection term is approximated better with third-order upwind differencing methods, although others have successfully used first-order upwind schemes (see Kattnig, 2014).

4.5.3 Boundary Conditions

Boundary conditions were specified at the inlet orifices, outlet, walls, and free surface:

Inlet – A cross-sectional averaged velocity normal to the inlet orifice(s) was specified inlet corresponding to the flow rate at hand. Turbulence parameters such as turbulent intensity and hydraulic diameter were also required. Because the inlet is circular with fluid completely filling its area, the hydraulic diameter was simply the diameter of the pipe (2 inches, or 5.08 cm). Turbulent intensity, defined as the ratio between the root-mean square of velocity fluctuations and average velocity in a particular direction, was estimated by the following equation:

$$I = 0.16(Re_{D_H})^{-1/8}, \tag{24}$$

where I is the turbulent intensity and Re_{D_H} is the Reynolds number calculated using the hydraulic diameter as the length scale (ANSYS, 2011). This empirical relationship assumes fully-developed pipe flow, which was not the case due to abrupt changes in flow direction just before the water enters the contact tank. Fortunately, solutions to the flow field proved to be insensitive enough to turbulent parameter estimations that a crude guess was sufficient in this case. Finally, a non-dimensional user-defined passive scalar value of 1 was introduced at the inlet once the velocity field was sufficiently resolved as described earlier in this section.

Outlet – A gage pressure of 0 Pa was given as the key boundary condition at the outlet. This was deemed appropriate because the fluid exiting the tank was anywhere between 0 and 3.6 inches away from the free surface, meaning any variations from zero gage pressure arising from hydrostatic variations were negligible.

Walls – Walls were set to be stationary with the standard no-slip condition.

Free Surface – In order to reduce computational effort, the rigid lid approximation was used to specify conditions at the free surface since it does not distort appreciably. In FLUENT, this can be achieved by using the "symmetry" boundary, which implies that normal velocities and gradients are zero immediately adjacent to the surface (FLUENT, 2011).

4.5.4 Scalar Transport Modeling and User-Defined Functions

The scalar being modeled in this case is passive, meaning it is affected by the flow field but does not affect it in return. As in Chapter 3, the following equation describes the mean concentration of the passive scalar as a function of both space and time (Pope, 2000):

$$\frac{\partial C}{\partial t} + \bar{U}_j \frac{\partial C}{\partial x_j} = \frac{\partial}{\partial x_i}\left(\kappa_{eff} \frac{\partial C}{\partial x_i}\right) \tag{25}$$

where C is the average concentration of the scalar and κ_{eff} is the effective diffusivity. Equation 25 uses the gradient-diffusion hypothesis, which assumes that turbulent scalar transport occurs down the gradient of the mean scalar field (Pope, 2000). The effective diffusivity is then considered to be the sum of the molecular and eddy diffusivities:

$$\kappa_{eff} = \kappa + \frac{\nu_t}{Sc_t} \tag{26}$$

where κ is the molecular diffusivity of the scalar and Sc_t is the turbulent Schmidt number. Although much discussion still exists in literature regarding its correct value, Venayagamoorthy & Stretch (2010) showed that 0.7 is a reasonable value for Sc_t in neutrally-stratified flows, so it was used for the CFD models presented here. This approximation was given as an input to FLUENT by means of a simple user-defined function, or UDF (see Appendix A for the specified UDF).

4.5.5 Grid Independence and Meshing Quality

Geometry and subsequent meshing was carried out using Workbench software by ANSYS. Cutcell meshing was specified globally. While this leads to an unstructured mesh, it produces desirable statistics of the cells in the mesh such as high orthogonal qualities, low aspect ratios and skewness, and good orientation of cells relative to the flow direction for the majority of the flow domain. Size functions were used to automatically refine the mesh in the vicinity of walls or curved geometry where larger gradients are typically expected to occur. Inflation was initially placed at boundaries near the outlet but was found to have little effect on the results, so it was discarded in most of the subsequent simulations to save on computational cost and maintain a high orthogonal quality of the mesh. Refined cell sizing was specified near the inlet, about 30 inches down the first channel, at which point much smaller velocities are expected in the tank and hence courser cell volumes are assumed to be adequate. Meshing resulting from these specifications for an arbitrary simulation is shown in Figure 4.5.

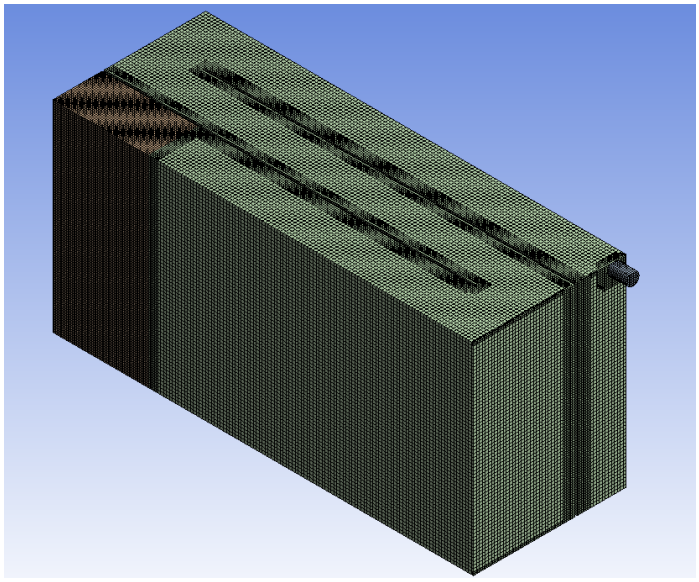

Figure 4.5: Meshing for an Arbitrary Simulation

For the contact tank being modeled Kattnig (2014) showed grid independence of baffling factors is achieved at about 1,000,000 cells. As a conservative measure each mesh used had about 1.4 million cells and contained no less than 1.3 million cells. Section 4.7.1 shows validation data which shows this size of mesh to be justified.

4.5.6 Time Step Selection and Independence

Kattnig (2014) also showed time step independence is achieved at no less than $\Delta t = 2s$ for the disinfection system at hand. Due to several of the inlet modifications leading to impinging jets, which has local physics that tend be more difficult to resolve in a RANS framework than Kattnig's simulations, $\Delta t = 1s$ was used instead to ensure that time step selection had no effect on the results. Again, this choice is justified by the validation data.

4.6 Results and Discussion

4.6.1 RTD Curves and Baffling Factors

Figure 4.6 summarizes the RTD curves and associated baffling factors resulting from physical tracer studies run at 40 gpm. The base case, in which a sharp inlet introduces source water parallel to the first channel at the bottom of the tank with a 2-inch diameter pipe, has an unimpressive baffle factor of 0.34. This is still superior to the un-baffled scenario where the system creates very large dead zones and attains a *BF* of only about 0.05 (Kattnig, 2014). Only one modification performed worse than the straight inlet, which is the 3-way (straight, to the left, and to the right) attachment. Due to the geometry, the flow rates at each orifice are not equal and only a small portion of the original jet's momentum is deflected perpendicularly. The left and right orifices have low velocities about an order of magnitude lower than the straight orifice, causing relatively stronger short-circuiting as induced by the primary jet.

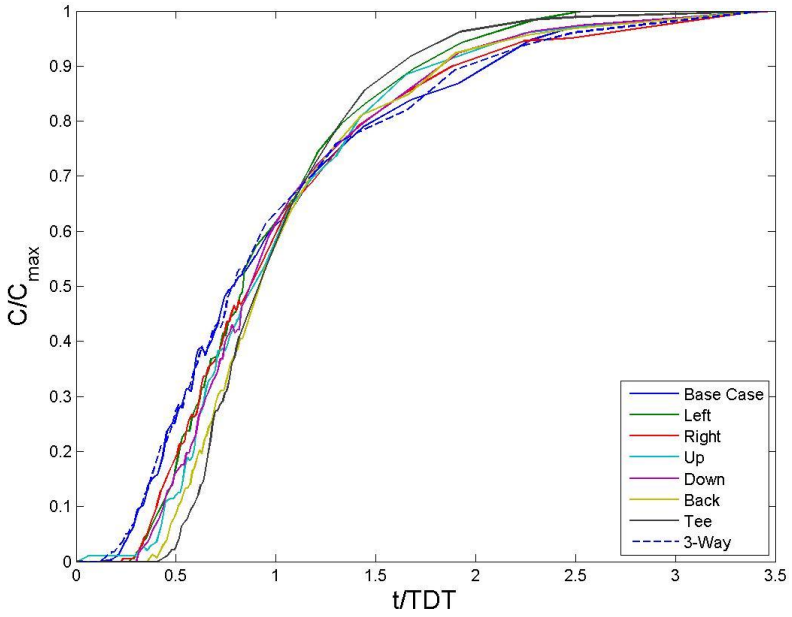

(a)

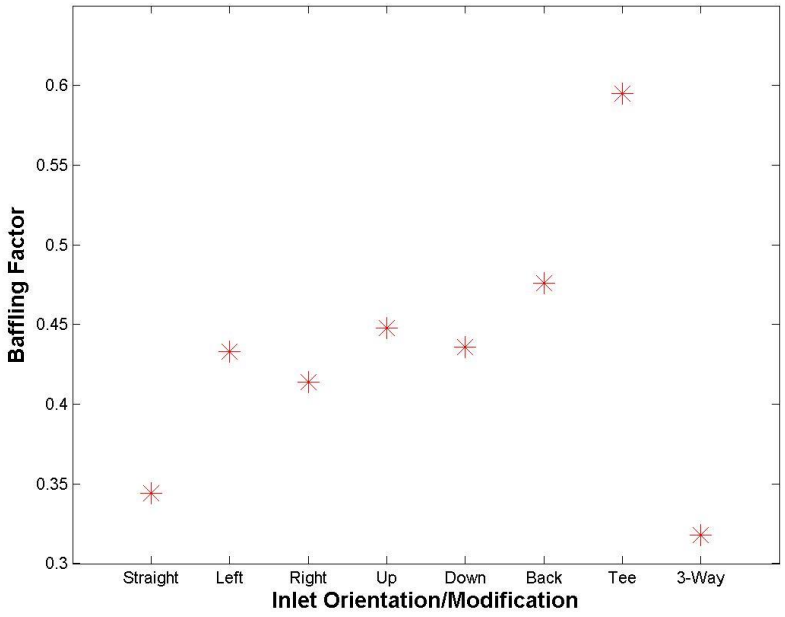

(b)

Figure 4.6: (a) RTDs for all Inlet Modifications at 40 gpm (b) BFs for all Inlet Modifications

The majority of the inlet modifications performed fairly similarly: the four elbows which were oriented left, right, down and up in addition to the short U-turned pipe used to shoot the jet to the back of the first channel. These five inlet conditions averaged a BF of about 0.44, a significant improvement over the straight jet of nearly 30%. It was hypothesized that deflecting the sharp inlet away from the direction parallel to the channel would help create a more homogenous velocity field in an attempt to mimic an ideal inlet condition (where the cross-sectional geometry identical to the cross-section of the channel itself). This is explained and justified in Section 4.7 below, where a hydrodynamic analysis is presented.

Finally, Figure 4.6(b) shows that the teed inlet condition (to the left and right) achieved the best RTD curve by far. From two physical tracer studies the average baffling factor was 0.59, an impressive 74% gain from the unmodified inlet. It was already anticipated that better mixing efficiency would occur in the case of a larger net cross-sectional inlet area (two orifices of 2-inch diameters rather than just one), but the teed inlet exceeded these expectations nonetheless.

4.6.2 Flow Rate Dependence

The results presented above were from flow rates of 40 gallons per minute. Mixing for lower flow rates of 10 and 20 gpm was also assessed for some inlet modifications in order to explore the dependence of RTD curves on Q. More specifically, the upward elbow, tee, and straight inlets were tested at the above flow rates. Right, down, left, and backwards orientations were assumed to possess similar dependence on flow rate as the elbow pointed up due to their similar RTD curves at 40 gpm. Transitional Reynolds numbers occur at 10 gpm for the 2-inch diameter inlet at hand; therefore, it was deemed unnecessary to investigate flow rates lower than this, as the flow regime would become laminar and produce a predictably inferior mixing

environment. The three-way inlet also not of concern because results from the 40 gpm tests have already shown that it is not a favorable inlet modification.

Figure 4.7 depicts the effect of system flow rate on *BF* values across different inlet modifications. The hydraulic efficiency of the unmodified, straight inlet is slightly influenced by flow rate but is overall rather insensitive to it. Mixing conditions enhance with flow rate but then quickly plateau for the left-oriented elbow. Due to its superior performance at 40 gpm and its large dependence on flow rate the teed inlet was further investigated numerically at 30 and 50 gpm. It was determined that at 30 gpm its baffling factor more or less plateaus. Although this modification experiences a rapid decline in efficiency with decreased flow rate, it still performs about as well as elbow to the left and the base case at 10 gpm.

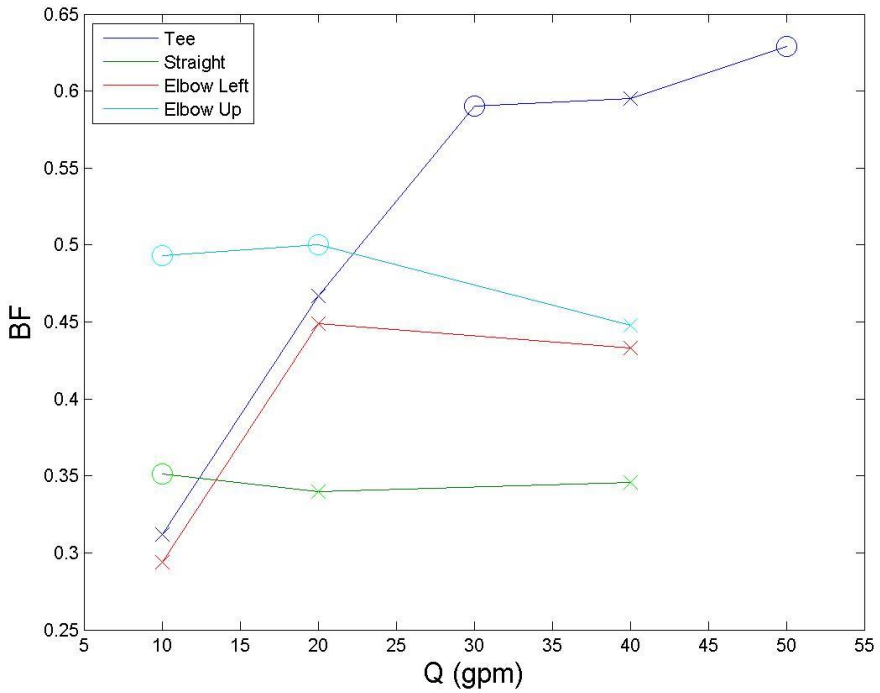

Figure 4.7: Flow Rate Dependence of Baffling Factors for Selected Inlet Conditions (x-Markers are Physical Tests while o-Markers are CFD Simulations)

Surprisingly and perhaps counter-intuitively, an upward-pointed elbow appears to increase modestly in efficiency as flow rate decreases (but as a whole behaves similarly across all flow rates). It is therefore clearly the superior choice when dealing with low flow situations that produce poor mixing conditions, especially considering the drastic decrease in baffling factors experienced by other inlet modifications at smaller flow rates.

Although the baffling factor is the most important system parameter from a practical point of view, it is helpful to investigate other measures of performance, if only briefly. Namely t_{10}/t_{90} and the Morrill index are presented for each inlet modification and flow rate tested as summarized in Table 4.1. t_{10}/t_{90} can provide valuable insight because it a ratio of two values on the RTD curve that are directly influenced by geometry and the flow dynamics in general. On the other hand, *BF* depends on the system's *TDT*, which in turn only considers the tank's volume and its flow rate. This can lead to overestimation of a tank's disinfection efficiency as argued by Wilson (2011). The Morrill index is simply the reciprocal of t_{10}/t_{90} and is a measure of dispersion in the tank.

From Table 4.1 it is readily seen that a strong correlation exists between *BF* and t_{10}/t_{90} and therefore a strong inverse correlation exists between *BF* and *MI*. In most instances t_{10}/t_{90} is about half of its corresponding baffling factor, meaning it takes roughly 2 *TDT*s for 90% of the original concentration at the inlet to reach the outlet. A notable exception to this is the teed inlet at all flow rates, which only needs about 1.5 *TDT*s for 90% to reach the outlet. This is also manifested in its lower *MI*. In fact, the only test to attain an *MI* below 3 is the teed configuration at 40 gpm. As a whole it can be concluded that the teed inlet performs the best not only in terms of baffling factors but in terms of t_{10}/t_{90} and *MI*. On the other hand the 3-way inlet performs the

worst across all measures of performance, having one of the lowest *BF*s and the highest *MI* for 40 gpm.

Table 4.1: Summary of Results

2-Baffle System				
Inlet Modification	**Flow Rate (gpm)**	**BF**	**t_{10}/t_{90}**	**MI**
None (Straight)	40	0.34	0.16	6.31
	20	0.30	0.14	6.98
	10*	0.35	0.19	5.32
Elbow Left	40	0.43	0.24	4.09
	20	0.45	0.27	3.66
	10	0.29	0.17	6.06
Elbow Right	40	0.42	0.22	4.59
Elbow Up	40	0.45	0.25	3.99
	20*	0.50	0.25	3.96
	10*	0.49	0.31	3.26
Elbow Down	40	0.44	0.24	4.20
U-shaped (Back)	40	0.48	0.26	3.91
Tee (Left & Right)	40	0.60	0.41	2.46
	20	0.47	0.30	3.31
	10	0.31	0.19	5.27
3-Way (Left, Straight, Right)	40	0.32	0.16	6.42

*From CFD simulations

4.7 Hydrodynamic Analysis

This section takes advantage of the capabilities of CFD to estimate arbitrary flow fields in an attempt to explain the hydrodynamics taking place across various inlet modifications for the internally-baffled contact tank. More specifically, the teed and elbow up inlet modifications (for which acceptable model validation has been established and which are assumed to be representative of other inlet attachments) are contrasted to the straight, unmodified inlet to provide reasoning behind the enhanced mixing efficiency that has been observed to occur. All scenarios occur at a flow rate of 40 gpm unless stated otherwise. The 3-way inlet is again omitted from discussion because of its poor performance in physical testing.

4.7.1 Model Validation

As useful as numerical modeling may be, caution must be taken when interpreting results. Issues such as mesh size and quality, time step size, artificial physics arising from discretization of derivatives in governing equations of flow, boundary condition estimation, turbulence modeling, and more can cause erroneous results. These results are even more dangerous when they appear to be plausible but are actually inaccurate, as can happen all too often. Physical validation is therefore essential if one is not extremely confident in his or her simulation. Because of this, RTD curves arising from numerical models were compared to physical tracer studies in order to validate them before accepting the model's results as accurate. These can be seen in Figures 4.8(a), (b), and (c). In each of the three cases the physical data is represented by discrete points designated by x-markers. RTD curves from numerical simulations are also discrete but are so numerous and closely spaced that they appear to be a continuous line.

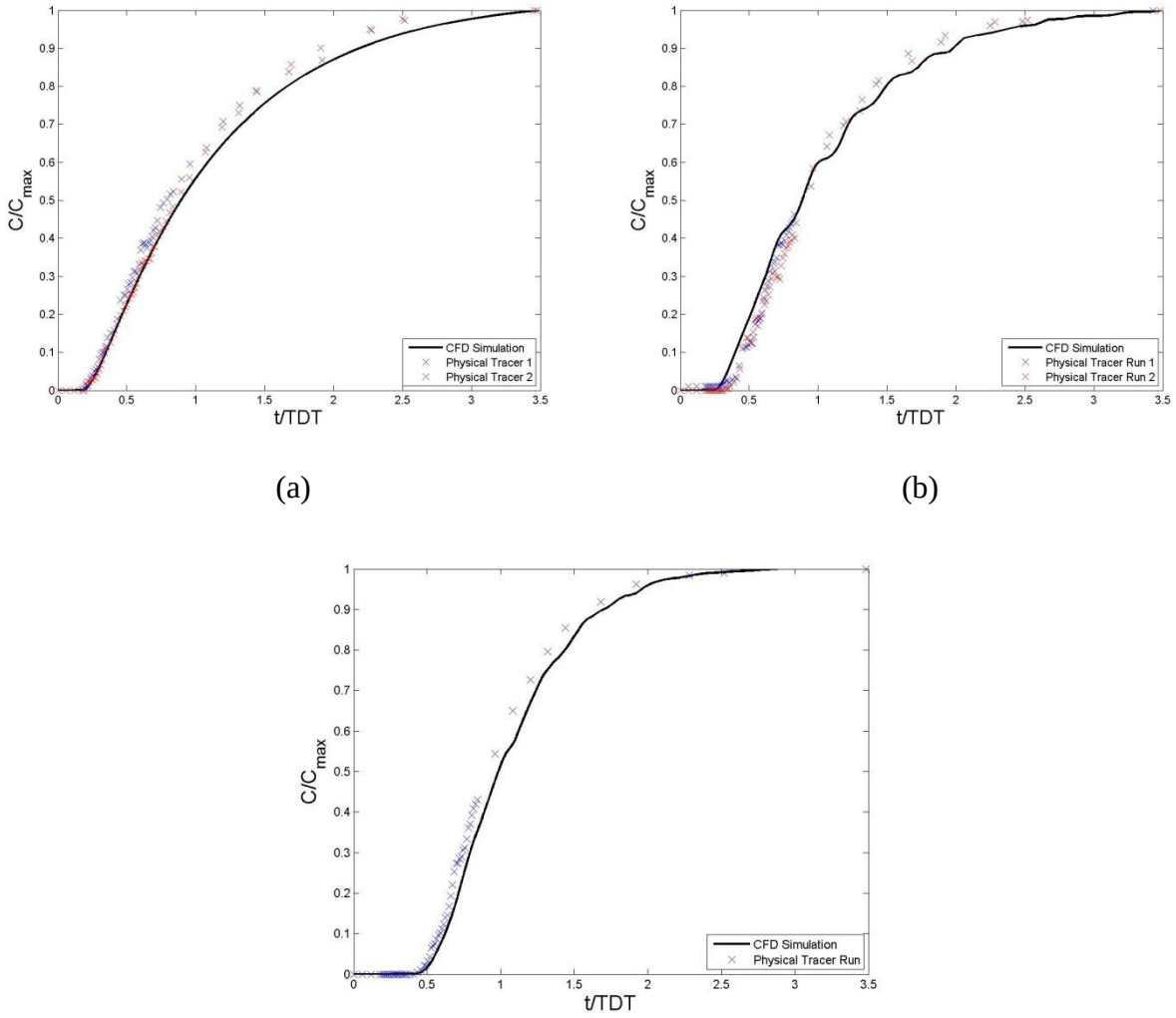

Figure 4.8: Physical Validation of Three Inlet Configurations: (a) Straight (b) Upward-Oriented (c) Teed

Graphically all three simulations seem to fit well with the physical tracer studies. Even so, a quantitative evaluation is desirable in order to help eliminate the ambiguity involved in a visual determination of accuracy. To this end a root-mean-square error between each of the physical tests and their corresponding numerical simulations were evaluated for all three validation plots. It should be noted that only flow times for which a data point for both the physical and numerical tests existed could be evaluated. These calculations are summarized in Table 4.2, which suggest highly favorable results. An average error of just 4.6% is observed

between a physical tracer and CFD for both the upward elbow and teed configurations with even smaller error for all other validations. It is therefore concluded that all three CFD models describe the flow dynamics in the tank with negligible error.

Table 4.2: Root-Mean-Square Error between Physical and Numerical Data

Root-Mean-Square Error, 40 gpm		
Inlet Modification	**Physical Tracer 1**	**Physical Tracer 2**
None (Straight)	0.039	0.018
Elbow Up	0.037	0.046
Tee	0.046	N/A

4.7.2 Flow in the Vicinity of the Inlet and in the First Channel

Figure 4.9 illustrates the vastly different conditions occurring in the cross-sectional plane at the inlet for each modification by means of contours of velocity magnitude normalized by volume-averaged tank velocity. It can be readily inferred that the flow dynamics in this vicinity are highly dependent on boundary conditions stemming from the different inlet conditions. Figure 4.9(a) (the original inlet) implies a large dead zone above the inlet, where water is stagnated and stays largely untreated. The free jet shoots past a substantial portion of the first third of the tank and loses out on favorable channeling effects. On the other hand, Figures 4.9(b) and (c) show the teed and upward elbow modifications to the inlet, which make much better use of the region above the entrance to the tank. In both cases the influent is deflected away from the longitudinal direction of the channel and fills up the large dead zone in the first channel. This allows the flow to stabilize to a more two-dimensional flow much faster, resulting in better approximation the idealized inlet (that again, is the same as the cross-section of the channel itself).

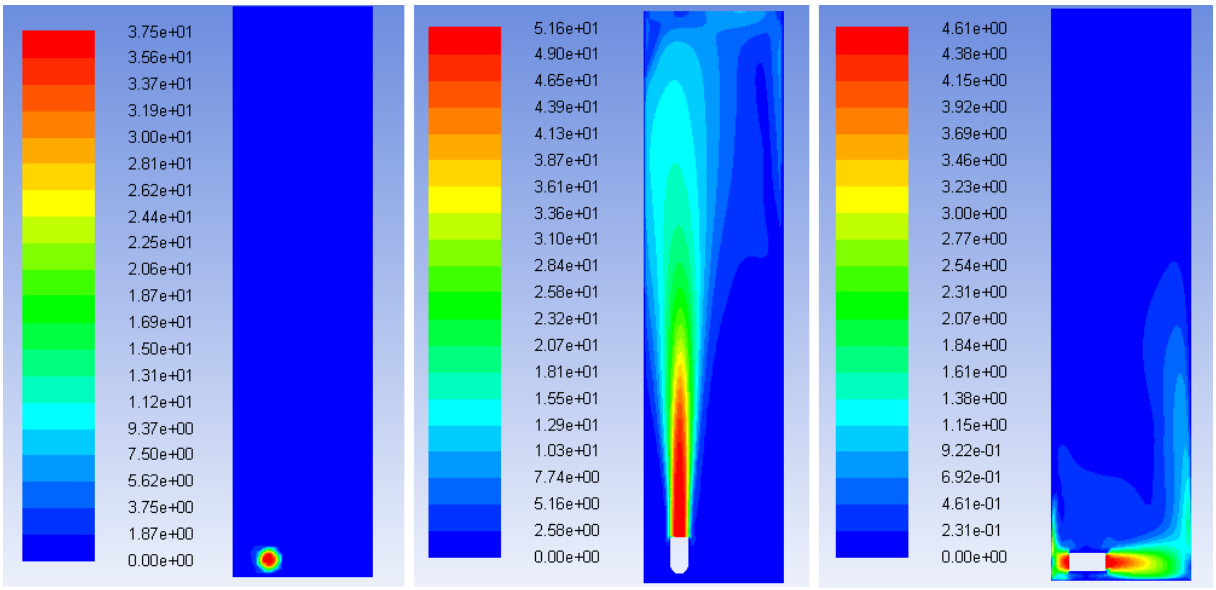

(a) (b) (c)

Figure 4.9: Contours of $|V|/|V_{avg}|$ in Horizontal Plane at the Inlet for Different Modifications: (a) Unmodified (b) Elbow Up (c) Tee

Figure 4.10 shows the resulting vertical (y) velocities from the various inlet modifications in a horizontal plane that dissects the first channel at the center of the inlet, normalized by average y-components of velocity in the tank. The goal is to swiftly bring dv/dx and thereby v-values themselves to a minimum, where x is the stream-wise (longitudinal) direction of the channel. This is thought to maximize horizontal advection while simultaneously minimizing diffusion as in the case of a non-sharp, ideal inlet. Clearly and as expected, the straight inlet performs the worst. Several contour lines are encountered throughout the span of the channel, producing sharper gradients in vertical velocities with respect to the longitudinal direction when compared to modified scenarios. So much of the jet's power remains at the end of the first channel that a rapid change from dynamic to static pressure can be inferred as it hits the wall and its remaining momentum is deflected upward. From a scalar transport point of view, excessive levels of diffusive mixing are allowed to occur in the upper regions while vertical momentum slowly dissipates throughout the channel.

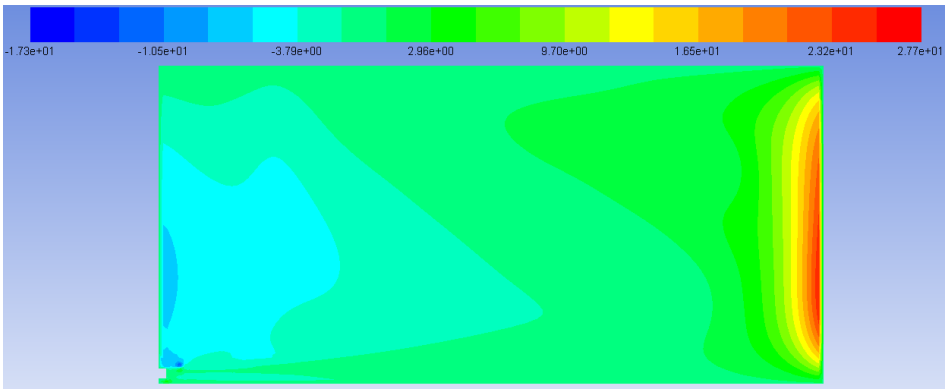

(a)

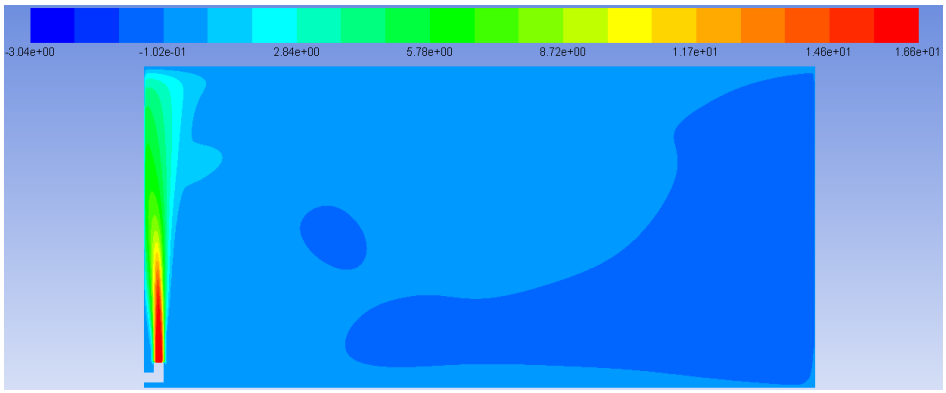

(b)

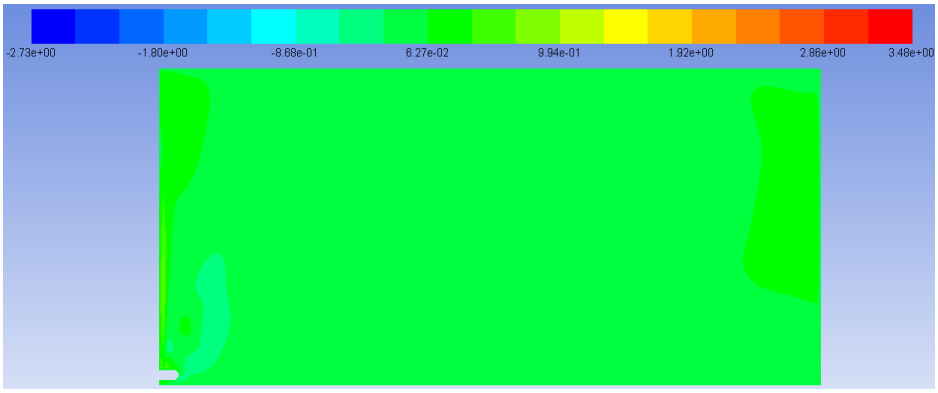

(c)

Figure 4.10: Contours of v/v_{avg} in Vertical Plane at the Inlet for Different Modifications: (a) Straight Inlet (No Modification) (b) Elbow Up (c) Horizontal Tee

The upward-pointed elbow improves upon vertical velocity gradients as depicted part (b) of Figure 4.10. Dissipative forces resulting from differences in velocities between the free jet and its comparatively inert surroundings allow upward motion to lessen substantially before the rest

of the first compartment is traversed. This allows the disinfectant to better fill the cross-section before the second and third portions of the tank are reached. Only one normalized contour value (-0.00627) is found in the majority of the channel after the inlet in contrast to the unmodified inlet where multiple contours are observed throughout the longitudinal direction.

Finally, the teed inlet in Figure 4.10(c) performs even better than the upward elbow Effects of a sharp inlet can scarcely be seen at all since the y-velocities are almost entirely between two contour values. The superior baffling factor attained for this inlet is largely accounted for by the near-zero vertical velocity field already found at the beginning of the first channel of the tank. A teed inlet also intuitively allows a scalar to fill the transverse direction of the cross-sectional plane. However, the height of the tank is over 7.5 times the width of each channel, so this is not thought to be as important as a low vertical velocity field although this explains the teed inlet's superior mixing performance at least in part.

4.7.3 Flow Behavior through the Entire Tank

While a large portion of the enhanced mixing efficiency is revealed in the flow dynamics found in the first portion of the baffled tank, it is still useful to investigate the second and third channels. Here, x is defined as the centerline ordinate throughout the tank. Cross-sectional area-weighted averages of both the velocity magnitudes and vertical velocities were calculated at 16 different points in the tank in order to filter out dependence on transverse and vertical directions and focus on changes throughout the primary direction of flow: the inlet, the two turning points between channels, the outlet, and four equally-spaced locations in each of the three channels. They were then normalized by the maximum velocity found in the tank (magnitude and vertical values corresponding to Figures 4.11(a) and (b), respectively) and linearly interpolated between data points. The x-axis is divided by the total length of the centerline ordinate (142 inches) and

finally the results are plotted in Figure 4.11. Channels 1 and 2 terminate at roughly $x/L_{total} = 0.33$ and 0.67 respectively.

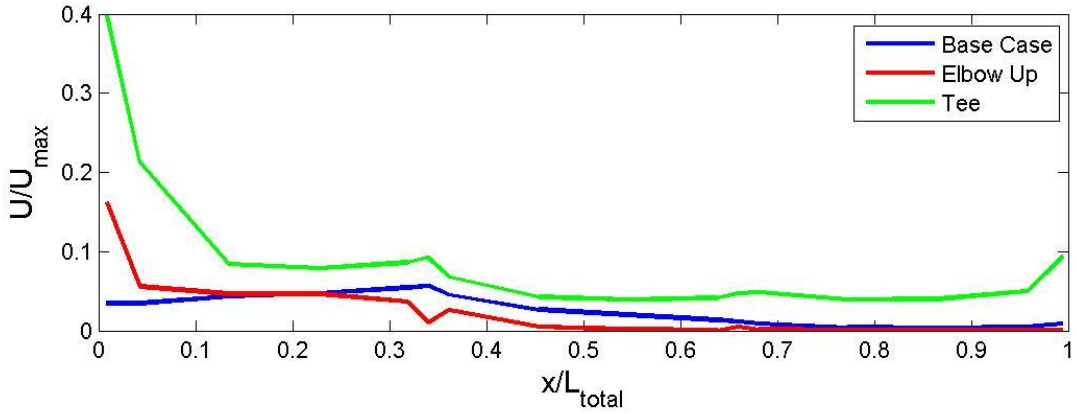

(a)

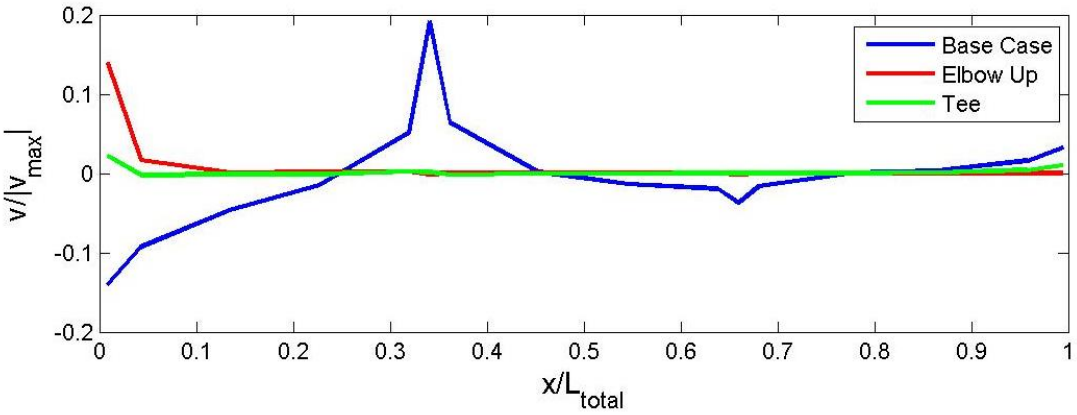

(b)

Figure 4.11: Area-Weighted Average Velocities throughout the Baffled Tank for (a) Velocity Magnitudes and (b) Vertical Velocities

Ultimately the data at the inlet was omitted since velocities are orders of magnitude higher than the rest of the tank, even when non-dimensionalizing them; to include them would hinder visual interpretation of the results by making the smaller scales difficult to see. The first plot is only marginally revealing since directional components of the velocity field are not

accounted for. The magnitude of the velocity field for the unmodified case does not vary significantly. Meanwhile, teed and elbow-up inlets experience quickly decaying velocities in the first channel as already discussed in Section 4.7.2, then stay mostly constant thereafter.

The second plot of Figure 4.11 is much more insightful. Both inlet modifications produce sharp decays in upward velocities down to almost zero which are achieved in less than 5% of the total length of flow. Only towards the do end they raise back up again slightly, in the last couple of feet, so that water located in lower regions of the tank may exit (recall that the outlet is located at the free surface). This is in agreement with the idea that bringing the flow to a two-dimensional state rapidly will allow better emulation of an ideal inlet.

In marked difference to these scenarios, the unmodified inlet has vertical velocities that fluctuate over the entire x ordinate and are rarely near zero on average. They surprisingly start more negative than positive, but then shoot upward as the end of the first channel is reached. This corresponds to the upward deflection of flow as the jet impinges on the back wall of the first channel and subsequently makes the turn into the second channel. A similar yet opposite and smaller effect occurs during the transition between the second and final channels as can be seen between 60% and 70% of the total flow length. Just as it appears the vertical velocities are finally stabilizing, they again increase in order to reach the outlet as in the cases of the teed and elbow-upward inlets. As a whole Figure 4.11 serves to strengthen the notion that gradients in vertical velocities with respect to longitudinal flow directions (as well as vertical velocities themselves) imply a lack of thorough mixing across a given cross-sectional plane. Consequently, slower-acting diffusion occurs rather than bulk scalar transport via horizontal advection.

4.7.4 Cross-Sectional Distribution of Flow

Now that longitudinal dependence of flow has been discussed, attention is turned to behavior with cross sections throughout the system. Obviously, vertical velocities and their gradients do not account for all of the observed gains in mixing efficiency; otherwise the teed and upward-oriented inlets would behave almost identically, as both the gradient of v in the longitudinal direction and v itself goes to zero within 10% of the total flow path in both cases. Ideally flow should be as homogenous as possible so that plug flow may be approached.

Figures 4.12 and 4.13 portray lateral and longitudinal velocities, respectively, in the same cross sections used in Figure 4.11 (except for the turning points between channels, which are orthogonal to the rest of the planes and would obstruct visibility). An isometric view is utilized in order to display a large number of planes in an efficient amount of space, with the inlet's plane located on the far left and the outlet's plane on the far right. The contours are normalized by 10% of the velocity at the inlet required for a flow rate of 40 gpm (about 1.25 m/s) in Figure 4.12 and by 50% of the same value for Figure 4.13. Any location that exceeds these thresholds will lack contours, but they are small, so using scales of $w/(0.1 \cdot V_{inlet})$ and $u/(0.5 \cdot V_{inlet})$ allows for a better visualization of the distribution across the planes by utilizing more contour values. Figures 4.12 and 4.13(a) depict the entire tank at the same angle as (b) through (d) as a reference to depict the location of each cross section.

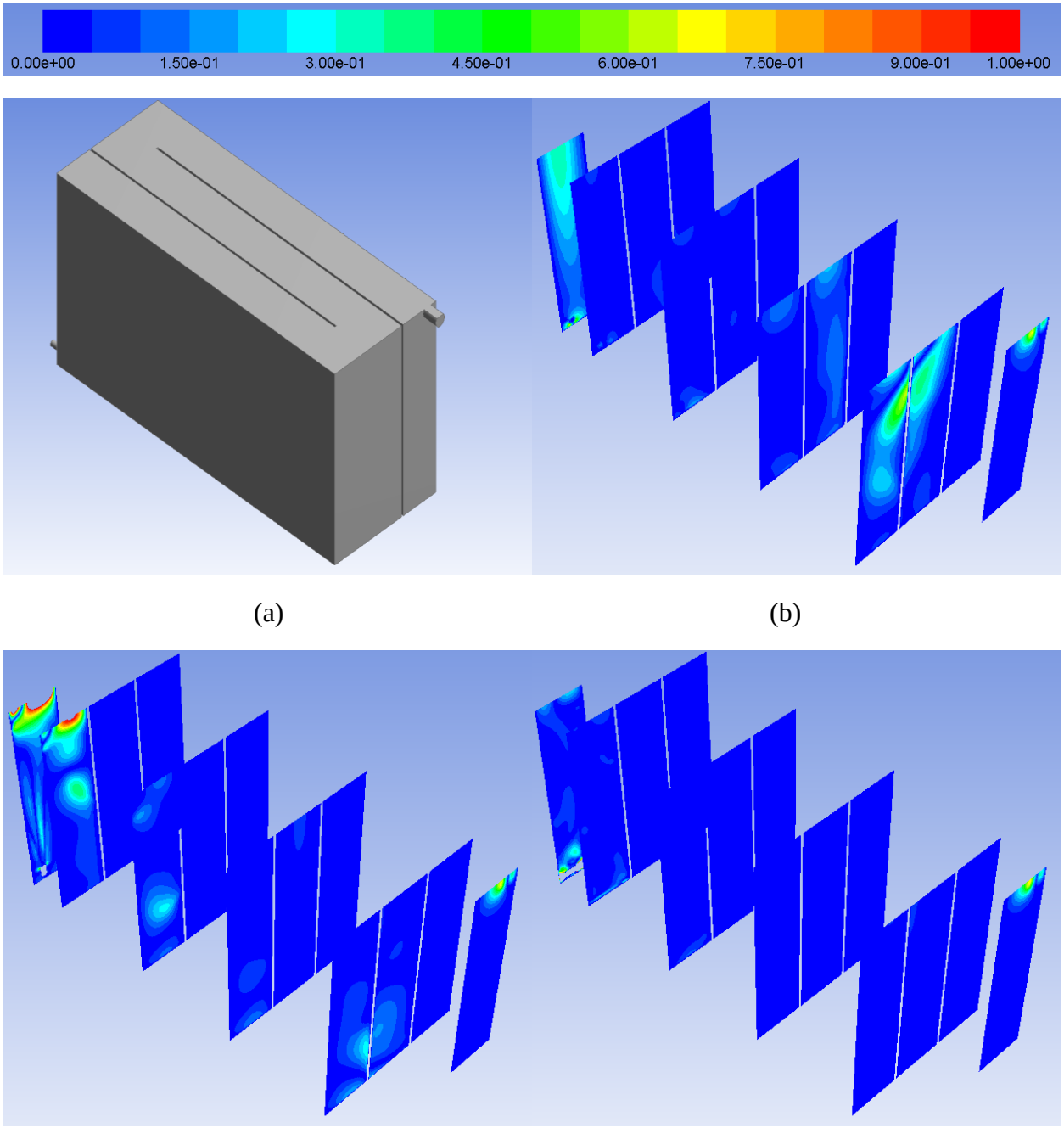

Figure 4.12: Distribution of Lateral Velocities [$w/(0.1 \cdot V_{inlet})$] across Various Cross Sections: (a) Isometric View of Entire Tank (b) Base Case (c) Elbow Up (d) Tee

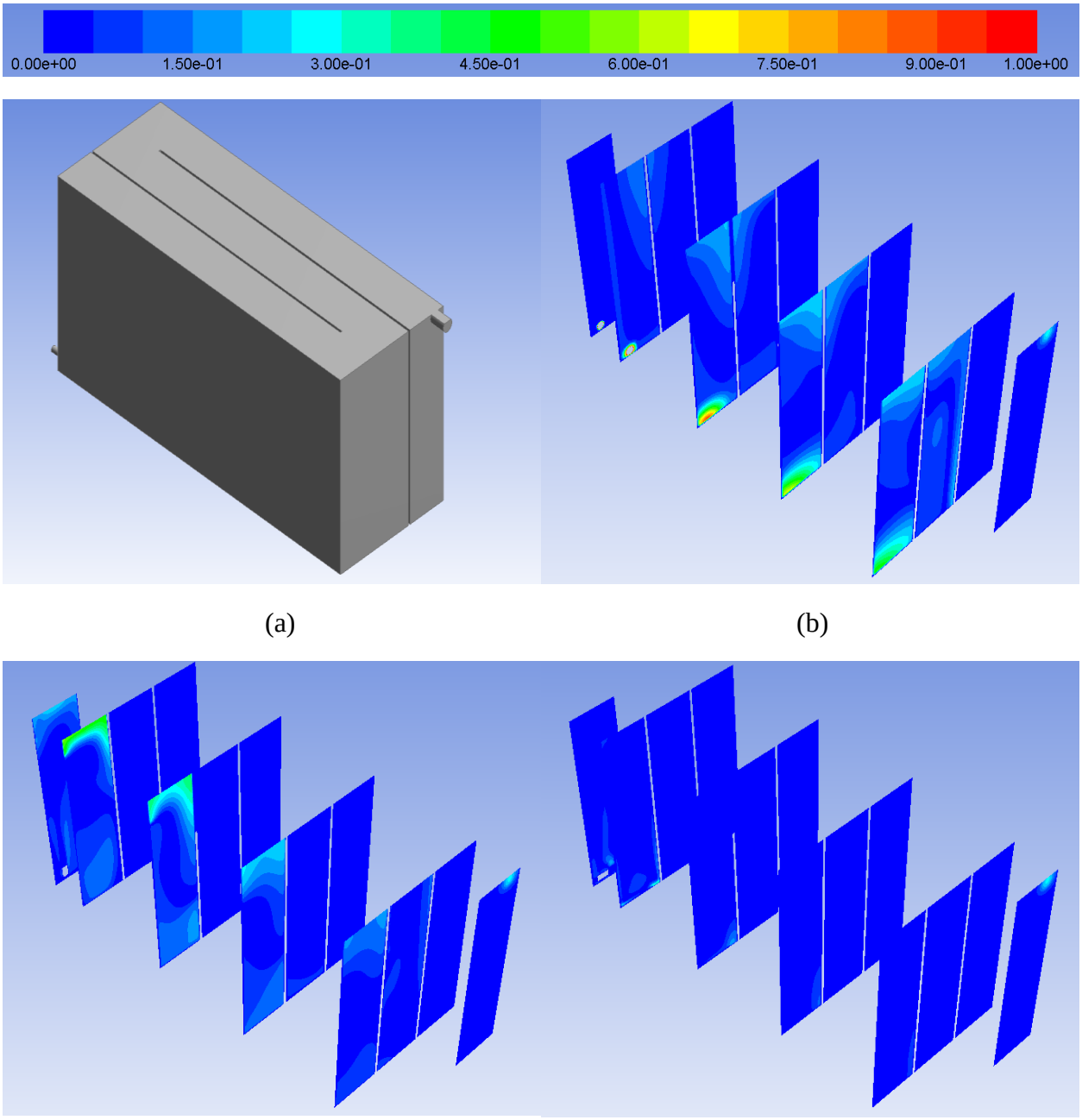

Figure 4.13: Distribution of Longitudinal Velocities [$u/(0.5V_{inlet})$] across Various Cross Sections: (a) Isometric View of Entire Tank (b) Base Case (c) Elbow Up (d) Tee

Unsurprisingly, the original and elbow-up inlets experience significant lateral movement throughout the first channel, especially in the upper portions. By the second channel this sideways flow has largely stopped for the elbow-up inlet but the straight inlet continues to mix

laterally throughout much of the second channel, which leads to a significant loss of scalar advection. As predicted, sideways movement in the tank with the teed inlet ceases very quickly in accordance with the notion that its lateral orientation efficiently spreads flow throughout the z (transverse) ordinate before any significant portion of the longitudinal direction is traversed. All three scenarios experience a small surge near the outlet to allow enough water to exit the outlet in order to maintain mass continuity.

Figure 4.13(b) clearly shows the jet from the straight inlet shooting across the bottom of the first channel. It is partially wall-bounded and hence the constant axisymmetric spreading rate of a fully-turbulent free jet is not observed. Instead, it spreads with a small lateral bias, but still rather poorly compared to the size of the entire cross-sectional area. Excessive gradients of longitudinal velocities in lateral and vertical directions are still observed until the third channel, where the flow becomes essentially one-dimensional (except near the outlet) and efficient mixing conditions are finally evident.

Figure 4.13(c) indicates improved conditions in the contact tank. The disinfection system with the upward elbow inlet experiences rather uneven longitudinal velocities at first, of course taking place primarily near the free surface. Despite this, the tank with the upward inlet experiences a stabilization of longitudinal velocities by the beginning of the second channel. This appears to be a key difference between the inlet pointed upward and the unmodified inlet, whose influences are clearly seen in the second channel. Such a difference may be surprising considering the similarities in their first channels: both contain longitudinal velocities that are found primarily in either the lower or upper portion of the cross-sections, potentially causing one to erroneously conclude that no changes in mixing efficiency would be noted between the two tanks when in fact significant changes are realized.

Finally, Figure 4.13(d) illustrates the improvements caused by the teed inlet over both other cases presented here. Within the first 10% of the tank very few contours are seen in a given cross-section. This is to be expected, as a uniform longitudinal velocity field serves to approximate plug flow. Nonetheless it is still important to prove that this is in fact the flow that is actually occurring in the tank.

4.7.5 Flow Rate Dependence of Contact Tank with Teed Inlet

Because it performed so well at higher flow rates and because its efficiency declined substantially with *Q*, the teed inlet merits further discussion. Figure 4.14 shows that its RTD and hence its baffling factor vary strongly with flow rate up to about 30 gpm. This can be attributed to the fact that each orifice of the tee experiences half the velocity of other inlet modifications for a given flow rate; once about 30 gpm is achieved, each of its orifices are sufficiently turbulent while other inlets achieve the same level of local turbulence at 15 gpm. Conversely, for a total *Q* of 10 gpm the smaller velocities at each orifice imply turbulence levels that are too low for effective scalar transport.

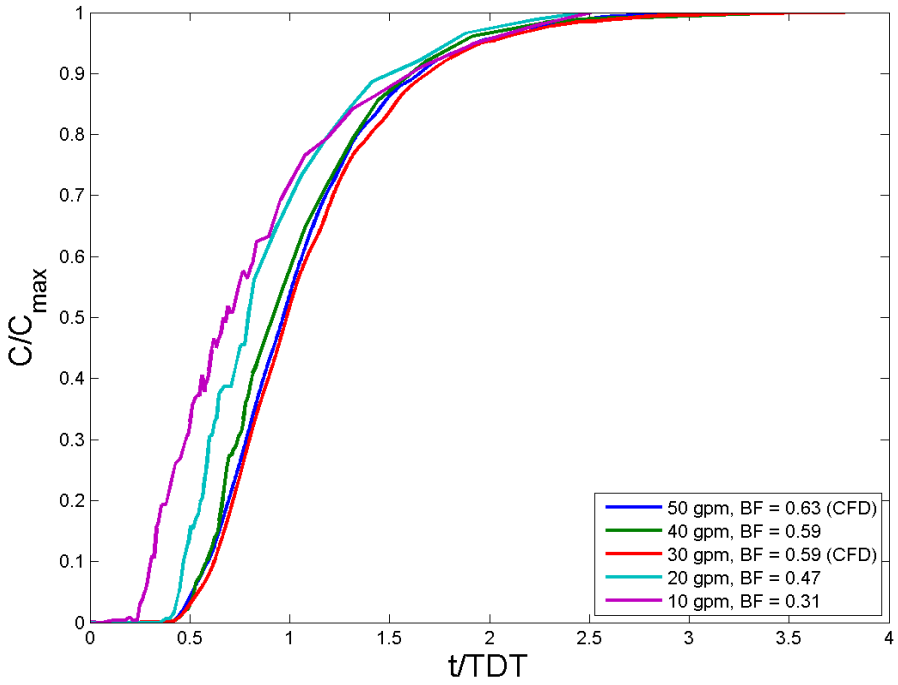

(a)

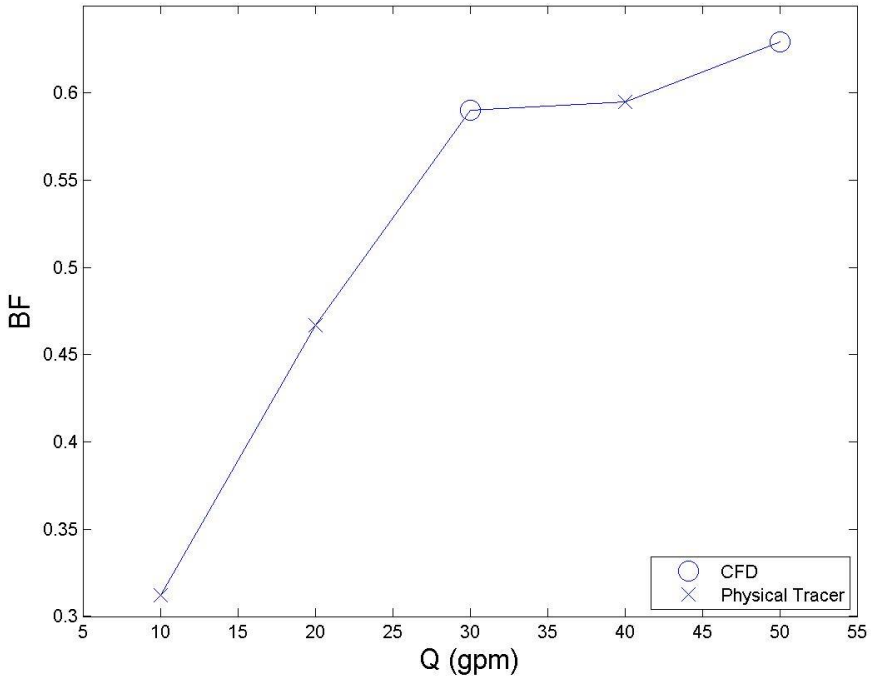

(b)

Figure 4.14: (a) RTDs and (b) Baffling Factors at Various *Q*s for the Teed Inlet

The lower Reynolds numbers found in the tank for low and high flow rates are implied in Figure 4.15. Small velocities associated with lower flow rates do not allow the influent to fill up the large dead zones above the sharp inlet nearly as well as would be achieved with higher velocities. Even in the volumes that the jet does manage to dissipate into, scalar mixing cannot be as efficient due to lower and perhaps intermittent turbulence.

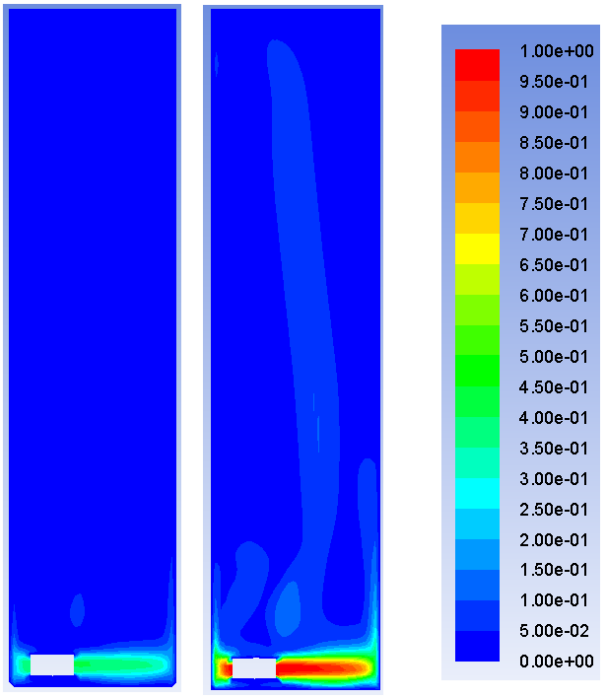

(a) (b)

Figure 4.15: Velocity Magnitudes ($V/V_{max,\ 50\ gpm}$) for (a) 10 gpm and (b) 50 gpm for Teed Inlet

Figure 4.16 serves to corroborate well with Figure 4.15. Evidently, higher initial momentum allows much more vertical spreading for a quicker development of channel-like flow. The tank flowing at 10 gpm is much "quieter" and throughout much of the longitudinal slice a larger contour is seen only at the bottom, similar to the unmodified scenario, implying that homogenization of stream-wise velocities throughout cross-sectional areas is not occurring in the first channel and that dead zones have largely not been avoided. A comparable baffling factor to the straight inlet is observed as a result. Flow rates of 30 and 40 gpm are fully turbulent at the

inlet and behave quite similarly to flow at 50 gpm and hence are not shown or discussed here. The tank flowing at 20 gpm intuitively acts somewhere between these two extremes.

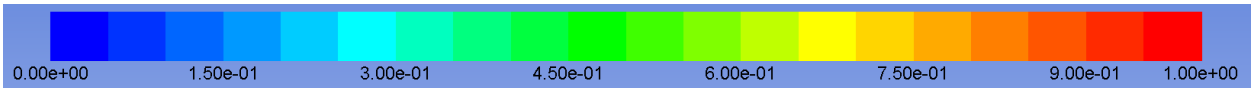

(a)

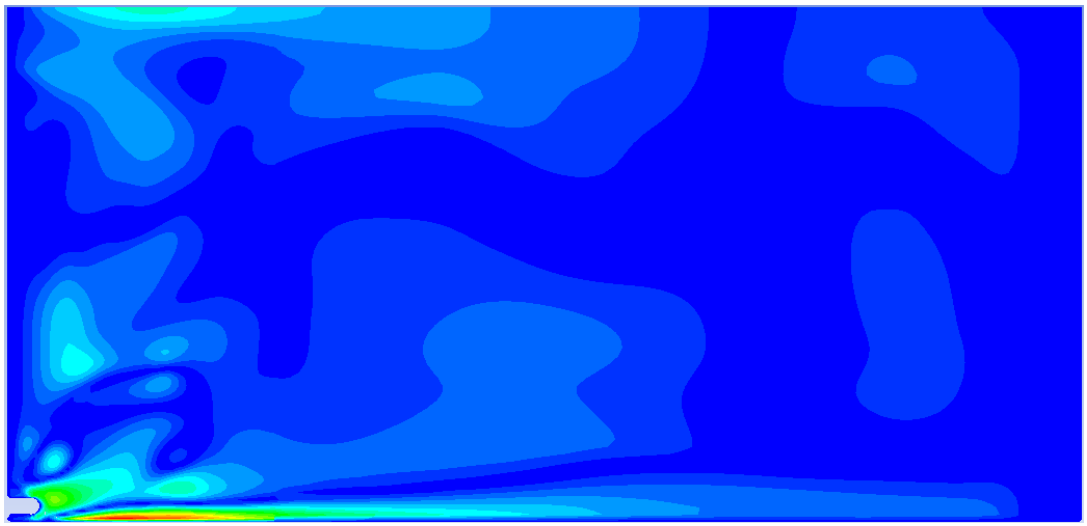

(b)

Figure 4.16: Longitudinal Velocities ($u/u_{max,\ 50\ gpm}$) for Teed Inlet at (a) 10 gpm and (b) 50 gpm

4.7.6 Evolution of Scalar Concentration at the Free Surface

In order to further legitimize this hydrodynamic analysis, time progression of the scalar concentration at the free surface is shown in Figure 4.17 for the cases of the straight and teed inlets. *t/TDT* values up to 1 were chosen because this is where the largest changes in RTD curves occur and hence provide the best illustration of the differences in scalar transport due to modified inlet conditions. The elbow-up inlet condition is omitted to avoid redundancy; it is simply somewhere between the straight and teed inlets, so the comparison of these two extreme cases is an adequate example of different scalar transport progression. Although the velocity and scalar fields are clearly three-dimensional throughout most of the contact tank, the free surface was chosen to depict scalar concentrations because the inlet is located at the bottom; it follows from this that superior mixing has likely occurred at any elevation below the free surface, so the highest elevation is the most conservative horizontal plane to examine.

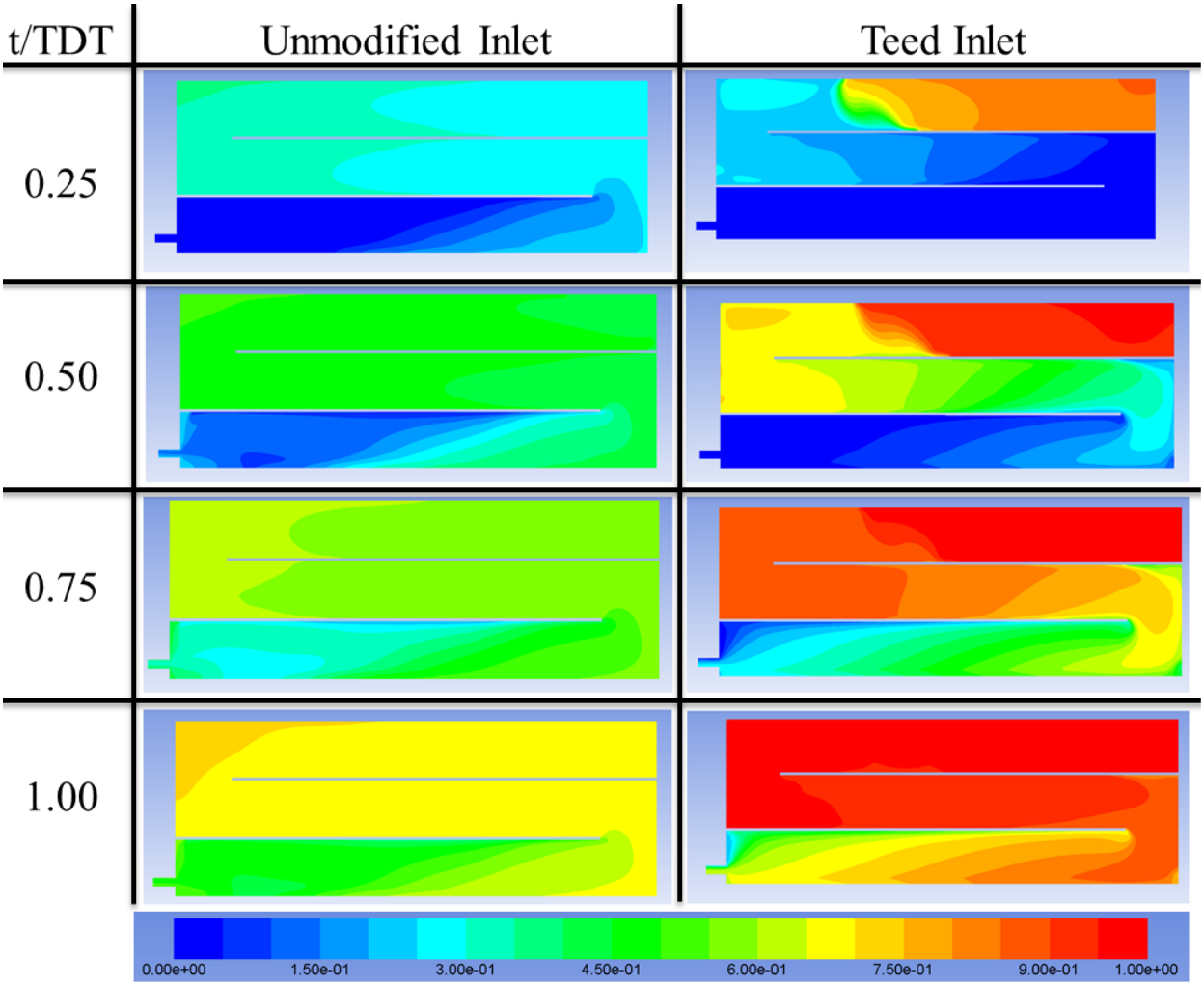

Figure 4.17: Time Dependence of Scalar Concentration at the Free Surface for the Unmodified and Teed Inlets

The reader is now referred back to Figure 2.1, which illustrates the ideal RTD curve. At *t=TDT* an instantaneous jump of normalized scalar concentration from 0 to 1 occurs corresponding to pure advection. Such a scenario would be manifested as a sudden jump in contours of concentration from 0 to 1, so any deviation from this is due to in the inefficiencies in the tank that leads to diffusive action. Quicker transitions from high to low concentrations therefore approximate plug flow better than slower transitions. With this in mind, the marked differences seen between scalar concentrations at the free surfaces for these two inlets corroborate well with the hydrodynamics presented in this section.

For all points in time two important observations are made in the tank with the teed inlet: first, normalized concentrations much closer to one are found throughout all channels compared to the straight inlet. By the time the flow reaches *t=TDT* the first 2 channels are mixed to scalar values of nearly 1 while the third channel decreases monotonically, whereas the tank with a straight inlet has a maximum concentration of about 0.7 (and only found in a small corner) for the same point in time. Secondly, the contours are much closer together as concentrations go back down to zero. This is in accordance with the notion that the teed inlet allows flow conditions to better emulate plug flow early in the first channel, leading to smaller deviations from the ideal inlet. In fact for the straight inlet, in the vicinity of the transition between channels 1 and 2, the concentration temporarily increases only to go back down again. This is a clear indication of a poor imitation of plug flow. Both of these notions seem to hold true at all *t/TDT*s.

4.8 Conclusions

To summarize, managers of drinking water systems for small municipalities often face issues with adequate water disinfection stemming from lack of expertise and funding. In baffled contact tanks, sharp inlets can be easily and cheaply modified to make better use of the higher levels of turbulence found in the vicinity of the inlet relative to the rest of the tank. This allows the water to better approximate ideal plug flow by filling up transverse and vertical directions of the tank quickly to maximize channeling effects, especially in the first channel.

Seven attachments were used to modify the sharp inlet of a 1,500 gallon contact tank: an elbow pointed left, right, up and down, a tee, a backward-pointing U-shaped piece, and a 3-way inlet. It was found that significant gains in mixing efficiency were achieved for all modifications except the 3-way inlet, whose side orifices encouraged larger short-circuiting by the main jet. More specifically the elbow pointed all 4 directions as well as the U-shaped piece resulted in

baffling factors around 0.44 for a flow rate of 40 gpm. The teed inlet performed the best at this same flow rate, attaining a BF of 0.59. Its performance unfortunately decays quickly with flow rate below 30 gpm due to lower levels of turbulence at each orifice compared to the one-orifice inlet alternatives at the same flow rate. Nonetheless, this is a gain of about 70% in *BF* over the unmodified, straight-shooting inlet. Beyond 30 gpm the teed inlet showed only modest gains in hydraulic efficiency, hinting at a plateau in performance.

At any rate, any modification to a sharp inlet that deflects the flow into transverse and vertical directions rather than the longitudinal direction will allow unfavorable inlet conditions to better emulate an ideal inlet, whose baffling factor is estimated to be around 0.8 for this contact tank (Kattnig, 2014). It was shown by a hydrodynamic analysis that this can mainly be attributed to a quick homogenization of longitudinal velocities to bring the average flow field to two dimensions rather than three, thereby facilitating advection while minimizing dead zones, short-circuiting, and diffusive scalar transport.

Although baffled contact tanks are clearly superior, un-baffled systems are found in small municipalities throughout the United States. For such systems it is even more important that simple and cost-effective solutions are found. To this end Chapter 5 describes research undertaken to optimize mixing efficiency in these prevalent yet mediocre tanks.

CHAPTER 5: IMPACT OF INLETS ON MIXING EFFICIENCY IN UN-BAFFLED HYDRAULIC CONTACT TANKS

5.1 Introduction

Chapters 3 and 4 have shown that baffles are undoubtedly an efficient means of improving flow dynamics in a hydraulic contact tank. By combining baffles with maximum length-to-width ratios and inlets identical to the cross-section of tank compartments, residence time distributions of the disinfectant are optimized. Despite this, poorly designed tanks are found in many treatment facilities that lack baffles altogether. In an un-baffled system the largest inlet possible would still be desirable to promote plug flow but is extremely uncommon in practice; such a system is likely to be under strict budgeting limitations. As a result these tanks suffer from the detrimental combination of a lack of baffles and poor inlet conditions (hereon referred to as un-baffled sharp inlet tanks, or USITs). According to Table 1.1 a typical baffling factor for an arbitrary USIT would be on the order of 0.1, which is considered very poor (USEPA, 2003).

As was the case in Chapter 4, owners and managers of flawed tanks are in the direst need for system upgrades yet have the least amount of resources. Inlet modifications are again investigated as a practicable means of improving hydraulic mixing efficiency in the face of such fiscal constraints. However, the overall approach and resulting analysis must be somewhat different due to the different flow physics occurring throughout the tank.

5.2 Methodology

A contact tank similar to the one in Chapter 4 was studied using nine highly resolved CFD simulations. In light of the good agreement between the physical and predicted RTDs obtained for the baffled tank, the USIT counterpart was only investigated numerically. Conservative measures were taken to achieve a reasonable degree of confidence in results as

explained in Section 5.2.3. Dependence of RTDs on flow rate was not considered; rather, a typical flow rate of 40 gpm was used for all simulations.

Results are again quantified by both the baffling factor and Morrill index parameters in order to assess system RTD curves in the context of the USEPA's framework for drinking water disinfection and to evaluate the level of dispersion. The resolved flow fields from CFD modeling are briefly discussed to explain the results, and the chapter concludes with a summary of the research presented.

5.2.1 Prototype and Geometry

Due to its simple yet representative geometry, the same contact tank considered in Chapter 4 was used to research inlet modifications but with two key differences. First, the baffles were removed in order to explore un-channeled flow typically found in USITs. Second, the inlet and outlet were moved horizontally to the center of their respective walls. This was done in order to maintain symmetry after removing the baffles; in this way the entire tank can be thought of as a single compartment with a lower length-to-width ratio than before. Furthermore, all tested inlet modifications are symmetric with respect to the primary direction of flow. Figure 5.1(a) shows an isometric view of the tank, while Figure 5.1(b) depicts a plan-view schematic. Flow was assumed to occur at a depth of 63.1 inches. Small variations in actual flow depth may arise depending on inlet condition, but both *BF* and *MI* were found to be relatively insensitive to this variable. Changes in flow depth were therefore ignored.

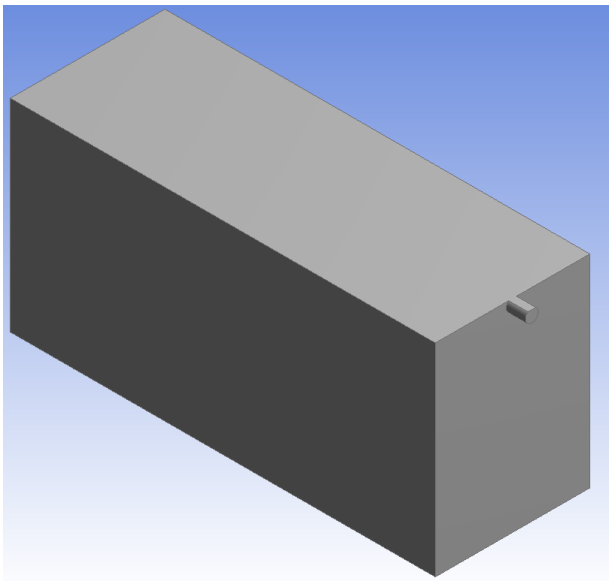

(a)

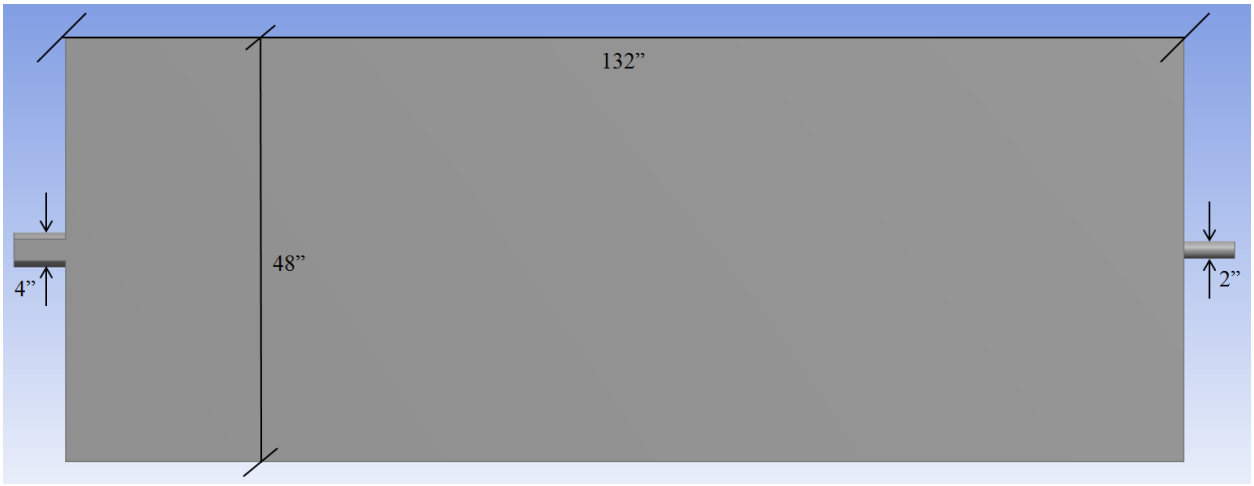

(b)

Figure 5.1: Modeled Geometry of the USIT: (a) Isometric View and (b) Plan View with Dimensions

An exception to the inlet/outlet configuration shown in Figure 5.1 is the “base case” wherein the locations of the inlet and outlet are left as they were in the baffled tank. This intuitively allows for a longer flow path by making use of the diagonal distance of the

rectangular footprint rather than the longitudinal length of 132 inches. Performance of this base case allows for a means of assessing system performance relative to unmodified inlet conditions.

5.2.2 Inlet Modifications

Because of the much larger cross section of the USIT, a deflection of flow using one orifice will not be nearly as effective as it was in Chapter 4. As such the base case and seven modifications with multiple orifices were investigated for potential increases in hydraulic contact times. An ideal (but unrealistic to implement in practice) inlet comprising the entire back wall of the tank, 48 inches wide by 63.1 inches high, was also modeled to obtain an upper bound of mixing efficiency achievable by this system. The seven modifications are as follows. Unless otherwise noted, each orifice is 2 inches in diameter and located negligibly far from the tank's wall, 2 inches from the floor.

- Four inlets, equally spaced, shooting straight
- Four inlets, equally spaced, shooting upward
- Four inlets, equally spaced, shooting backward
- Four inlets, two shooting to the left and two to the right
- Four inlets, spread equally over the plan view of the tank, shooting downward
- Four inlets spread equally over the plan view of the tank, shooting downward, with the outlet moved to the center of the free surface
- Eight inlets spread equally over the plan view of the tank, shooting down

5.2.3 CFD Modeling

The same CFD methodology employed in Chapter 4 was used for the USIT in this chapter: grid independence was assumed to occur at 1,300,000 cells since Kattnig (2014) showed that the baffling factor changed negligibly beyond 1,000,000 cells for the tank at hand. Kattnig also showed time step independence at $\Delta t = 2s$, so a Δt of 1s was chosen for conservativeness. A RANS framework was employed with the RNG k-ε or RSM closure scheme to model turbulence. The RNG k-ε model was used for the straight and upward shooting inlets, while the RSM was chosen for all other scenarios due to the expected difficulties encountered when jets impinge onto solid surfaces. The same solver settings described in Chapter 4 were associated with each of the closure schemes.

Boundary conditions were also identical to the baffled tank of Chapter 4. It should be noted that for the inlets, pipes leading to each orifice were hydraulically identical, i.e. same bends, lengths, material, etc., so that head loss is the same through each pipe and each orifice discharges the same flow rate. The prescribed cross-sectional-averaged velocity at each orifice then corresponds to Q/N, where Q = 40 gpm and N is the number of orifices for the inlet configuration in question.

After fully resolving the steady state flow field, a non-dimensional value for the passive conservative scalar representing the disinfectant of 1 was specified at each orifice. The Reynolds-averaged advection-diffusion equation was then solved at each time step and RTD curves were obtained by monitoring the outlet over time.

5.3 Results

5.3.1 RTD Curves and Baffling Factors

Figure 5.2(a) depicts RTD curves for the base case, all inlet modifications, and the ideal inlet simulated at 40 gpm. Baffling factors for each inlet condition are summarized in Figure 5.2(b) for increased clarity of the results. Although none of the tested attachments are efficient as the ideal inlet, several of them improved mixing efficiency. In agreement with Kattnig's analysis (2014) the base case was found to result in a baffling factor of just 0.06. The four-orifice inlets shooting straight and up both performed even worse, achieving BF values of just 0.03 and 0.05, respectively. The four sideways inlets attained a middling *BF* of 0.16; this is a disappointing result since it is analogous to the T-shaped piece, which was the superior option in the baffled tank of Chapter 4.

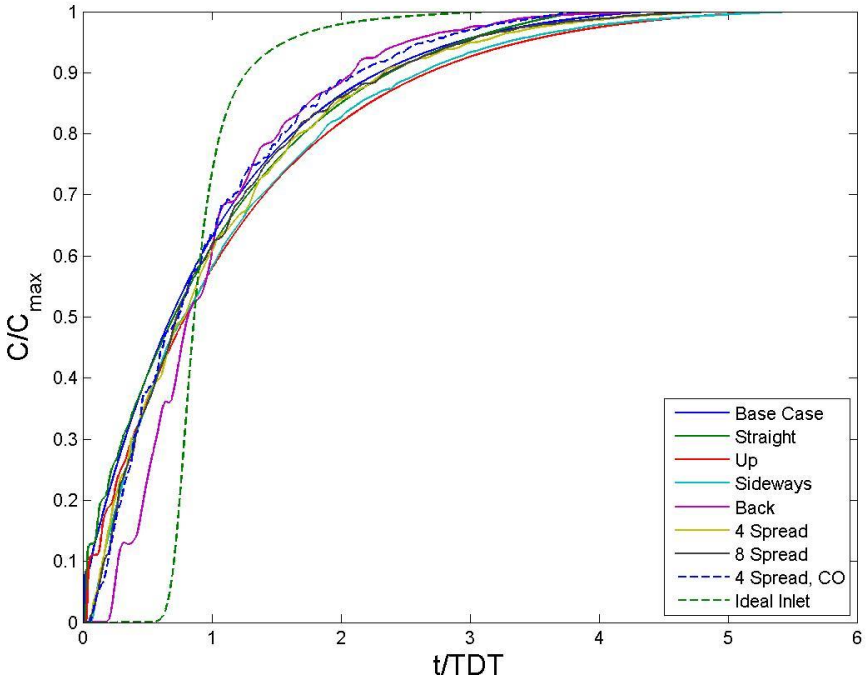

(a)

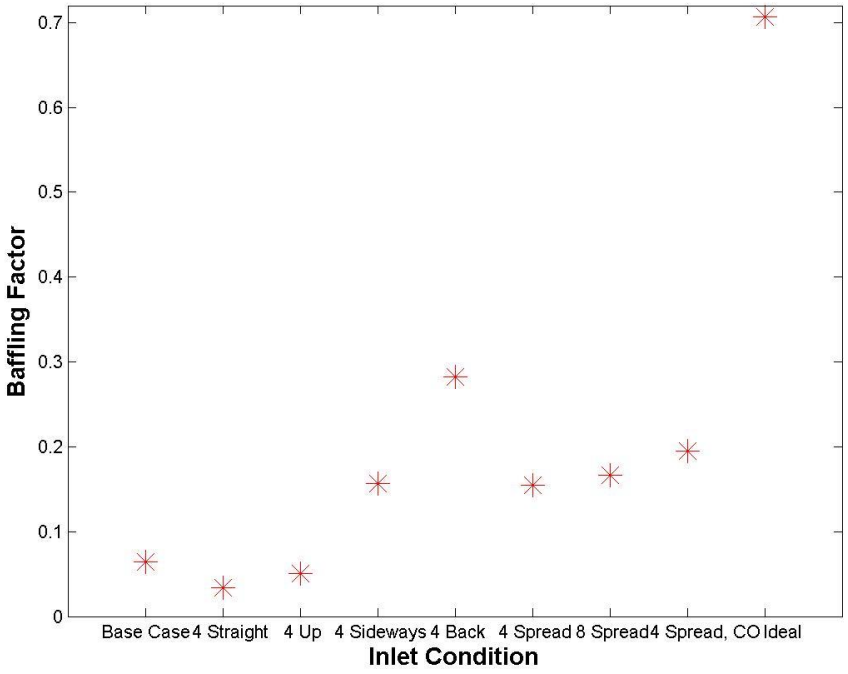

(b)

Figure 5.2: (a) Simulated RTD Curves and (b) Corresponding Baffling Factors

The spread-out configurations were investigated to assess whether or not it is prudent to divert some of the flow into portions that intuitively may be short-circuited otherwise. Unfortunately, a consequence of this design is that orifices closer to the outlet cause 10% of the concentration to reach the outlet sooner, resulting in low baffling factors because of *BF*'s dependence on t_{10}. One simulation was run with an outlet at the center of the free surface to see if plug-like flow could be achieved in the vertical direction. A small gain in *BF* was noted over the original outlet position but the results indicate that this is not an optimal design due to an even lower length-to-width ratio than the main flow direction of the original inlet/outlet setup.

Finally, the four inlets shot towards the back wall of the tank resulted in the best baffling factor of the modifications tested. Although it does not quite reach the worst case scenario of the baffled tank (*BF* = 0.34) and is well shy of the ideal inlet's *BF* of 0.71, a *BF* of 0.28 is an impressive gain of over 300% relative to the unmodified USIT.

5.3.2 Morrill Indices

Morrill indices are summarized in Table 5.1 to ensure that the predicted *BF* values are not misleading (recall that the baffling factor does not measure overall dispersion or recirculation in the tank). Since the inlet conditions are organized from lowest to highest *BF*s, the corresponding *MI*s should successively decrease from one configuration to the next. This is what is indeed observed, meaning system performance is adequately quantified by *BF* values for the study presented here. As expected extremely high levels of dispersion accompany poor baffling factors, making such inlet designs poor choices for contact tanks as evidenced by behavior over the entire RTD curve.

Table 5.1: *BF* and *MI* Values for Each Inlet Condition

Inlet Condition	BF	MI
4 Straight	0.03	70.01
4 Up	0.05	52.83
Base Case	0.06	35.56
4 Spread	0.15	15.03
4 Sideways	0.16	16.72
8 Spread	0.17	14.18
4 Spread, CO	0.19	10.94
4 Back	0.27	7.65
Ideal	0.71	1.80

5.4 Hydrodynamic Analysis

The hydrodynamic analysis presented in Chapter 4 adequately demonstrates the need to emulate the ideal inlet as quickly as possible by homogenizing longitudinal velocities and dissipating vertical velocities in order to enhance residence time distributions. As alluded to in Section 5.2.1, optimal performance of un-baffled contact tank can perhaps be thought of as a single channel with a much lower length-to-width ratio of flow than its baffled counterpart. In this context the base case and best modification that was simulated (i.e. 4 inlets shooting backwards) are briefly compared to explain the results. The ideal inlet is included as reference to the best possible scenario for this particular USIT.

Figure 5.3 shows the behavior of longitudinal velocities throughout each of the three scenarios being analyzed. The cross-sections shown are at 10, 33.3, 66.7, and 90 percent of the total length of the tank, and a view of the full tank is shown for reference. As with a baffled tank, it appears that a more uniform flow results in superior mixing conditions as evidenced by Figure 5.3 and consideration of each tank's respective RTDs. The contours in the base case clearly imply a jet shooting along the lower-left portion, bypassing huge volumes of the tank and

resulting in poor contact times. Four inlets directed backwards help alleviate this issue but several contours in the cross sections still imply a lack of uniform flow. Finally the ideal inlet shows negligible transverse gradients in longitudinal velocities until the end, at which point the relatively small outlet causes flow to accelerate so that it can exit at the free surface.

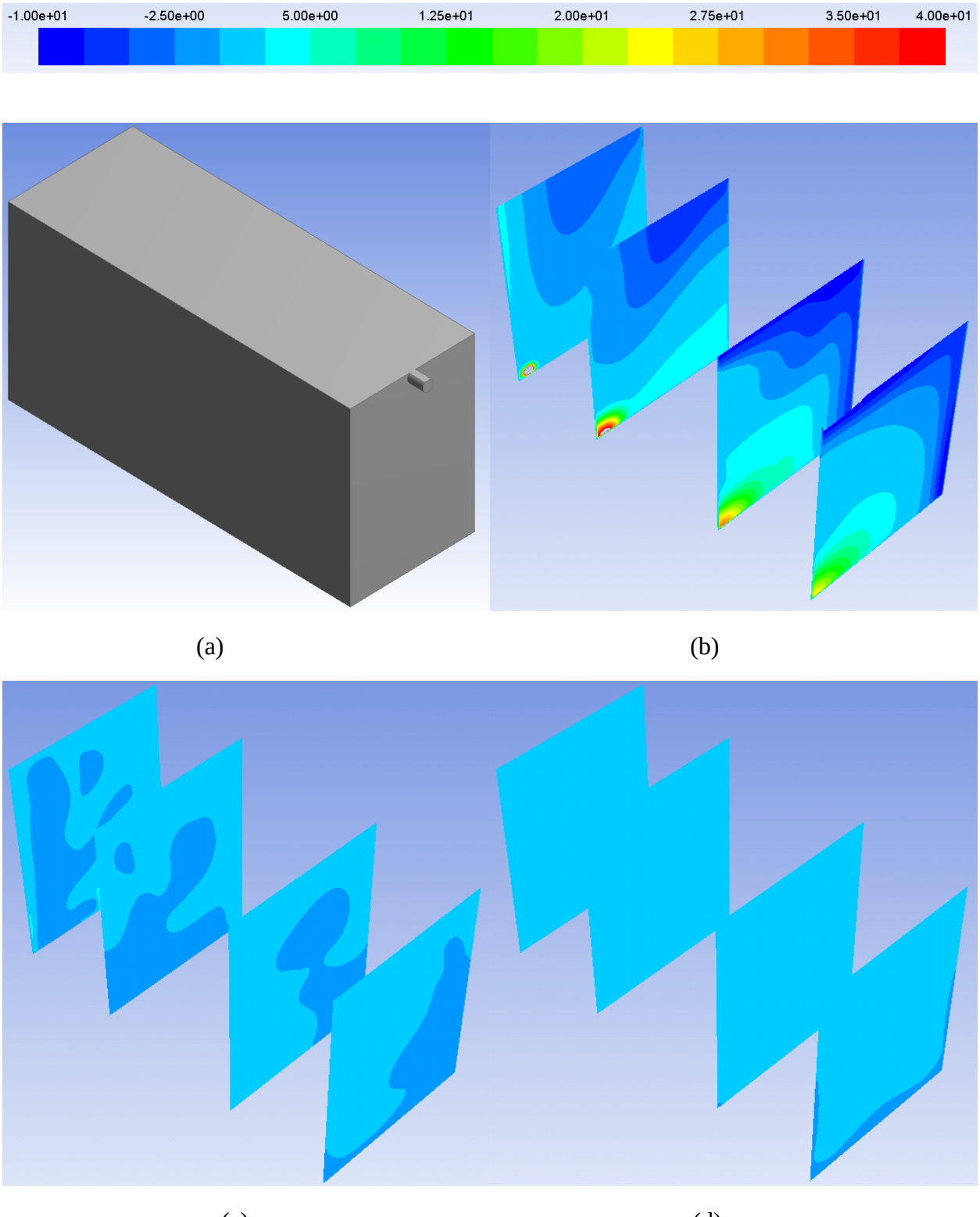

Figure 5.3: (a) Isometric View of Tank for Reference (b) Contours of Longitudinal Velocities (cm/s) for the Base Case (c) for 4 Inlets Shot Backward (d) for the Ideal Inlet

Again drawing parallels to the baffled tank of Chapter 4, the distribution of vertical velocities within the tank are assessed. In Figure 5.4, x is defined as the stream-wise direction from the inlet to the outlet and L_{total} is the total length of the tank in the x-direction (132 inches). Area-weighted averages of vertical velocities in 20 cross-sections, each spaced apart by $0.05 \cdot L_{total}$ (except the last one at $0.99 \cdot L_{total}$) were taken for each of the three inlet conditions analyzed.

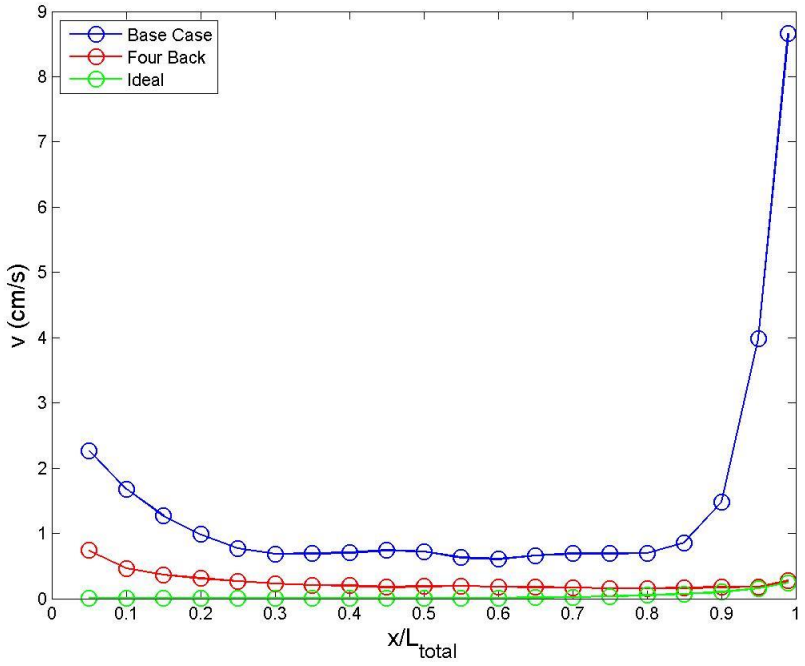

Figure 5.4: Area-Weighted Averages of Vertical Velocities throughout the USIT

As expected, the ideal inlet contained negligible vertical flow throughout the tank, until the end where water in lower portions of the tank rises up to exit at the free surface. In contrast to this the base case experiences a large upshot in vertical velocities at the end due to its severe short-circuiting. The four inlets oriented backwards starts with higher vertical velocities as flow spreads throughout cross-sectional dimensions but appears to stabilize to nearly zero by about 20% of the system's length.

5.5 Conclusions

USITs inevitably lead to inferior mixing conditions relative to a baffled contact tank. However, simple modifications can be made to the inlet in order to mitigate poor geometric design. Seven alterations the inlet were numerically investigated by CFD models, five of which enhanced contact times relative to the unmodified inlet. Of these, the configuration wherein four orifices shoot inflow towards the back wall performed the best, attaining a *BF* and *MI* of 0.27 and 7.65, respectively. This is thought to be due to spreading flow to the transverse and vertical directions of the tank, the former of which are significantly larger than in the baffled tank, thereby substantially reducing short-circuiting and mimicking plug flow behavior as closely as possible. A brief hydrodynamic analysis confirmed that despite low length-to-width ratios, promoting channel-like flow as quickly as possible results in optimal residence time distributions.

CHAPTER 6: SUMMARY AND CONCLUSIONS

6.1 Summary of Research

This thesis summarizes research that assesses the effect of geometric design on the performance of hydraulic contact tanks used for drinking water disinfection. Both physical and numerical experimentations were undertaken as part of this study. After outlining the necessary literature review in Chapter 2, Chapter 3 highlighted a 2D parametric study of a baffled contact tank with an ideal inlet. More specifically the effects of the width of flow relative to the turning radius around each baffle were scrutinized in order to determine the optimal ratio of L_{bo}/W_{ch} for various geometric configurations. These results were determined by 30 highly resolved two-dimensional CFD simulations, which in turn were validated by empirical measurements taken by Shiono et al (1991).

Noting that in practice many contact tanks do not have ideal inlets, the effects of sharp inlets were researched in Chapter 4. With the financial constraints faced by many small municipalities in mind, cost-effective and easily-installed attachments to sharp inlets were tested on a laboratory-scale physical prototype using step-input tracer studies with sodium chloride. Resulting RTD curves due to three of these attachments were explained by means of a hydrodynamic analysis using CFD simulations that were validated from physical tracer studies.

Finally, un-baffled contact tanks with poor inlet conditions were considered in Chapter 5. Such systems typically give way to extremely poor flow dynamics, leading to large amounts of short-circuiting and inadequate microbial inactivation. Since these tanks are commonly owned by municipalities with small budgets, an approach similar to the baffled tank of Chapter 4 was taken wherein inexpensive alterations to the inlet were considered. The results obtained were

purely from CFD experimentation; this is justified by using the same modeling approach that led to good agreement between physical and numerical data in the baffled contact tank from Chapter 4.

6.2 Major Conclusions

In Chapter 3, the footprint from the tank studied by Shiono et al (1991) was altered to investigate three channel widths and five baffle widths per baffle orientation for a total of 30 geometric configurations. It was found that L_{bo}/W_{ch} is a primary parameter to consider when geometric design of contact tanks; in particular L_{bo}/W_{ch} should be on the order of 1 in order to prevent extraneous contractions or expansions. These can lead to unnecessary flow separation as the flow traverses around baffle tips and cause poor contact times and/or recirculation. Performance was quantified by both the baffling factor and Morrill index. Maintaining L_{bo}/W_{ch} near 1 appears to produce more desirable flow dynamics regardless of baffle orientation and channel width. It was also confirmed that higher length-to-width ratios in the flow (i.e. large L_T/W_{ch} values) lead to superior RTD curves due to more plug-like flow conditions.

A two-baffle contact tank with poor inlet conditions was analyzed in Chapter 4 through both physical and CFD testing. A mediocre *BF* of just 0.34 was obtained without any modifications, so seven inlet attachments were investigated in an attempt to produce better contact times: A 90° elbow oriented 4 directions (left, right, up, and down), a U-shaped piece diverting flow at the inlet 180°, a three-way piece shooting flow left, right, and straight simultaneously, and a tee-shaped piece diverting flow to the left and right simultaneously. Despite a sensitivity to flow rate the tee-shaped piece was found to enhance contact times the most, attaining a 74% gain in *BF* of 0.59 at 40 gpm over the baseline tank. A hydrodynamic analysis concluded that any inlet modification that leads to quicker dissipation of vertical

velocities (implying two-dimensional, plug flow behavior) will boost the residence times in hydraulic contact tanks.

A similar approach was taken in Chapter 5 to enhance RTD curves in tanks without baffles and with poor inlet conditions. Seven hypothetical attachments were computationally modeled. These attachments are different from Chapter 4 due to new tank geometry and hence new flow physics. Compared to the results from Chapter 4 the modifications were disappointing but not surprising; the best alteration, wherein 4 equally-spaced inlets deflect flow to the bottom of the back wall of the tank, achieved a *BF* of 0.27. Relative to the unmodified tank's *BF* of just 0.06, however, this is a gain of over 300%. Therefore managers of un-baffled disinfection tanks with sharp inlets may wish to implement such a modification in order to produce safer drinking water through more cost-effective means.

6.3 Future Research Considerations

Two major impacts of hydraulic contact performance are noted that are not taken into account by geometric considerations:

- Stratified flow can occur in tanks for several reasons, e.g. a significant gradient of sodium chloride concentration in the flow or large temperature differences between the source water and ambient air in the treatment facilities. In the case of unstable stratification, lighter strata originally at greater depths tend to rise to the surface while heavier strata at lower depths sink to the bottom, thereby enhancing mixing. This would result in a conservative underestimation of contact tank performance. In the case of stable stratification, however, contact times could appear to be greater than they are while the disinfectant actually short-circuits vast portions of the tank. It would therefore be

desirable to determine a reliable and tractable means of quantifying contact tank performance in such a scenario.

- Residence time distributions are usually approached assuming that the flow field has reached a steady state condition from which unsteady scalar transport is assessed. If the net flow rate through the system is not constant, such a framework may not be valid (a tank's *TDT*, for example, is not so easily defined). Determining system performance when inflow is greater than outflow (or vice versa) remains a topic that should receive considerably more attention.

REFERENCES

Amini, R.; Taghipour, R.; Mirgolbabaei, H. 2011. Numerical Assessment of Hydrodynamic Characteristics in Chlorine Contact Tank. *International Journal for Numerical Methods in Fluids*. **67 (7)**, 885-898. DOI 10.1002/fld.2394

Angeloudis, A.; Stoesser, T.; Falconer, R.A. 2014. Predicting the disinfection efficiency range in chlorine contact tanks through a CFD-based approach. *Water Research*. **60**, 118-129.

ANSYS Inc. 2011. ANSYS FLUENT Theory Guide. Canonsburg, PA.

Barnett, T.C. 2013. *Flow Dynamics and Scalar Transport in Drinking Water Contact Tanks*. Master's Thesis, Department of Civil and Environmental Engineering, Colorado State University, Fort Collins, CO.

Bradbrook, K.F.; Biron, P.M.; Lane, S.N.; Richards, K.S.; Roy, A.G. 1998. Investigation of Controls on Secondary Circulation in a Simple Confluence Geometry Using a Three-Dimensional Numerical Model. *Hydrological Processes.* **12**, 1371.

Brouckaert, C. J.; Buckley, C. A. 1999. The Use of Computational Fluid Dynamics for Improving the Design and Operation of Water and Wastewater Treatment Plants. *Water Science and Technology*. **40 (4-5)**, 81-89. DOI 10.1016/S0273-1223(99)00488-6

Cockx, A.; Do-Quang, Z,; Liné, A.; Roustan, M. 1999. Use of Computational Fluid Dynamics for Simulating Hydrodynamics and Mass Transfer in Industrial Ozonation Towers. *Chemical Engineering Science.* **54**, 5085-5090

Crozes, G.F.; Hagstrom, J.P.; Clark, M.M.; Ducoste, J; Burns, C. 1999. Improving clearwell design for CT compliance, *AWWARF & AWWA*, Denver. ISBN O-89867-963-X

Davis, M.L; Cornwell, D.A. 2008. *Introduction to Environmental Engineering*; McGraw Hill: New York.

Evans, H; Bauer, Mike; Goodman, N; Hague, J; Ta, T. 2003. The Role of Ozone in Improving Drinking Water Quality in London and Oxford. *Ozone: Science & Engineering: The Journal of the International Ozone Association.* **25(5)**, 409-416. DOI: 10.1080/01919510390481739

Greene, D. J.; Haas, C. N.; Farouk, B. 2006. Computational Fluid Dynamics Analysis of the Effects of Reactor Configuration on Disinfection Efficiency. *Water Environment Research.* **78(9)**, 909-919. DOI 10.2175/106143005X72984

Gualtieri, C. 2006. *Numerical simulations of flow and tracer transport in a disinfection contact tank*. In Proc. of iEMSs 2006 Conf.

Gualtieri, C. 2010. Discussion on E. C. Teixeira and R. N. Siqueira: Performance assessment of hydraulic efficiency indexes. J. Env. Eng., ASCE, vol.134, n.10, October 2008, pp.851−859. *Journal of Environmental Engineering*, ASCE, 136(9), 1006−1007.

Hannoun, I.A.; Boulos, P.F.; List, E.J. 1998. Using hydraulic modeling to optimize contact time.

J. Am. Water Works Assoc., August: 77-78.

Huismans, L., and W. E. Wood. 1974. Slow Sand Filtration. *World Health Organization*. Web. 3 June 2014.

Johnson, S. 2006. *Ghost Map: The Story of London's Deadliest Epidemic-- and How It Changed the Way We Think about Disease, Cities, Science, and the Modern World*. New York, NY: Penguin Group. 195-96.

Kattnig, J. 2014. *Use of Innovative Techniques to Optimize the Residence Time Distribution of Drinking Water Contact Tanks*. Master's Thesis, Department of Civil & Environmental Engineering, Colorado State University, Fort Collins, Colorado.

Khan, L. A.; Wicklen, E. A.; Teixeira, E. C. 2006. Validation of a Three-Dimensional Computational Fluid Dynamics Model of a Contact Tank. *Journal of Hydraulic Engineering*. **132 (7)**, 741-746. DOI 10.1061/(ASCE)0733-9429(2006)132:7(741)

Kim, D.; Kim, D.I.; Kim, J.H.; Stoesser, T. 2010. Large Eddy Simulation of Flow and Tracer Transport in Multichamber Ozone Contactors. *Journal of Environmental Engineering.* **136(1)**, 22-31. DOI: 10.1061/ASCEEE.1943-7870.0000118

Kim, D.; Kim, J.; Stoesser, T. 2013. The effect of baffle spacing on hydrodynamics and solute transport in serpentine contact tanks, *J. Hydraulic Research.* **51 (5),** 558-568.

Letterman, R.D; ed. 1999. *Water Quality and Treatment, 5th ed.* American Water Works Association, McGraw-Hill: New-York.

Li, X. X.; Liu, C.H.; Leung, D. Y. C. 2006. Recent Progress in CFD Modelling of Wind Field and Pollutant Transport in Street Canyons. *Atmospheric Environment.* **40**, 5640-5658.

Moin, P. 2010. *Fundamentals of Engineering Numerical Analysis*. Cambridge University Press: New York, NY.

Morrill, Arthur B.; Dean, John B.; Orton, James W.; Ellms, J.W. 1932. Sedimentation Basin Research and Design [with discussion]. *American Water Works Association.* **24**, 1442-1463.

Munson, Bruce R.; Rothmayer, Alric P.; Okiishi, Theodore H.; Huebsch, Wade W. 2013. *Fundamentals of Fluid Mechanics.* Wiley Publishing: Hoboken, NJ

Peplinski, D. K.; Ducoste, J. J. 2001. Lessons for Applying Computational Fluid Dynamics Modeling to Disinfection Clearwells. *Bridging the Gap: Meeting the World's Water and Environmental Resources Challenges.* DOI 10.1061/40569(2001)22

Pope, S.B. 2000. *Turbulent Flows*. Cambridge University Press: Cambridge, U.K.

Rauen, W. B.; Angeloudis, A.; Falconer, R. A. 2012. Appraisal of Chlorine Contact Tank Modelling Practices. *Water Research*. **46 (18)**, 5834-5847. DOI 10.1016/j.watres.2012.08.013.

Shiono, K.E.; Teixiera, E.C.; Falconer, R.A. 1991. Turbulent Measurements in a Chlorine

Contact Tank. *The 1st International Conference on Water Pollution: Modeling, Measuring and Predicting*. Southampton, UK. 519–531.

Shiono, K.; Teixeira, E.C. 2000. Turbulent characteristics in a baffled contact tank. *J. Hydraulic Research* (JHR), **38(6)**, 403-416.

Singer, P. C. 1994. Control of disinfection by-products in drinking water, *J. Environ. Eng.*, **120(4),** 727-744.

Stamou, A. I. 2002. Verification and Application of a Mathematical Model for the Assessment of the Effect of Guiding Walls on the Hydraulic Efficiency of Chlorination Tanks. *Journal of Hydroinformatics.* **4(4)**, 245-254.

Stamou, A. I. 2008. Improving the Hydraulic Efficiency of Water Process Tanks using CFD Models. *Chemical Engineering and Processing: Process Intensification.* **47**, 1179-1189.

Taylor, Z. H.; Xu, Q.; Wilson, J. M.; Venayagamoorthy, S. K. 2012. Computational Modeling of Baffled Disinfection Tanks. *World Environmental and Water Resources Congress*. DOI 10.1061/9780784412312.129

Teixeira, E. C.; Siqueira, R. N. 2008. Performance Assessment of Hydraulic Efficiency Indexes. *Journal of Environmental Engineering*, **134(10)**, 851-859.

Templeton, M. R.; Hofmann, R.; Andrews, R. C. 2006. Case Study Comparisons of Computational Fluid Dynamics (CFD) Modeling Versus Tracer Testing for Determining Clearwell Residence Times in Drinking Water Treatment. *Journal of Environmental Engineering Science*. **5(6)**, 529-536. DOI 10.1139/S06-007

Ueberhuber, C. W. 1997. *Numerical Computation 1: Methods, Software, and Analysis.* Springer Publishing Company: New York, NY

United States Environmental Protect Agency, USEPA. 2003. *Disinfection Profiling and Benchmarking Guidance Manual.* **EPA 815-R-99-013**, Office of Water, Washington, D.C.

United States Environmental Protect Agency, USEPA. 1991. *Guidance Manual for Compliance with the Filtration and Disinfection Requirements for Public Water Systems Using Surface Water Sources.* **EPA-68-01-6989,** Office of Drinking Water, Washington, D.C.

United States Environmental Protection Agency, USEPA. 2011. *National Characteristics of Drinking Water Systems Serving Populations Under 10,000*. **EPA 816-R-10-022,** Office of Water, Washington, D.C.

United States Geological Survey (USGS). 2014. *How much water is there on, in, and above Earth?* < http://water.usgs.gov/edu/earthhowmuch.html>

Venayagamoorthy, S.K.; Stretch, D.D. 2010. On the Turbulent Prandtl Number in Homogeneous Stably Stratified Turbulence, *Journal of Fluid Mechanics*. **644**, 359-369. DOI 10.1017/ S002211200999293X

Versteeg, H. K; Malalasekera, W. 2007. *An Introduction to Computational Fluid Dynamics: The Finite Volume Method, Second Edition*. Pearson Education: Harlow, England

Wang, H.; Falconer, R.A. 1998. Simulating Disinfection Processes in Chlorine Contact Tanks Using Various Turbulence Models and High-Order Accurate Difference Schemes. *Wat. Res.*, **32(5),** 1529-1543.

Wang, H.; Shoa, X.; Falconer, R. A. 2003. Flow and Transport Simulation Models for Prediction of Chlorine Contact Tank Flow-Through Curves. *Water Environment Research*. **75(5)**, 455-471. DOI 10.2175/106143003X141268

White, G. C. 1998. *Handbook of Chlorination and Alternative Disinfectants* (4th edn). Wiley: New York.

Wilcox, D.C. 2012. *Basic Fluid Mechanics, Fifth Edition.* DCW Industries, Inc: San Diego, California.

Wilson, J. M.; Venayagamoorthy, S. K. 2010. Evaluation of Hydraulic Efficiency of Disinfection Systems Based on Residence Time Distribution Curves. *Environmental Science & Technology*. DOI 10.1021/es102861g.

Wols, B.A.; Uijttewaal, W.S.J.; Rietveld, L.C.; Stelling, G.S.; van Dijk, J.C.; Hofman, J.A.M.H. 2008. Residence Time Distributions in Ozone Contactors. *Ozone: Science & Engineering: The Journal of the International Ozone Association.* **30(1)**, 49-57. DOI: 10.1080/01919510701759538

Wols, B.A.; Hofman, J.A.M.H.; Uijttewahl, W.S.J.; Rietveld, L.C.; van Dijk, J.C. 2010. Evaluation of Different Disinfection Calculation Methods Using CFD. *Environmental Modelling & Software.* **25(4)**, 573-582. DOI:10.1016/j.envsoft.2009.09.007

Wright, N.G.; Hargreaves, D.M. 2001. The Use of CFD in the Evaluation of UV Treatment Systems. *Journal of Hydroinformatics.* **3(2)**, 59-70.

Xu, Q.; Venayagamoorthy, S. K. 2010. Hydraulic efficiency of baffled disinfection contact tanks. 6th *International Symposium on Environmental Hydraulics*. Athens, Greece.

Yakhot, V.; Orszag, S.A. 1986. Renormalization Group Analysis of Turbulence. *J. Scientific Computing*, **1(1)**, 3-51.

Zhang, L.; Xia, Y; Jiang, B; Xiao, X.; Yang, X. 2013. Pilot Experimental Study on Shell and Tube Heat Exchangers with Small-Angles Helical Baffles. *Chemical Engineering and Processing: Process Intensification.* **69**, 112-118. DOI:10.1016/j.cep.2013.03.005

APPENDIX A: UDF

```
#include "udf.h"

DEFINE_DIFFUSIVITY(diff_coeff,c,t,i)

{

return C_MU_T(c,t) / 0.7+0.001;

}
```